MAGNETIC MULTILAYERED NANOWIRES BY ELECTRODEPOSITION FOR SPINTRONIC APPLICATIONS

A DISSERTATION
SUBMITTED TO THE FACULTY OF
UNIVERSITY OF MINNESOTA
BY

Mazin Mohammad Al-Maqablah

IN PARTIAL FULFILLMENT OF THE REQUIREMENTS
FOR THE DEGREE OF
DOCTOR OF PHILOSOPHY

Advisor: Bethanie J. H. Stadler

AUGUST 2013

ACKNOWLEDGEMENTS

First of all, I would like to express my sincere gratitude to my advisor, Prof. Beth Stadler for choosing to supervise me, for introducing me to this field, for the knowledge that she passed to me, and no doubt for her kindness and humanity. Without her continuous support, I would not have gone this far.

I would also like to thank Prof. Randall Victora for his excellent teaching and for introducing me to magnetism and magnetic recording technologies. I also owe him thanks for the continuous feedback he provided in all MINT related activities. That feedback was always helpful.

I owe special thanks for Prof. Paul Crowell for letting me use his labs for magnetotransport measurements and for the feedback and useful discussion he provided in group meetings and in my preliminary oral exam. I would also like to thank Prof. Stephen Campbell for the important suggestions he made on my preliminary oral exam. Those suggestions were very important and they helped me present my research material in a better way.

I am very grateful to my parents and my brothers for their love, support, and encouragement all over the past years. I would also like thank my father and mother in law for their support and for hosting my wife and daughter during their occasional stay in Jordan. At last but definitely not the least, I would like to thank and express my sincere appreciation for my life companion, my wife, Inas, for her patience, support, encouragement, and endless love.

DEDICATION

to my parents and brothers, to my beloved, my wife Inas, and to the pupil of my eye, my daughter Celine

ABSTRACT

Close-packed GMR arrays have recently drawn great attention because of their potential use in applications such as magnetic sensors and magnetic random access memory (MRAM). In this dissertation, Co/Cu multilayered nanowires were designed and engineered to meet these applications.

All-metallic current perpendicular to the plane (CPP) giant magnetoresistive (GMR) layers were made within insulating matrices by direct growth to avoid sidewall damage that is caused by lithographical patterning in current vacuum-deposited devices. These insulating matrices were made of Anodic Aluminum Oxide (AAO) templates and were grown both as free-standing membranes and as integrated layers on Si, both with columnar nanopores with diameters of 10-500nm. The barrier layer, which is a thin oxide layer at the bottom of the nanopores, was completely removed in both cases and Co/Cu multilayered nanowires were successfully grown inside these nanopores by DC electrodeposition. The thicknesses, diameters, and growth conditions were then engineered to make competitive structures for magnetic recording read sensors and spin torque RAM.

For read sensors, we synthesized 10nm-diameter nanowires composed of Co(15nm)/Cu(5nm)/Co(10nm) trilayers that had 30 Ω resistance and 19% magnetoresistance for disk drive read heads. In contrast to conventional read heads based on lithographically-produced magnetic tunnel junctions, these offer potentially easier fabrication and more than 100x lower resistance with commensurate reductions in heat

production. These wires were measured to have resistivities of 5.4×10^{-8} Ω.m, only three times higher than bulk values for copper. The low resistance, yet high magnetoresistance, is due to smooth sidewalls from *in situ* templated chemical growth. Thus, unlike lithographically-etched sensors, these nanowire sensors will be capable of reading high density (2-10 Terabit/in^2) bit patterned media, such as that produced by self-assembled block co-polymers.

For STT-RAM applications, spin transfer torque switching of Co/Cu multilayered nanowires with perpendicular c-axis was observed without the need for external magnetic fields with switching current densities below 10^7 A/cm^2. The switching current density varied with Cu interlayer thickness. When the Cu interlayers were thin, the samples exhibited one stable state (high resistance) at zero current which was explained by investigating interwire and intrawire dipole fields that were then confirmed by simple energy calculations. Structures with increasing the Cu spacer thicknesses required increased current densities to switch due to spin relaxation and also due to the switching of the effective magnetic anisotropy of the structures from parallel to perpendicular to the wire axes. This change in anistropy was also observed experimentally via magnetization hysteresis loops and confirmed by calculations of the effective demagnetizing fields for the layered structures. The ability to tune the demagnetizing field of these structures makes them very interesting candidates for future spin transfer torque RAM with multiple states per bit.

TABLE OF CONTENTS

LIST OF FIGURES

Chapter 1

Chapter 2

Chapter 3

Chapter 4

Chapter 5

Chapter 6

Chapter 1

Introduction

1.1. BACKGROUND AND MOTIVATION

In conventional electronics, the charge of the electron is used to manipulate, store, and transfer information. Devices based on this scheme often suffer volatility, i.e, data is erased soon after the power source is turned off. Also, according to Moore's law the number of transistors on a silicon chip will roughly double every two years [1]. With device scaling nearing its limit and with power consumption continuing to increase, it will be less than unlikely that memory devices based on conventional electronics will be used for future high density devices.

In spintronics, information is stored by the orientation of the spins instead of the charge. The orientation of the spin relative to a magnetic field is commonly referred to as spin "up" or spin "down". These two states can then represent a binary "1" or a binary "0" in memory devices. Compared to conventional electronics, spintronics devices offer lower power consumption, better scalability due to smaller required space on a chip, and faster speeds because spin manipulation is faster than charge manipulation. On top of all,

spintronic devices do not require a special semiconducting platform to fabricate the devices. Almost any substrate can be used to fabricate spintronics devices.

In reality, spintronic memory devices do not use one spin orientation to represent the “1” or “0”. They rather use the relative orientation of two spin directions as in the case of Ferromagnet/Nonmagnet/Ferromagnet (FM/NM/FM) sandwich structures. In these structures, the relative orientation of the two spin directions in the two ferromagnetic layers is usually used to determine the “1” or “0” state. For example, aligned spin directions can be used as a binary “1” whereas anti-aligned spin directions can be used for a binary “0”.

Historically, sandwich FM/NM/FM structures are classified depending on the type of nonmagnetic material used in the stack. For insulating nonmagnetic layers, the structures are called Magnetic Tunnel Junctions (MTJs) [2]. For a metallic nonmagnet, the structures are usually referred to as Giant Magneto-Resistive (GMR) structures [3]. Magnetic tunnel junctions are known to have high resistances (due to the insulating nonmagnetic layer) and high magnetoresistance (MR) ratio [4], defined as $(R_{high}-R_{low})/R_{low}$. GMR structures, on the other hand, have much lower resistances, but they come with much lower MR ratios as well [5]. For fast memory devices, low resistances are favored to reduce the Resistance-Capacitance (RC) time constants. Also, low resistances are favored to reduce Joule heating. But, high MR ratios are needed to increase the signal and thus a higher signal to noise (SNR) ratio.

Current magnetic memory devices (like spin torque RAM or STRAM) use MTJs as storage elements [6], which are composed of an oxide layer (such as MgO) sandwiched

between two ferromagnetic metal layers. These are excellent for today's dimensions with magnetoresistances MR of about 70%. However, the demands of device integration prefer resistances (R) below 300Ω, which means that the resistance-area (RA) products of MTJs must be substantially decreased as device dimensions continue to shrink. This has led researchers to re-examine all-metal "current perpendicular to the plane giant magnetoresistive" (CPP GMR) structures, which are calculated to have high signal to noise ratios at high device densities. Because all metallic CPP GMR sandwich structures have relatively low MR ratios, pioneering attempts have been used to increase the ratio. These included the use of nano-oxide layers (NOL) and Heusler-alloy magnetic soft layers. In NOL devices, co-deposition of Al or Si within the device layers is followed by a controlled oxidation to produce insulating Al-O or Si-O boundaries between the magnetic grains [7,8]. Large variations in grain morphology typically lead to unpredictable device performance even at large sensor dimensions. Heusler-alloy devices require thick seed layers and excess annealing to obtain half-metallic crystal structures [9-11]. And yet, even when the correct structure is obtained, the all-important interfaces often do not exhibit half-metallic properties [12]. In all of these cases, vacuum-deposited thin films were patterned into either ellipsoidal or cylindrical pillars, the smallest of which were 30nm-diameter cylinders. Also, in all cases, the magneotresistance decreased with diameter until it is negligible below 30nm.

A straightforward attempt to increase the magnetoresistance of all metallic CPP GMR structures is to make multilayers of them, which is basically a way of introducing multiple GMR sensors in series which in turn increases the signal obtained and thus the

SNR. Multilayered nanostructures are difficult to fabricate by depositing multilayer thin films and then patterning them into nanostructures using lithography. This is because the resulting structures will have very high aspect ratios (AR) and thus will more than likely fall down on the substrate or to etch unevenly with depth. Therefore, a template assisted deposition, where multilayered nanostructures are deposited directly inside nanoporous templates, is more promising. Vacuum deposition such as sputtering and evaporation cannot be used for high aspect ratio template assisted deposition because these techniques produce line-of-sight depositions and also are very slow techniques. Electrochemical deposition is the ideal solution in this case as it is cheap, fast, and has shown promising results over the past decade [13-18]. Therefore, template assisted electrochemical deposition of multilayered CPP GMR structures has the best potential for future high density storage devices. Even for sandwich structures, electrodeposition can still be favored since it mitigates the side wall damage that is associated with vacuum deposited and patterned structures [18].

Multilayered Co/Cu nanowires are found to be perfect structures that meet the specifications mentioned above for two main reasons. First, Co and Cu are immiscible and thus inter-diffusion of these elements into each other is minimized. Also, the majority Co band is very similar to the majority Cu band whereas the minority bands are very dissimilar [19], Fig. 1.1. This enhances spin polarization and increased the magnetoresistance ratio which are very important quantities for spintronic devices.

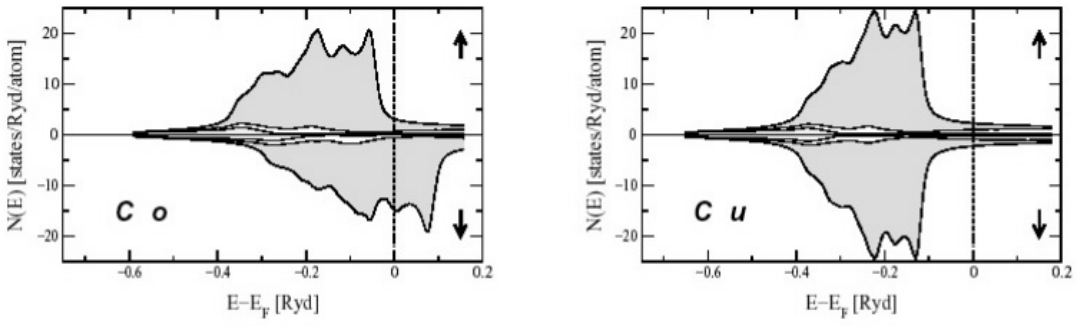

Fig. 1.1. Spin projected densities of states of Co and Cu.[19]

1.2. OBJECTIVES

The main objective of this work is to prove the feasibility of using electrodeposited multilayered nanostructures as future elements in spintronics applications. Applications covered in this work are: magnetic field sensors, and spin transfer torque random access memory (STT-RAM). For magnetic field sensors, the objective is to fabricate small diameter magnetic sensors with low resistance-area (RA) products and decent magnetoresistance (MR) ratio that can be used for ultra-high density magnetic recording. For STT-RAM applications, the objective is to design and fabricate arrays of multilayered nanowires that have low resistance area products, high density and high order, low switching current densities, and the ability to operate at zero bias magnetic fields. All of these properties are to be achieved using the simplest, cheapest, and fastest methods, i.e., electrochemical techniques. Electrochemical techniques are usually given less attention in industries involving state of the art devices because of the belief that electrochemical techniques are inaccurate and produce results with very wide variation. Part of the goals of this thesis is to prove that this belief is wrong.

1.3. ORGANIZATION OF DISSERTATION

In Chapter 1 of this dissertation, the motivation and the objectives of this work will be highlighted. Then a literature survey of electrochemical fabrication of multilayered nanowires and applications will be conducted in Chapter 2. In this chapter, the theories of the different physical phenomena that apply to this research will also be provided.

Chapter 3 provides a COMSOL simulation of the electrodeposition process in porous templates. In this chapter, the required spacing between pores for uniform deposition will be found. Chapter 4 discusses the feasibility of using nanowires as current perpendicular to the plane giant magnetoresistive elements and an overview of different potential applications of these nanowires. Chapter 5 proposes a specific example of using 10nm diameter wires as future read sensors for ultra-high density magnetic recording. In this chapter, fabrication of these small diameter wires will be discussed, followed by resistivity and magneto-transport measurements to prove the concept.

Chapter 6 talks about the feasibility of using Co/Cu multilayered nanowires as future storage elements in spin transfer torque random access memories (STT-RAMs). In this chapter, fabrication of high density wires will be first discussed, followed by spin transfer torque measurements at zero external magnetic fields. The effect of Cu layer thickness will be investigated and the experimental data will be explained by using energy and dipole field arguments. Conclusions and future work recommendations are provided in chapter 7.

Chapter 2

Theory and Literature Survey

2.1. TEMPLATE FABRICATION

As discussed in chapter 1, the most suitable method to fabricate multilayered nanowires is electroplating into nanoporous templates. These templates can be polycarbonate track etched membranes, block copolymers, and anodic aluminum oxide templates [20-22]. In track etch templates; high energy ions are shot onto a polycarbonate template and if the template thickness is thin enough the ions will penetrate through leaving tracks behind them which can be subsequently etched wider to make nanoholes [23]. Therefore, these templates are usually thin (~5um) and have pores are located very randomly. Block copolymer templates have much higher order but the order degrades with the template thickness so these highly ordered block copolymer templates are also usually thin (<50nm) [24]. Anodic aluminum oxide templates can be thick and yet be very ordered. These templates are made by anodizing an aluminum film under the right conditions.

A single anodization step of Al produces templates with pores that vary in size, shape, and branch along the thickness of the template. Therefore, continuous and straight

nanowires are difficult to electroplate into these templates. A novel two-step anodization approach was invented by Masuda which helped achieve more uniformly sized and distributed pores [25]. Thereafter, alumina templates made by two step anodization of aluminum became very popular for electroplating nanowires. Although this method narrowed the size distribution of the pores, the order was short ranged and thus templates made by this modified method cannot be used for fabrication of devices that require long range ordered arrays, like MRAM for instance. However, long range order in alumina templates can be achieved by nanoimprinting the aluminum surface before anodization [26]. Here, a nanopillar stamp made by a hard material such as Si_3N_4 is used to stamp the aluminum surface, and then a single anodization step is performed to achieve the same order of the Si_3N_4 stamp. However, this method requires a master stamp usually fabricated by an electron beam lithography step which is very expensive if large stamps are made. In all of these fabrication cases, the pore size and the center to center spacing of the pores are governed by the anodization parameters like andoization voltage, temperature, and the type of electrolyte and its concentration [27,28].

Alumina templates have been also integrated onto Silicon substrates [29,30]. This eanbles integration of nanowiredevices with transistors, diodes, and other semiconducting devices to drive their operation. However, there is a major challenge in integrating such templates on Si while still using electroplating to make devices inside the pores. This challenge is the formation of an oxide barrier layer at the bottom of the pores at the template/Si interface. This barrier layer also forms when anodizing free aluminum foils but it can be easily removed by floating the resulting alumina template on a chemical

etchant for few minutes [30]. The problem with removing the barrier layer for templates made on Si is that the chemical etchant cannot easily reach the bottom of the pores without also etching the pore walls, so the whole template is etched away. There have been some attempts in smartly removing the barrier layer off templates integrated on Si. One approach is to use ion milling to break the barrier layer but this approach typically requires thin templates for efficient and fast removal of the barrier [30]. Another approach is to put a conductive film like Cu or Au underneath the Al film and use that film as the bottom electrode during anodization. In this case, when the anodization process reaches the bottom of the Al film, the anodizing solution breaks the barrier in attempt to reach the conductive film on the other side of the barrier layer [30]. This only happens for a certain combinations of solution and metallic films because it depends on the reactivity of these two materials. In our work, we found that Cu is highly reactive with oxalic acid and the barrier breaks in a short time. For other metallic films, like Au, the breaking of the barrier takes longer times allowing better control of the process.

In this work, a two-step anodization method was used to make porous templates that were both free standing and on Si. In some cases, commercial templates from Synkera, were used to grow the nanowires.

2.2. TEMPLATE-ASSISTED DEPOSITION

The templates described in the previous section are filled with nanowires using electrodeposition. This uses a very simple setup as shown in Fig. 2.1. Here, two electrodes are placed in an electrolyte containing cations of a certain metal, and a voltage

drop is applied between the electrodes so the cations are electrostatically pulled towards the negative potential electrode. A reduction reaction then takes place and as a result, the metal deposits on the cathode.

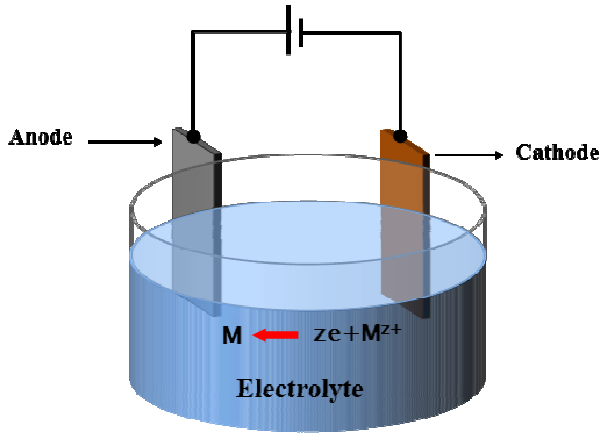

Fig. 2.1. Electroplating cell showing a reduction reaction of M^{+2} cations to metal M at the cathode.

2.2.1. SINGLE ELEMENT NANOWIRES

Here, the cathode in Fig. 2.1 is replaced with a porous template that has a conducting film on its underside. In that case, the cations are attracted to the top of the template, then diffuse down the pores to reach the bottom contact where reduction of the cations deposits the metal inside the pores to form nanowires. Also, the electrolyte here contains cations of only one element and thus single element nanowires are grown inside the pores.

Single element magnetic nanowires like Fe, Ni, and Co have been successfully grown in porous templates by electrodeposition [31-34]. In most of these references, the

aim was to study the magnetic properties of these wires and possible applications. Later in this chapter, the magnetic and structural properties of electrodeposited single element nanowires and multilayered nanowires will be discussed.

2.2.2. MULTILAYERED NANOWIRES

Similar to single element wires, multilayered nanowires use the same electrochemical cell and the same concept. The only difference is that the electrolyte used for the deposition of multilayered nanowires has more than one element. For example, a mixture electrolyte containing Co^{+2} and Cu^{+2} cations is used to deposit Co/Cu multilayered nanowires. Also, because the individual layers of multilayered nanowires may require specific thicknesses (1-100nm), it is considered more challenging to deposit multilayered nanowires. In some applications, like the ones studied in this work, the individual layer thicknesses can be as small as 3nm, so careful control of the deposition of these layers is crucial. Next, the uniformity of single element wires and multilayered wires will be discussed.

2.2.3. DEPOSITION UNIFORMITY

Non-uniform nanowire growth in porous templates has been observed experimentally [15,35]. This has been attributed mainly to the overlapping of diffusion regions which produce less diffusive flux in certain pores and more diffusive flux in other pores, resulting in nonuniform nanowire lengths. Methods to solve for this non-uniformity have been proposed. One for example uses the rotating disk electrode system

to eliminate the time dependence of the diffusion layer thickness during deposition and make the deposition current density as uniform as possible all over the substrate [15]. Another method uses polycarbonate templates which have large spacing between the pores so that diffusion regions of the pores never overlap [36], resulting in completely independent pores. A third method uses pulsed or AC electrodeposition which typically improves the uniformity by a great amount [37]. As a rule of thumb, it has been proposed that a center-to-center spacing of at least twice the diameter of the pores is needed to produce independent deposition and thus uniform deposition inside the pores.

In this work, we first simulated nanowire electrodeposition in porous templates using COMSOL multiphysics 3.5a and proved the twice the diameter rule of thumb. We then used templates that have that condition to insure uniform nanowire deposition. We also used charge controlled deposition [38] which allows to accurate control of the thicknesses.

2.3. MAGNETIC AND STRUCTURAL PROPERTIES OF ELECTRODEPOSITED NANOWIRES

2.3.1. SINGLE ELEMENT NANOWIRES

There has been a vast number of reports about the magnetic and structural properties of template synthesized single element magnetic nanowires. For Ni, Co, and Fe nanowires, the coercivity (H_c) was found to decrease with the diameter of the wire when an external field was applied parallel to the nanowire axis [16,39]. This is due to multidomain formation at larger diameters. The diameter value at which multidomains

start to form is solely dependent on the exchange parameter of the material which is largest for Co allowing a threshold diameter of ~35nm [40].

The anisotropy of Fe and Ni nanowires is dominated by shape ($K_{shape} >> K_u$). For Co nanowires, however, the crystalline anisotropy is large and can be as high as the shape anisotropy. This makes single Co nanowires interesting structures because the magnetization easy axis can be tuned by manipulating the shape anisotropy of the wires.

Because Co is the only magnetic element studied in this work, structural properties of nanowires made of Co is particularly important. It has been shown that the Co deposition voltage and the pH of the Co^{+2} containing electrolyte both play a big role in determining the structural properties of the deposited Co nanowires.

Darques et *al.* showed that deposition from a high pH electrolyte results in Co nanowires that have hcp Co grains with their c-axes aligned with the wire axis, resulting in along the nanowire crystalline anisotropy [41,42]. Similarly, they also showed that deposition from a lower pH electrolyte results in hcp grains aligned perpendicular to the nanowire axis, indicating a perpendicular to the wire crystalline anisotropy. At extremely low pH, they showed that the deposited wires have fcc Co grains that have random directions, resulting in nearly zero anisotropy. The effect of the deposition voltage or the current density was shown to have the same effect (i.e., higher voltages or current densities result in perpendicular anisotropy and vice versa). The orientation of the c-axis is extremely important when making devices as will be clearly seen in the content of this work.

2.3.2. MULTILAYERED NANOWIRES

The effect of layering in Magnetic/Nonmangetic nanowires on the magnetic properties can be very interesting. For example, in 50nm diameter Co(50nm)/Cu(5nm) multilayered nanowires, H_c was found to be higher than that of same diameter Co nanowires due to their single domain nature and strong shape anisotropy [43,44].

Medina et *al.* showed that the shape anisotropy of Co/Cu multilayered nanowires can be perfectly tuned by the proper design of the aspect ratios of the individual layers [45]. It can be either along the nanowire axis, perpendicular to wire axis, or even zero. With the proper selection of crystalline anisotropy, as described in Ref. 41, the total anisotropy of the multilayered nanowire can be selected. This tool is really useful and is used in our work as will be visited in great detail in chapter 6.

The structural properties of the Co layers in Co/Cu multilayered nanowires are the same as those for single element nanowires [46]. In other words, the direction of the c-axis of the Co hcp grains can be selected using the pH of the electrolyte or the deposition voltage, similar to single element nanowires. Similar to bulk Cu, the crystal structure of the Cu layers in electrodeposited Co/Cu multilayered nanowires is fcc [47].

Because Co/Cu multilayers are usually deposited from a mixture electrolyte containing both $CoSO_4$ and $CuSO_4$, and because the reduction potential of Co^{+2} is higher than that for Cu^{+2}, there is always Cu inclusions in the Co layers. It was found that the Cu impurities in the Co layers deposited at -1V from a solution that contained 155 g/l CoSO4.7H2O, and 1.13 g/l CuSO4, were 7% due to the codeposition of Cu and Co at -1V [47]. The Co impurities in the Cu layers were found to be less than 1% because the

deposition potential of Cu (-0.56V) is less than that of Co.

Although Cu inclusions in the Co layers sound unwanted, it was found useful in some cases. For example, in this work we found that the Cu impurities caused the saturation magnetization (M_s) and the anisotropy constant (K_u) of Co to decrease which, for a fairly sized element (K_uV/kT large enough for thermal stability), was found useful because it reduces the external energy needed to switch the magnetization. This will be discussed in much greater details in chapter 6 but the main idea is that K_u and M_s were reduced by adding Cu to the Co layers, which resulted in less spin polarized currents needed to switch the magnetization from one direction to another in spin torque RAM elements.

2.4. GIANT MAGNETORESISTANCE (GMR)

Giant magnetoresistance is a quantum mechanical effect occurring in structures of alternating magnetic and nonmagnetic layers. It is based on the electrical resistance shift when two ferromagnetic layers sandwiching a nonmagnetic layer have either aligned anti-aligned magnetizations. This effect was discovered independently by Albert Fert and Peter Grunberg in 1988, who were awarded the 2007 Noble Prize in Physics for their discovery [3]. Their discovery was based on Fe/Cr superlattices at T=4.2K. They found a huge decrease in resistance when two adjacent Fe layers are aligned, Fig. 2.2. Here, at very large field, all the Fe layers have aligned magnetizations and the resistance is smallest (R_L). At zero field, the Fe layers align antiferromagnetically mainly through RKKY exchange coupling and the resistance is highest (R_H). The change in resistance is

higher for thinner Cr layers due to the higher antiferromagnetic coupling at thinner Cr which results in larger R_H. But, here the resistance is normalized and only $\Delta R/R$ can be seen. A ratio defining the strength of the magnetoresistance was historically defined as:

$$GMR(\%) = \frac{R_H - R_L}{R_L} \times 100 \qquad (2.1)$$

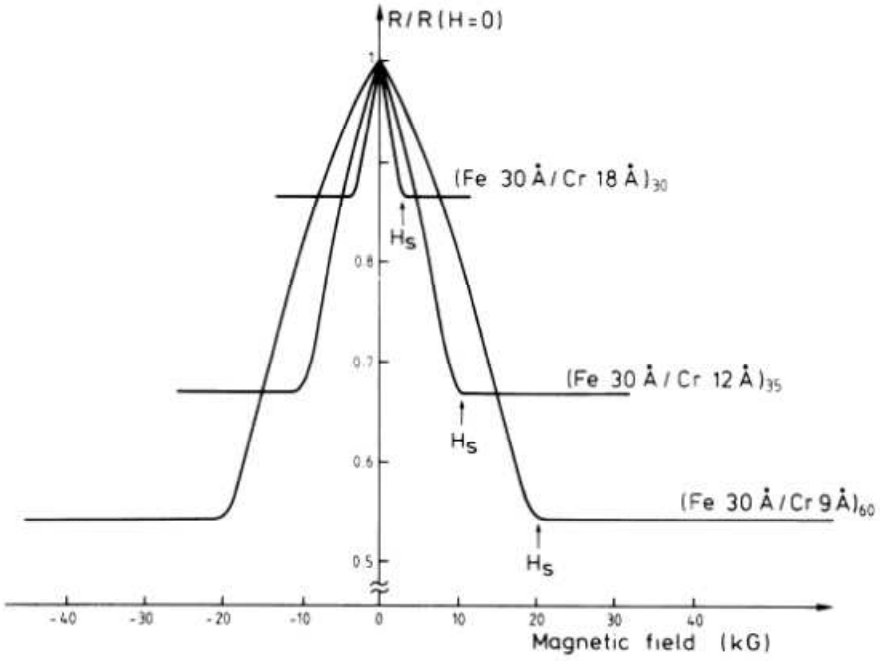

Fig. 2.2. In-plane normalized resistance for Fe/Cr superlattices with different Cr thicknesses and number of layers. Field and current are applied in plane of the layers.[3]

To understand the principle of GMR, the two-current or the two parallel resistance model can be used [48], Fig. 2.3. Here, if the two ferromagnetic layers have aligned magnetizations, then one spin direction of the sense current has little scattering (R_1) and

the other spin direction has much higher scattering (R_2). In this case, the total sandwich structure resistance is low (R_L) given by:

$$R_{\uparrow\uparrow} = \frac{2R_1R_2}{R_1 + R_2} \qquad (2.2)$$

On the other hand, when the two ferromagnetic layers have antialigned magnetization, both spin directions have an average scattering of $(R_1+R_2)/2$. Here, the total resistance of the structure is high (R_H) can be written as:

$$R_{\uparrow\downarrow} = \frac{R_1 + R_2}{2} \qquad (2.3)$$

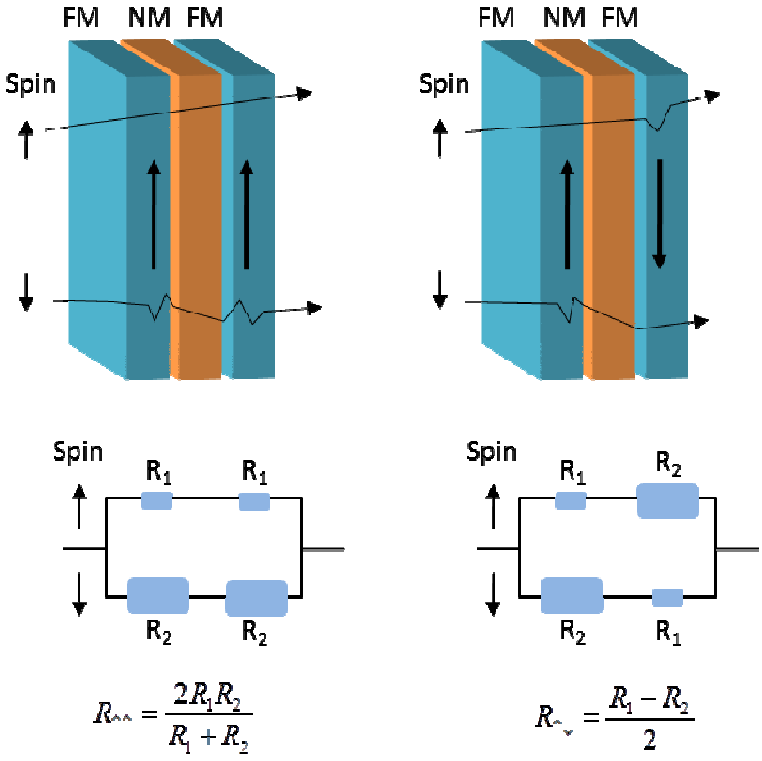

Fig. 2.3. Two current model for the giant magnetoresistance of multilayers.

The GMR ratio using such model can be calculating by substituting (2.2) and (2.3) in (2.1). This gives:

$$GMR(\%) = 100 \times \frac{(R_1 - R_2)^2}{4R_1R_2} \qquad (2.4)$$

As can be seen in (2.4), the GMR ratio can be increased by making R1 as small as possible. The theoretical maximum of equation (2.4) is ∞ but this is not realistic in practice.

Applications of GMR include magnetic field sensors, as in read sensors for hard disk drives, and magnetic random access memories. In read sensors, different magnetic fields from the bits ("0" or "1") cause different resistance readings in the sensor based on the GMR effect, and by passing a bias current in through the sensor a voltage signal is generated. In magnetic random access memories (MRAMs), an external magnetic field is used to write the bits, which can be GMR elements, and the signal is read using the same principle. Increasing density in these devices can be problematic when high densities are reached. This is because the external magnetic field will likely write adjacent bits and thus errors occur. To overcome this, people have developed a MRAM that uses spin polarized current injected through the bit to switch the magnetization from one direction to another based on the so called spin transfer torque (STT) effect [49-52]. MRAMs based on this effect are often called STT-RAM and have been first made commercially available by Sony in 2005. In the next section, the physics of the spin transfer torque effect will be discussed. In chapter 6, we will show spin transfer torque results of multilayered nanowires that are proposed as future elements for STT-RAMs.

2.5. SPIN TRANSFER TORQUE (STT)

In a structure as shown in Fig. 2.4, where fixed and free ferromagnetic layers sandwich a nonmagnetic layer, electrons passing through the fixed ferromagnetic layer will be polarized by the magnetization of that layer, i.e., more spin-up electrons than spin-down electrons. This polarized current will then pass through the free ferromagnetic layer and will exert a torque on its magnetization trying to align it with the magnetization of the fixed magnetic layer. If the torque is enough (i.e., enough current density), the magnetization of the free layer will be kicked out of equilibrium and will rotate until it reaches a minimum and stable energy state, which in this case, is when the two magnetizations are parallel to each other.

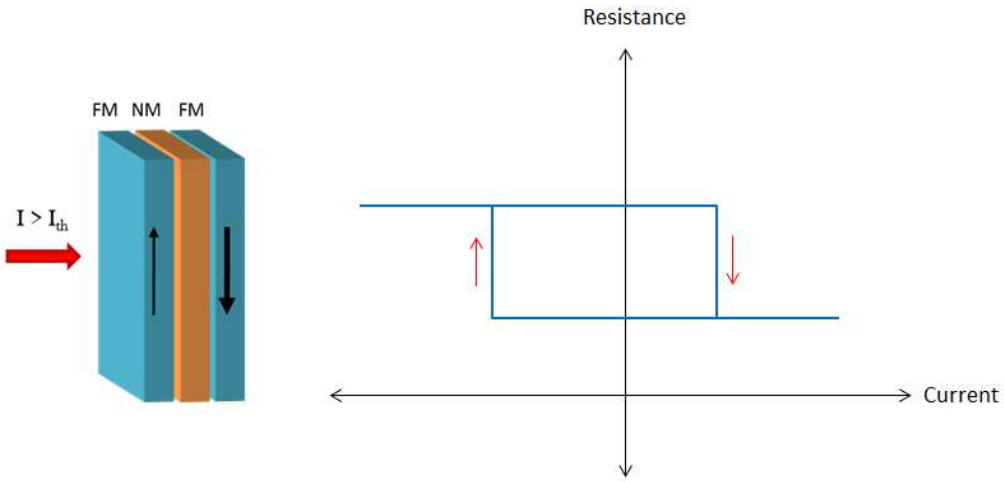

Fig. 2.4. Schematics of the spin transfer torque effect.

The mechanism of bringing the two magnetizations back to the antiparallel state is similar but requires the current direction to be flipped. In this case, electrons will pass through the free layer first, to the nonmagnetic layer and finally hit the fixed layer. Electrons with similar polarization to the fixed layer will pass through while electrons with opposite spins get reflected back and exert their torque as they reflect back to the free layer. Eventually, and at some sufficient current, the magnetization of the free layer will switch back to the antiparallel state, which is another minimum energy state. The results of STT switching experiments are usually interpreted by plotting the resistance versus current, as shown in the schematics of Figure 2.4. This is because the resistance changes with the relative alignment of the magnetizations according to the GMR effect discussed in section 2.5.

The spin transfer torque is usually given by [139]:

$$T_{STT} = -\gamma \frac{J\hbar}{etM_s} \hat{M} \times (\hat{M} \times \hat{p}) \qquad (2.5)$$

where γ is the gyromagnetic ratio, J is the current density, $\hbar$ is Planck's constant, *e* is the electron charge magnitude, *t* and Ms are the thickness and saturation magnetization of the free layer, respectively. $\hat{M}$ and $\hat{p}$ are unit vectors along the free and fixed layer magnetizations, respectively. As seen in equation (2.5), the torque equals zero when $\hat{M} \times \hat{p}$ equals zero, and this is what makes the switching occur between two stable states (parallel or antiparallel).

This interesting phenomenon allows for accurate manipulation of the magnetization of a ferromagnetic layer using a spin polarized current injected through the layer. The

current density needed to do this is under the aid of external magnetic fields is usually on the order of 10^6-10^8 A/cm^2. In chapter 6, we will show STT switching results obtained not in sandwich structures, but in multilayers of ferromagnetic/nonmagnetic layers, all without the need for external fields.

2.6. COUPLING MECHANISMS IN MAGNETIC MULTILAYERED NANOWIRES

In this section we will discuss the coupling mechanisms between ferromagnetic layers in multilayered ferromangnet/nonmagnet nanowires. We will first consider the interactions between successive ferromagnetic layers in a single wire, called intra-wire interactions. Then we will discuss the interactions between ferromagnetic layers from different wires in the array, namely inter-wire interactions.

2.6.1. INTRA-WIRE COUPLING

Coupling here occurs between successive ferromagnetic layers inside a single nanowire. There are different types of coupling in this case and these are exchange coupling, dipole field or magnetostatic coupling, Orange-Peel coupling, and Ruderman-Kittel-Kasuya-Yosida or RKKY coupling. The strength of inter-wire coupling vary depending on the distance between layers, strength of the magnetic layer (M_s and K_u), roughness of interfaces, and quality of the spacer layer. We will study each of these types and discuss how big the effect is in electrodeposited Co/Cu multilayered nanowires.

2.6.1.1. Exchange Coupling Through Pinholes

Exchange coupling in magnetic materials is a quantum mechanical effect that results in electrons preferring similar spin directions. Because magnetic moment is connected with the spins of electrons, materials with higher exchange coupling capability tend to have larger single domain grains. This capability is usually referred to as the exchange parameter or exchange constant "A". For example, cobalt has a higher exchange constant than Fe or Ni, resulting in larger domain size.

In continuum, the exchange energy is given by:

$$E_{ex} = A(\left|\nabla M_x\right|^2 + \left|\nabla M_y\right|^2 + \left|\nabla M_z\right|^2) \qquad (2.6)$$

where A is the exchange constant, ∇M_x is the gradient of the x-component of magnetization. Single domains are formed to minimize this energy. As clearly seen in equation 2.6, the exchange energy is minimized when the material has uniform magnetization ($\left|\nabla M_x\right| = \left|\nabla M_y\right| = \left|\nabla M_z\right| = 0$), i.e., single domains.

Counter to this effect, there is magnetostatic energy that is large within single domains. In magnetic materials, exchange and magnetostatics usually compete and the result is multi-domains with certain domain wall widths and domain size.

In Co/Cu multilayered nanowires, if the Cu layers are not deposited uniformly, or are too thin, there may be pinholes through the layer which connect the two adjacent Co layers. If this happens, exchange coupling between the Co layers may take place, resulting in two adjacent Co layers having similar magnetization directions. Of course this is unwanted because it defeats the goal of having high GMR from multilayers.

2.6.1.2. Dipole Field Coupling

Dipole field coupling is a type of magnetostatic coupling that occurs between two magnetic elements that are placed next to each other such that the total magnetostatic energy of the system is minimized. Here, the magnetic flux from each element closes into the flux of the other element. This type of coupling enhances the stability of each magnetization by introducing a dipole field H_{dip} in the same direction as the magnetization. The magnitude of H_{dip} is inversely proportional to the cube of the distance between the layers and thus very sensitive to the spacing between the layers.

$$\vec{H}_{dip} = \frac{3\hat{n}(\hat{n}.\vec{m}) - \vec{m}}{\left|\vec{x}\right|^3} \qquad (2.7)$$

where $\vec{m}$ is the magnetic moment of the source point, and $\hat{n}$ is a unit vector between $\vec{m}$ and the observation point. Note that the magnetic moment of the other element is not included in this equation because we are only measuring the magnetic field from one element onto the other. Therefore, for a system of two magnetic elements, equation 2.7 is used to find the dipole field from each element onto the other. Of course, this equation assumes point sources so it is just an approximation.

In Co/Cu multilayered nanowires the dipole field acting on each Co layer is a sum of the individual fields coming from all adjacent layers. Because this field scales with $1/(\text{distance})^3$, only the few nearest neighbor layers contribute to the total field seen by a given layer. We will discuss the magnitude of dipole fields seen in Co/Cu multilayered nanowires in chapter 6.

2.6.1.3. Neel Coupling

Neel or orange-peel coupling is a magnetostatic effect that occurs due to rough interfaces. Suppose that we have a sandwich FM/NM/FM structure with rough interfaces as shown in Fig. 2.5. Then beside the dipole or magnetostatic field (H_{dip}) that forms between the two FMs, there exists a field H_n that is opposite in direction to H_{dip}. This field (H_n) is called the Neel field and it is a magnetostatic field that arises from the magnetic positive surface charge formed at the rough interface [53].

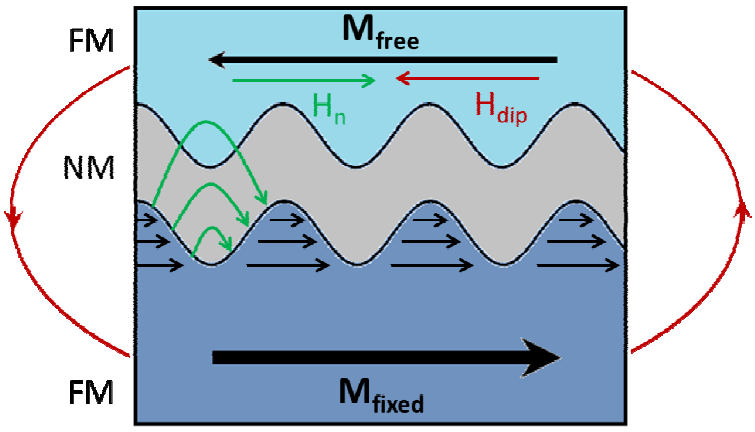

Fig. 2.5. Schematics of the origin of Neel "orange-peel" coupling in sandwich structures with rough interfaces

In electrodeposited Co/Cu multilayers, the interfaces roughnesses are unknown, but are likely to be similar to vacuum deposited structures since low resistance and spin transfer torque switching have been seen in electrodeposited devices. Hence the Neel field can be ignored in these structures.

2.6.1.4. RKKY Coupling

Ruderman-Kittel-Kasuya-Yosida (RKKY) coupling is the interaction of localized magnetic moments in a nonmagnetic host by interacting through the conduction electrons [54,55]. It is also often called interlayer exchange coupling. RKKY interaction oscillates between antiferromagnetic (AF) and ferromagnetic (F) coupling as a function of the nonmagnetic layer thickness [56]. Therefore, this thickness can be tuned to achieve either AF or F coupling depending on the application. The interlayer exchange coupling can be approximated as:

$$E_{ex} = c(\hat{M}_1 \cdot \hat{M}_2)\frac{\cos(kr)}{r} \qquad (2.8)$$

where $\mathbf{M_1}$ and $\mathbf{M_2}$ are the localized moments, k is the magnitude of the propagation vector, and r is the distance between $\mathbf{M_1}$ and $\mathbf{M_2}$. As seen in equation (2.8), the coupling strength decreases as it oscillates and becomes negligible at very small thicknesses (~3nm for a Ru host) [56]. In our electrodeposited Co/Cu nanowires, small thicknesses of Cu are avoided and thus RKKY coupling is suppressed. In this case, the dipole field is the stronger effect and is responsible for antiferromagnetically couple the adjacent Co layers at remanance.

2.6.2. INTER-WIRE COUPLING

Inter-wire coupling between adjacent wires can affect the magnetic properties of the nanowires in an array. It has been shown that nanowires grown in an array have smaller coercivities than single nanowires [57]. Arrays also result in canting of the

hysteresis loop and a reduced remanent magnetization (Mr) [58,59].

For nanowires saturated along the axis, the inter-wire dipolar field between the wires can be expressed as [59]:

$$H_{dip} = 6\pi PM_s \qquad (2.9)$$

where P is the porosity of the wires defined as the ratio of the nanowires area by the total area of the template. Intuitively, the porosity depends on the spacing between the nanowires and thus the inter-wire dipolar field can be suppressed if the distance between the wires is made large enough.

For multilayered nanowires, a modified form of equation (2.9) is needed such that it includes the effect of layering. In chapter 6, the layering effect will be taken into account and the inter-wire dipolar field for our multilayered nanowire arrays will be calculated.

Chapter 3

Simulation of nanowire electrodeposition inside porous templates

3.1. INTRODUCTION

In recent work, devices made by electrodeposition have been proposed for magnetic random access memories [14] and for read sensors in future 1-10 Terabit/in^2 magnetic recording systems [17] using electrochemical deposition in nanoporous templates. These devices, however, require uniform deposition and repeatable results. This is extremely important because for these devices, thin layers (as small as 3nm) are required. Although physical deposition techniques such as sputtering and evaporation can be used to deposit such thin layers, here the proposed devices [14,17] are composed of multilayers (as many as 500 layers) which are difficult to achieve through physical techniques due to the very long deposition times involved in these processes. Therefore, control over the uniformity of structures made by electrodeposition is crucial.

Non-uniform nanowire growth in porous templates has been observed experimentally [15,35]. This has been attributed mainly to the overlapping of diffusion

regions which produces less diffusive flux in certain pores and more diffusive flux in other pores, resulting in nonuniform nanowire lengths. Methods to solve for this non-uniformity have been proposed. One, for example, uses a rotating disk electrode system to eliminate the time dependence of the diffusion layer thickness during deposition and make the deposition current density as uniform as possible all over the substrate [15]. Another method uses polymer templates called polycarbonate templates that have large spacing between the pores so that diffusion regions of the pores never overlap [36], resulting in completely independent pores. A third method uses pulsed or AC electrodeposition which typically improves the uniformity by a great amount [37]. As a rule of thumb, it has been proposed that a center-to-center spacing of at least twice the diameter of the pores is needed to produce independent deposition and thus uniform deposition inside the pores.

In this project, we will simulate electrodeposition of copper in a single pore and multipore templates using COMSOL Multiphysics 3.5a. We will study the effect of pore aspect ratio and interpore spacing on the uniformity of the deposition. For single pore templates, the uniformity measure will be the ratio of deposit thickness near the edge of the pore to the thickness at the center of the pore. For multi-pore templates (typically named porous templates) only three pores are considered, and the uniformity measure is then defined as the ratio of deposit thickness in the outer pore to the thickness in the middle pore.

Primary current distributions have been successfully calculated for recessed electrodes [60-62]. However, these cannot be applied to our project here because of two

reasons. First, kinetics involved at the electrodes were neglected in these calculations. Second, these calculations are for single slots (pores) and thus they cannot be used to model the deposition in multi-pore templates.

For simulation using COMSOL, we started with the Cu electrodeposition model provided by COMSOL [63] where deposition occurs on a recessed cathode and modified it such that deposition occurs on only the bottom of the recess (left schematics of Fig. 3.1). This model assumes stagnant $CuSO_4$ solution with no supporting electrolyte so only migration and diffusion terms are included in the overall deposition current. It also assumes Butler-Volmer (B-V) kinetics and uses transient analysis to monitor the deposition over time. The most important feature in this model is that it accounts for the moving cathode during the simulation and therefore moves the cathode boundary conditions as deposition progresses. This is very important for realistic modeling of what happens experimentally. The constants and expressions used in the simulation are the same as those given in Ref. 63 with only the exchange current density being changed to $50A/m^2$ in this project. This was important to get longer deposition times before the solution in COMSOL diverged.

3.2. SIMULATION OF ELECTRODEPOSITION PROCESS

We start this section by first simulating mass transport in single pore templates, where only the depth of the pore is studied. Then we will move to considering the more general case where multiple pores are studied. Here, for simplicity, the pores are assumed to be trenches with 4μm width, infinite length (1m), and variable depth. We varied the

depth of the trenches such that the aspect ratio (AR), defined as the ratio of the pore depth to the pore width, is increased from 0 to 60, Fig. 3.1.

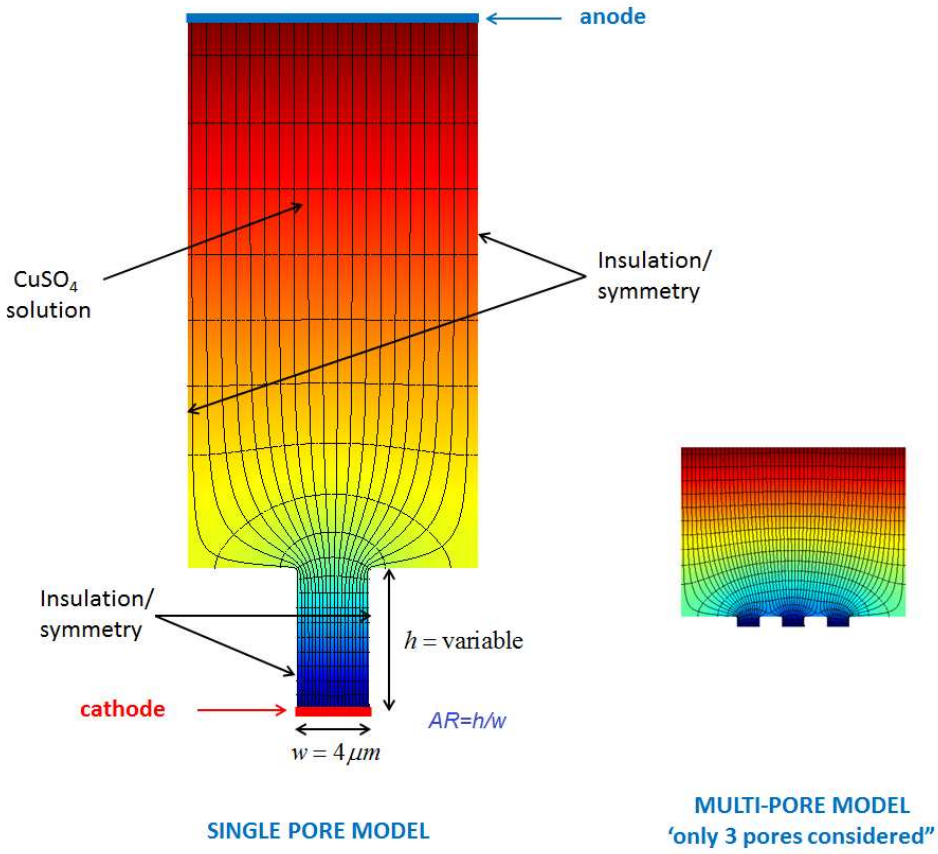

Fig. 3.1. Schematics of the cells used in COMSOL for both single pore templates and multi-pore templates.

3.2.1. SINGLE PORE TEMPLATES

As mentioned before, the width of the pore is fixed here at 4um and the depth is varied from 0µm to 240µm. For generality, we present our results in terms of aspect ratios which will take values from 0 to 60. Although commercial templates have much

higher aspect ratios (up to 10,000) [64], the study presented here gives an idea of what should be expected for extremely deep pores.

Figure 3.2 shows the simulation results of the single pore geometry (left schematics of Fig. 3.1) for simulations times up to 1.5s and for a pore of aspect ratio of 2. The upper limit in the simulation time was determined by when the solution diverged. The solution usually diverged when the moving mesh hit a corner or a fillet corner. Fig. 3.2a shows the normalized current density across the cathode. As seen, the current distribution becomes more non-uniform as deposition progresses. However, the deposition has been shown to be still under control and Cu deposited almost uniformly across the cathode, Fig. 3.2b. We think the valleys seen near the edges of the pore in Fig. 3.2b are due to the fact that diffusive species have difficulty reaching the corner of the pore, reducing the total amount of flux approaching the corner and hence the lesser deposition on the corners. Fig. 3.2c shows the potential profile along a vertical line connecting the midpoints of the anode and cathode. Similar curves are shown for an aspect ratio of 60 in Fig. 3.3.

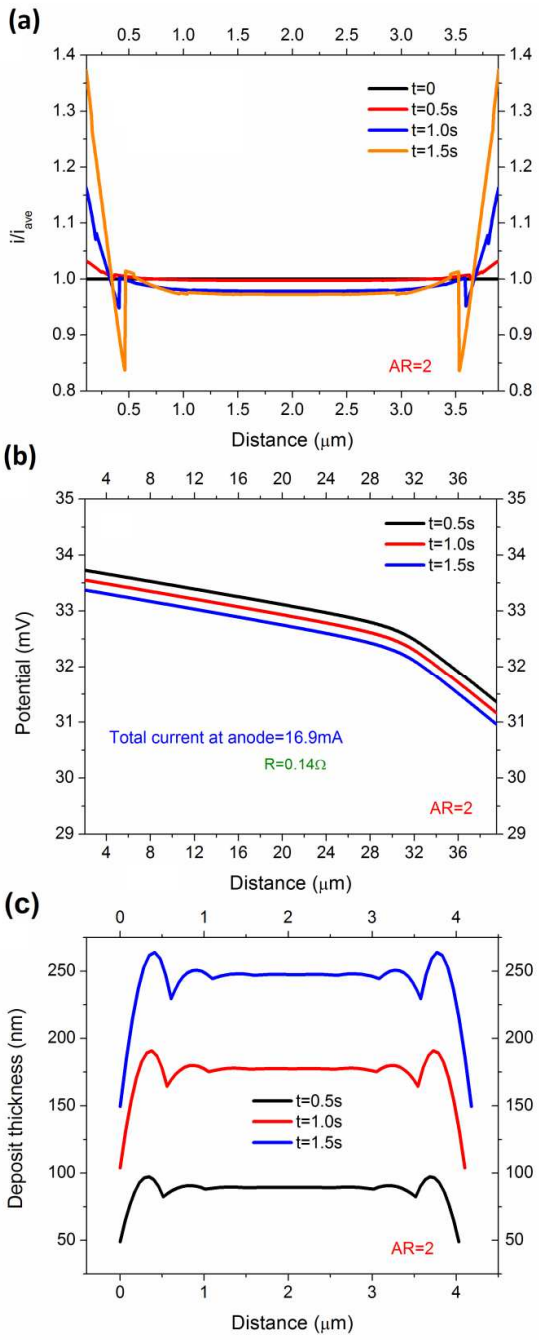

Fig. 3.2. COMSOL simulation results of single pore templates of aspect ratio=2. (a) Current distribution (b) Deposit thickness (c) Potential distribution.

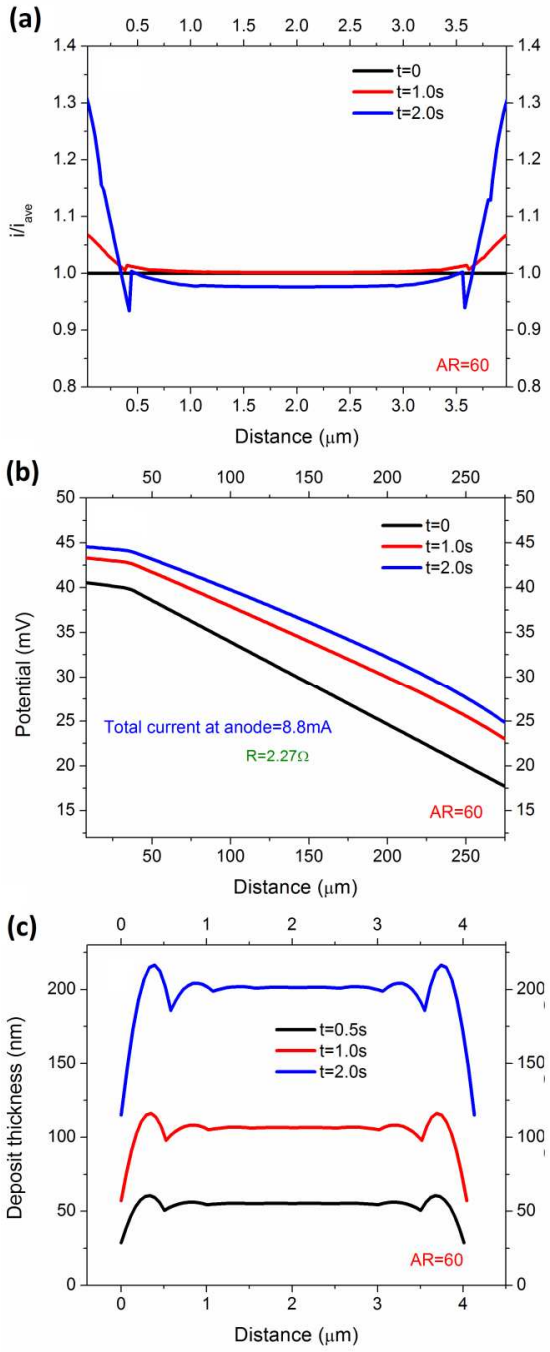

Fig. 3.3. COMSOL simulation results of single pore templates of aspect ratio=60. (a) Current distribution (b) Deposit thickness (c) Potential distribution.

Figures 3.4 and 3.5 show the concentration profile across the top of the pore and across the solution for cells with aspect ratios of 2 and 60, respectively. It is important to note that the concentration is almost uniform across the top of the higher aspect ratio pore meaning that diffusion boundary layers do not extend to the top of the pore and all the diffusion is taking place deep down the pores. However, for the low aspect ratio pores, the diffusion boundary layer does extend to the top of the pore which might not be a problem for single pore templates. As we will see later, this will be a big problem in multi-pore templates and will be the origin of the observed nonuniform deposition.

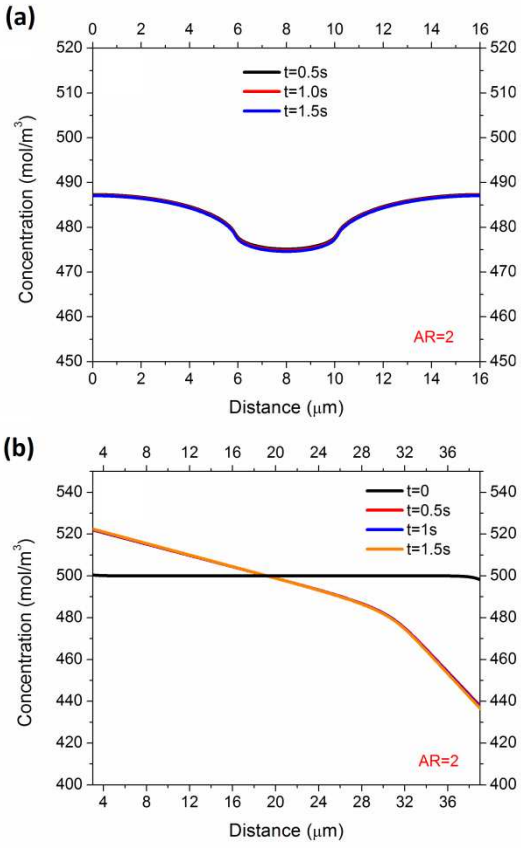

Fig. 3.4. Concentration profiles for electrodeposition in single pore templates with aspect ratio=2.

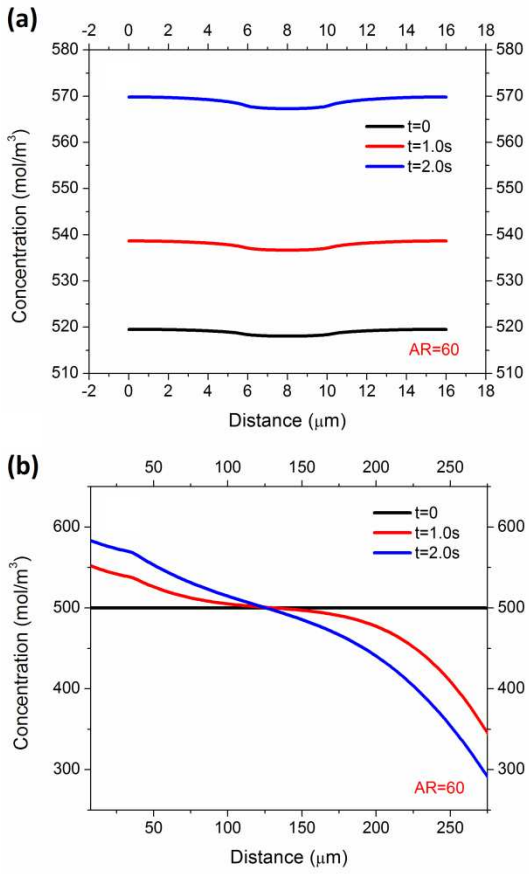

Fig. 3.5. Concentration profiles for electrodeposition in single pore templates with aspect ratio=60.

Figure 3.6a shows the electrolyte resistance and deposition rate for the single pore geometry as a function of the aspect ratio of the pore. As seen, the resistance increases linearly with the aspect ratio and this is expected because the total length of the electrolytic cell increases with aspect ratio and the resistance increases linear with the length. Later in the text, we will provide a simple model based on the geometrical resistances of the cell that agrees very well with the data of Fig. 3.6a, and the origin of

the linearity will be clarified. The deposition rate decreases monotonically with aspect ratio. This is because the deposition rate follows the same shape of the current which has a 1/AR dependence since both I=V/R and R increases linearly with AR. Fig. 3.6b shows the uniformity measure of the deposition in single pore template. Here, the current density and deposit thickness on the edge of the pore are divided by those at the center of the pore. As seen, the deposit becomes more uniform at high aspect ratios. Projecting this to deposition, this means that for single pore templates the deposition starts out uniform and as soon as the deposition approaches the surface of the pore, it becomes less uniform, but not by much (see y-axis values of Fig. 3.6b). Figure 3.6c shows the diffusion boundary layer thickness as a function of the aspect ratio. This agrees with what we said earlier on Figures 3.4 and 3.5 in that the diffusion regions can reach the surface of the pore if the pore is shallow. Although this is not important for single pore templates, it is extremely important for porous templates where overlapping of diffusion regions in shallow pores cause nonuniform deposition in these pores. This will be further explored in the next section where we simulate deposition multipore templates.

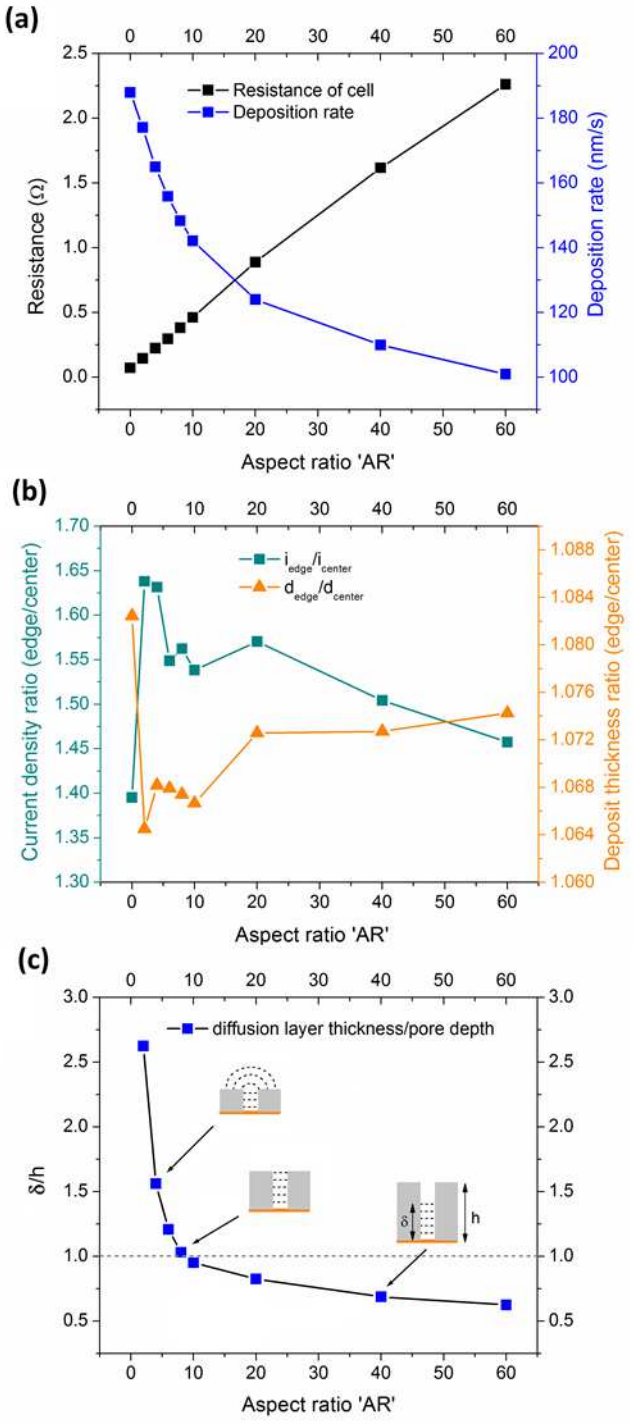

Fig. 3.6. Summary of results for simulated electrodeposition in single pore templates.

3.2.2. CLOSE-PACKED POROUS TEMPLATES

Here, we consider three pores and varied both the spacing between them and the aspect ratio of the pores. Figure 3.7 shows the thickness ratio, defined as the ratio of the deposit thickness in the outer pores to the deposit thickness in the inner pore, as a function of the aspect ratio of the pores for different center-to-center spacing. Here, it is seen that the thickness ratio decreases monotonically towards a value of 1 when the aspect ratio increases. Interestingly, when the spacing is 2 times the width of the pore, the thickness ratio still showed dependence on the aspect ratio, but by 3 times the width, the deposition is fairly uniform all the way to the top of the pore.

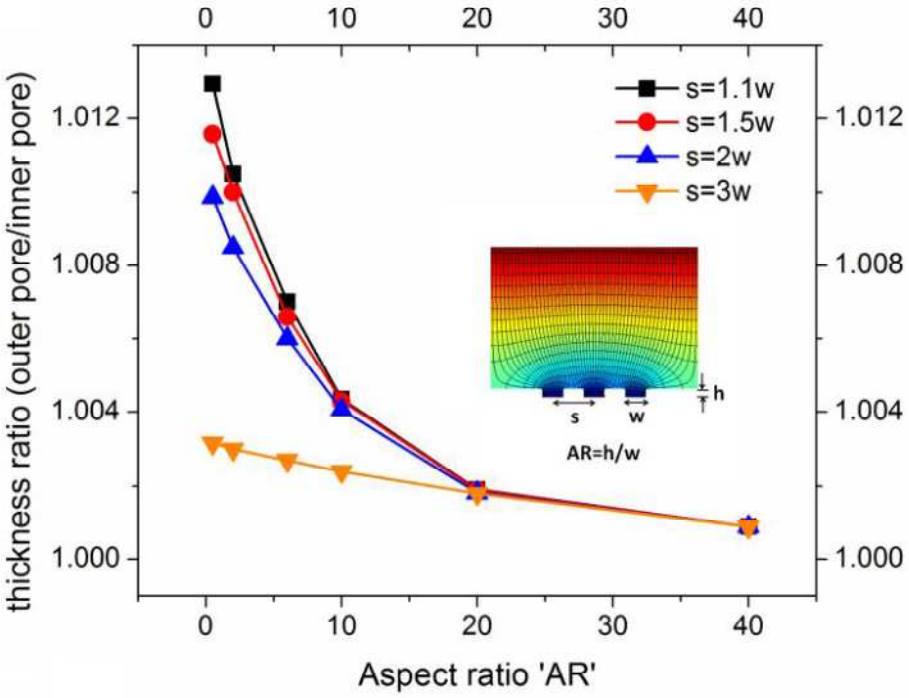

Fig. 3.7. Summary of simulated deposition in multi-pore tmeplates.

Figure 3.8 shows the electrolyte resistance of the 3 pore system as functions of the aspect ratio and spacing between the pores. Fig. 3.8a shows a linear dependence of the resistance on the aspect ratio when the center-to-center spacing was 3*w, where w is the width of the pore. This is similar to the results above for single pores. Fig. 3.8b shows the resistance of the 3-pore system as a function of the spacing between the pores. As seen, the resistance decreases as the spacing increases. This is only true for the 3-pore system where increasing the distance between the pores decreases the resistance because the diffusiong regions overlap less. This result should not be confused with conventional porous templates where the higher the density of pores (less spacing) the smaller the resistance. It is seen from the trend of Fig. 3.8b that the resistance would level out at higher spacings which is expected because the pores will no longer influence each in this case.

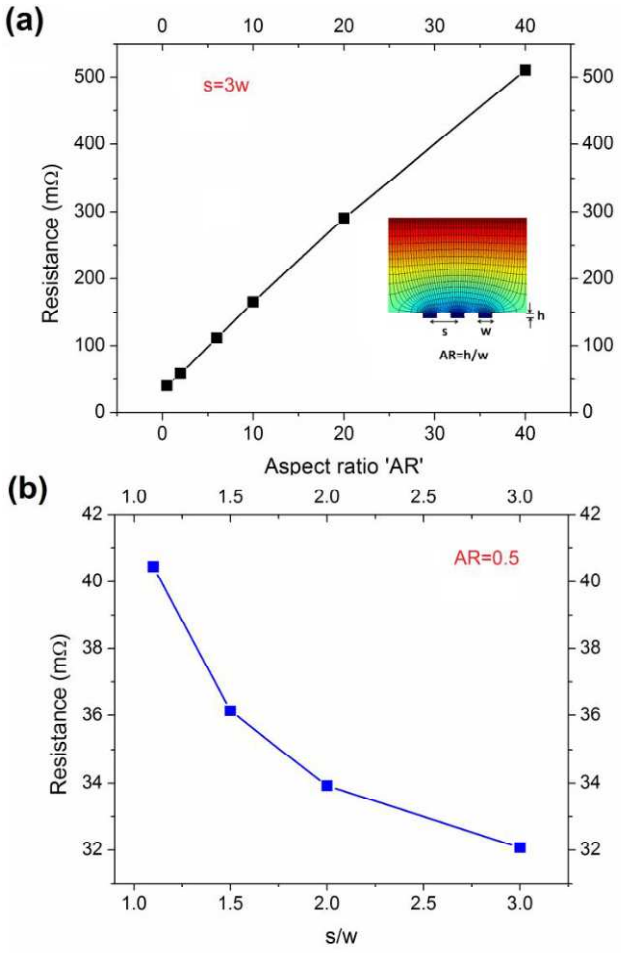

Fig. 3.8. Simulated resistance of multi-pore templates during electrodeposition.

3.3. ANALYSIS OF RESULTS

3.3.1. RESISTANCE MODEL TO FIND CONDUCTIVITY OF ELECTROLYTE

As seen in Fig. 3.6a and Fig. 3.8a, the resistance of the cell exhibits a linear dependence on the aspect ratio for both the single pore and multi-pore models. In this section, we are using simple geometrical resistances to model the linear behavior seen in our data. We assume no dependence on the spacing between the pores (i.e., large spacing,

see Fig. 3.8b). Therefore, our mission here is to analyze the data of Fig. 3.6a (single pore results) and Fig. 3.8a (multi-pore with *s/w*=3). First we start with writing the general equation of a line in the x-y space.

$$R(AR) = R_0 + slope * AR \qquad (3.1)$$

where R_0 is the y-intercept observed in our data. We need to determine the slope for the two cases studied here (i.e., for the single pore and multipore templates). Figure 3.9 below shows a proposed simplified model of the total geometrical resistance of our cell for both the single pore and 3-pore templates. Again, the spacing between the pores is assumed to be large so that interpore effects are minimized (see tail of Fig. 3.8b).

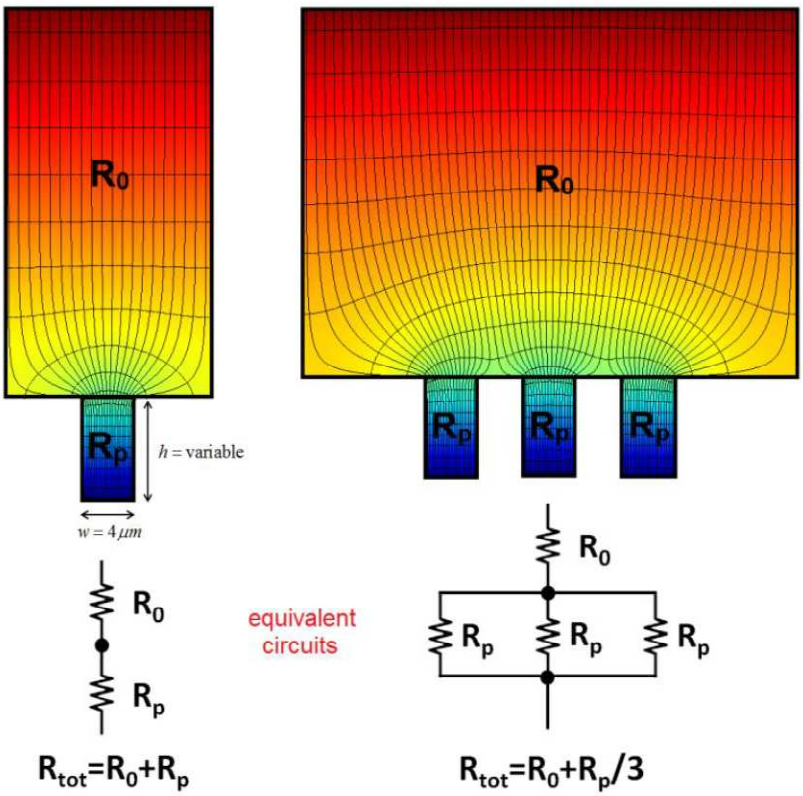

Fig. 3.9. Equivalent circuit model of single and multi-pore cells used in our simulation.

In this model, R_0 represents the resistance of the cell without any pore or with pores of aspect ratio of 0. Note that R_0 is different in both cases due to the different dimensions of the zero aspect ratio cell in both cases. According to the equivalent circuit model shown in Fig. 3.9, the total resistance of the cell including N number of pores is given by:

$$R = R_0 + \frac{R_p}{N} \qquad (3.2)$$

where R_p is the geometrical resistance of the pore and is given by:

$$R_p = \frac{h}{\kappa A} \qquad (3.3)$$

where *h* is the depth of the pore, κ is the conductivity of the solution, and *A* is the cross sectional area of the pore given by $A=w*z$, where *z* is the inward dimension and usually set to 1m in COMSOL. Substituting eq. 3.3 in eq. 3.2 and using $AR=h/w$ and $A=w*z$ yields:

$$R = R_0 + \frac{1}{N\kappa z} * AR \qquad (3.4)$$

This means the slopes of the data in Fig. 3.6a and Fig. 3.8a are given by 1/Nκz where N=1 for Fig. 3.6a and N=3 for Fig. 3.8a. To verify the validity of this model, we checked the actual slopes of figures 3.6a and 3.8a and it was found that the slope of the resistance curve of Fig. 3.6a (36.5mΩ) is 3.067 times larger than that of Fig. 3.8a (11.9mΩ) which is very close to 3 (the value of N). In addition, we took one step further in trying to estimate the conductivity of the solution from the slope of the data. Using a value of z=1m, the conductivity of the solution was estimated to be 27.4 S/m and 28 S/m using

data of Fig. 3.6a and Fig. 3.8a, respectively.

3.4. CONCLUSIONS

In this project, we successfully simulated the electrodeposition of Cu in single and multi-pore templates using COMSOL multiphysics. For single pore templates, the deposition was found to start uniformly across the pore. As the deposit approaches the surface of the pore, the deposition becomes non-uniform in the sense that it gets thicker on the sides than in the middle of the pore. However, the difference in these thicknesses is extremely small so the issue of inter-wire non-uniformity is, in our opinion, not important. For multi-pore templates, however, the deposition starts uniformly across the pores and as the deposition approaches the surfaces, diffusion regions from the different pores start to overlap due to the decreased aspect ratio. This causes less deposition in some pores and more deposition in others. This was solved by increasing the spacing between the pores. It was found that when the center-to-center spacing between the pores is three times the width of the pores the interpore non-uniformity is minimized, resulting in uniform thicknesses in all the pores.

The total resistance of the multi-pore template deposition cell having N number of pores with large center-to-center spacing was analyzed and an equation relating the resistance to the different parameters was derived. Resistances evaluated from this equation were shown to have great agreement with the simulated resistances. Furthermore, this equation along with the simulated data was used to estimate the conductivity of the $CuSO_4$ solution.

Chapter 4

Novel Magnetoresistive Structures Using Self Assembly and Nanowires on Si

4.1. INTRODUCTION

Anodic Aluminum Oxide (AAO) is a promising template material for fabricating nanowires because of its self-assembled nanopores whose dimensions can be precisely controlled by tuning the different anodization parameters [65]. As well as having free standing AAO templates, the AAO can be integrated onto Si substrate [29,66-68] to open the road of making devices such as MRAM and catalysts that benefit from the combination of silicon processing and the self-assembly properties of AAO.

AAO templates can be made using two-step anodization which results in highly ordered and straight nanopores [25]. A major concern for integrated nanowires is the removal of the barrier layer, which is a thin aluminum oxide layer existing at the bottom of the pores. This must be removed or thinned before efficient electrochemical deposition of nanowires can occur. Several methods have been used to remove this barrier. One

method involves pore widening by phosphoric or chromic acid which will result in removal of the barrier layer as well as widening the pores [69]. This method is disadvantageous in the sense that pore size is not preserved and in the worst case, the entire template is etched away. Another method uses Ar ion-milling to break the barrier layer [30]. This method has two disadvantages. It requires an ultra-thin AAO template so that Ar ions can reach the bottom of the pores with sufficient energy to break the barrier layer. It also damages the surface of the AAO as it etches the barrier, so the AAO thickness in this method is not preserved. A third method is to perform the second anodization for a very long time. A spike in the time-dependent current curve during this step is used as a sign to stop the anodization process exactly when the barrier is removed, but the template remains secure on the contact below[30, 70].

Metallic nanowires can be grown in these templates by DC and AC electrodeposition [70-73]. Co/Cu multilayered nanowires have also been electrodeposited in free standing AAO templates using a mixture electrolyte that contains both Co and Cu cations [13,14,17,18,45-47]. These electrochemically deposited multilayered nanowires have shown current-perpendicular-to-plane giant magnetoresistance (GMR) [13,14,17] as well as a spin transfer torque phenomenon (STT) [13,14,17,74,75] as will be discussed in the following two chapters.

In this work, anodic aluminum oxide (AAO) was grown as free standing templates and also as successfully integrated templates on Si. The three barrier removal methods described above were tested here. Only the third method worked in the complete removal of the barrier layer which was further investigated by electrodepositing Cu into pores

after attempting barrier removal. Therefore, this method was used in all the subsequent work presented in this paper. Co/Cu multilayered nanowires were successfully grown and their magnetic properties such as MH loops and giant magnetoresistance (GMR) were measured. Spin transfer torque switching was also measured in the nanowires that were grown in free standing AAO templates.

4.2. EXPERIMENTAL

4.2.1. FREE STANDING AAO TEMPLATES

Two-step anodization [25] was used to make AAO templates from electropolished foils of Al metal. After anodization, the remaining Al metal was etched away with mercuric chloride, leaving oxide templates that contained nanopores with diameters of 10 to 70 nm (using sulphuric acid, H_2SO_4), and diameters of 40 to 150 nm (using oxalic acid, $H_2C_2O_4$). The barrier layers were etched by floating the templates on a mixture of phosphoric and chromic acids, and Cu films were sputtered onto the back of the templates.

4.2.2. AAO ON Si

A 1µm aluminum film was evaporated using e-beam evaporation on a silicon substrate coated with titanium and copper films (200nm each). A two-step anodization process at 18C in 0.4M oxalic was then used to make a 600-700nm anodic aluminum oxide (AAO). The anodization voltage was kept constant at 40V during the two

anodization steps. After the first anodization which was run for 4 minutes, the resulting AAO was etched away using a mixture of 1.8wt% chromic acid and 6wt% phosphoric acid for 30-45 minutes at 60C. The resulting aluminum, which was about 600nm thick, was then anodized a second time using the same parameters to create a 600-700nm thick AAO with pore diameter of 40nm and inter-pore spacing of about 100nm. In addition to growing these latter pores directly onto Si, they were also grown onto Co(20nm)/Cu(10nm)/Co(10nm) thin films that were evaporated onto Si.

The barrier layer was removed by running the second anodization step for a much longer time. For the case of Si/Ti/Al samples, which were used initially, this method failed in the removal of the barrier. However, for the case of Si/Ti/Cu/Al samples, this method succeeded in removing this barrier.

4.2.3. MAGNETORESISTIVE NANOWIRES

DC electrochemical deposition was carried out at room temperature to grow Co/Cu multilayered nanowires in the AAO membranes. The electrolyte solution was made of 155 g/L $CoSO_4$.7H2O, 1.13 g/L CuSO4 and 50g/L H_3BO_3. Cyclic voltammetry was used to determine the cathode potential for Cu and Co deposition (-0.52 and -1 volts respectively) [47]. The purpose of H_3BO_3 was to maintain the pH value of the solution at 3.7.

Multilayered Co/Cu nanowires were fabricated with different layer thicknesses by controlling the deposition time of each layer. For the Si-integrated nanowires, 50 bi-layers of Co(7.5nm)/Cu(5nm) were grown with a thick Cu layer (about 50nm) deposited

prior to and after the deposition of the multilayers. Field emission scanning electron microscopy (FESEM) was used to study the structure of the AAO and nanowires. Magnetic properties of the samples were verified by a vibrating sample magnetometer (VSM). Magnetoresistance was measured using an ac and dc magnetotransport systems with biasing currents of 1mA. STT switching was measured in multilayered nanowires grown in the free standing AAO membranes.

4.3. RESULTS AND DISCUSSION

4.3.1. FREE STANDING AAO TEMPLATES

As the AAO was formed, using a two-step anodization process, columnar nanopores self-assembled inside the oxide to form a close-packed array. The pore diameters were varied from 10-150nm by changing the anodization conditions [27,28,65]. As the diameter of the AAO nanopores decreased, the distance between the nanopores also decreased. The free-standing membranes had pores with lengths of 17μm. Figure 4.1 shows top view SEM images of free standing AAO templates before and after pore widening. Here, the pore diameter was ~40nm before widening and became ~55nm after 40 minutes of pore widening in 5wt% phosphoric acid. Note here that the pores became more circular and more ordered after widening.

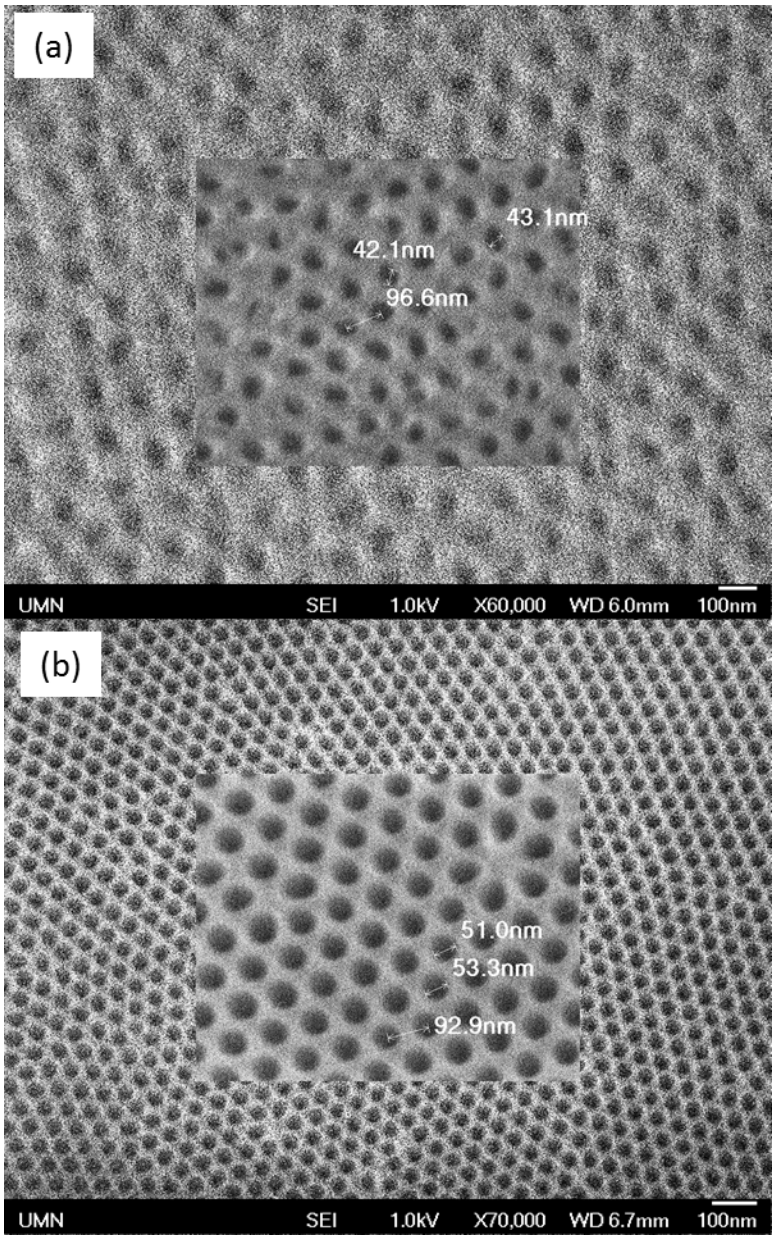

Fig. 4.1. Top view micrographs of homemade AAO templates before and after 40mins of widening in phosphoric acid.

4.3.2. AAO ON Si

It was possible to vary nanopore diameters without changing spacing. This can be

a great way to analyze the effect of interwire magnetic interactions on the magnetoresistive (MR) properties, which will be done in the future. The initial MR characterization is reported in this chapter and will be further discussed in following chapters. Figure 4.2 shows SEM images of self-assembled nanopores grown on Si with different pore sizes and fixed spacing.

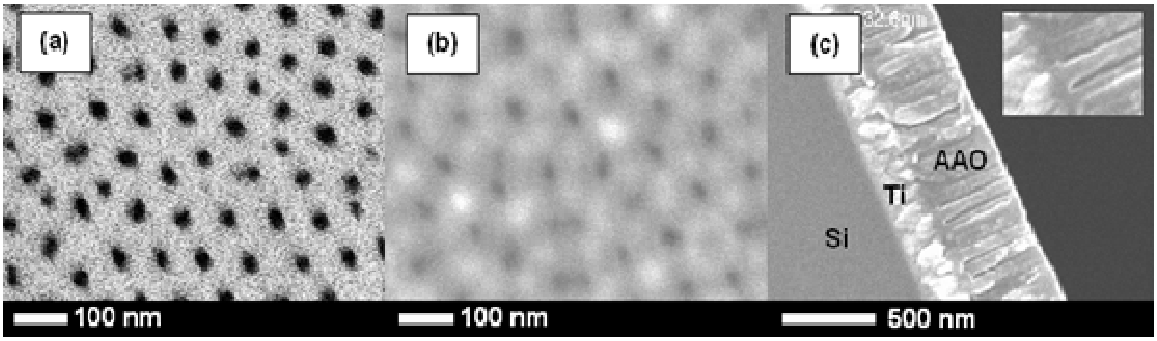

Fig. 4.2. SEM images of self-assembled nanopores grown on Si (a) top view with pore size of 40nm and 100nm spacing (0.4M oxalic acid at room temperature), (b) top view with pore size of 30nm and 100nm spacing (0.3M oxalic acid at 5^{o}C), and (c) cross-sectional view of AAO on Si/Ti showing the barrier layer at the bottom of the pores.*

Figure 4.3 shows the time dependence of the current during the long second anodization step. Fig. 4.3a represents the second anodization of Al on Si/Ti substrate where the second anodization did not result in any spikes in the current, and this means the barrier was not broken. Fig. 4.3b represents the case of having Al on Si/Ti/Cu substrate where the current increased very rapidly at about 270s, and then came back to its low value at about 350s. The flat part on the top is from the instrument current limit which is 105mA. During this spike, the Cu film tended to be very reactive to the acid, and it was completely gone after this spike. Thereafter, the sample behaved much like the

Si/Ti/Al sample. We thus used this spike as a sign to manually stop the anodization process as shown in Fig. 4.3c. Manually stopping the anodization process at this point of the curve was proven to be an ideal method to completely etch the barrier layer while maintaining good contact with the underlying Cu. However, if this anodization step was not given the sufficient time for the rapid increase in current to appear, as shown in Fig. 4.3d, then the barrier layer remained at the bottom of the pores and subsequent electrodeposition of nanowires was not possible.

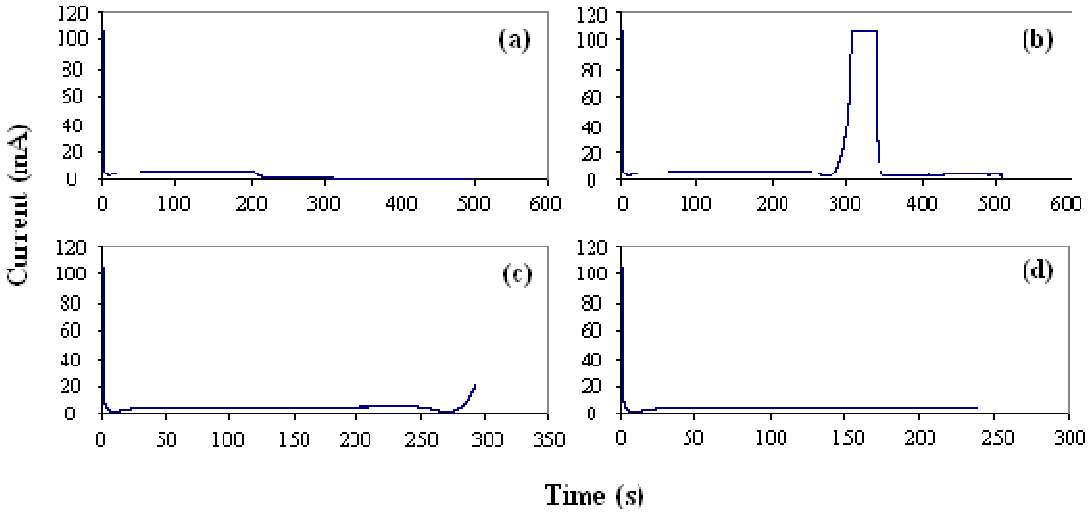

Fig. 4.3. Time dependence of the current during the (a) 2nd anodization of Al on Si/Ti substrate for 500s, (b) 2nd anodization of Al on Si/Ti/Cu substrate for 500s, (c) manually stopped 2nd anodization of Al on Si/Ti/Cu substrate at the early stages of the spike, and (d) manually stopped 2nd anodization of Al on Si/Ti/Cu substrate before the spike.*

Attempts at electrochemical deposition inside the pores was used as evidence of the presence or the absence of a barrier layer in each sample. Figure 4.4 shows the behavior of the current while attempting electrodeposition of Cu in pores of samples that had been

treated using the three methods described above. As seen in Fig. 4.4, only the third method resulted in a large, uniform current during deposition that can only be obtained when a good contact has been made between the electrolyte and the metal electrode below the pores. The remaining barrier layer in samples processed by the first two methods essentially acts as an insulator that prevents the electrolyte from accessing the electrode.

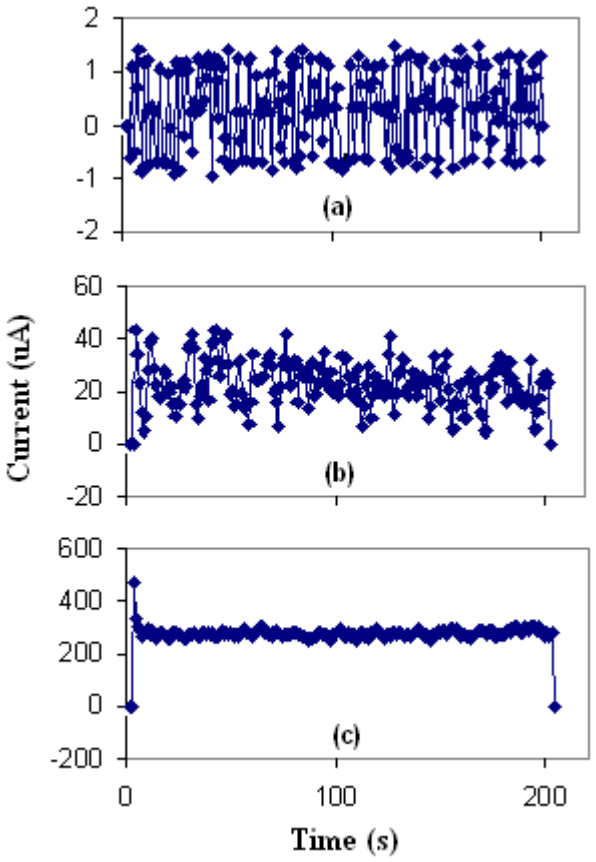

Fig. 4.4. Time dependence of the current during DC electrodeposition of Cu in pores whose barrier layers were treated using (a) Ar ion milling for 15mins, (b) pore widening in 5wt% H3PO4 for 45mins, and (c) very long second anodization.*

4.3.3. MAGNETORESISTIVE NANOWIRES

Using the free standing AAO templates, the highest magnetoresistance was found in nanowires that had hysteresis loops that were identical as measured in plane and perpendicular to the plane. The highest measured MR ($\Delta R/R$ = 11%) of the multilayers was calculated as 33% by subtracting the resistance of the Cu leads on either side of the multilayers from the denominator [14]. Figure 4.5a shows MH loops of 50 bilayers of Co(7.5nm)/Cu(5nm), in which the sample appears to have an easy axis perpendicular to the nanowires.

Compared to the relatively high MR value obtained from nanowires grown in free standing templates, nanowires on Si were found to have a lower value which was measured to be 2-3%, Fig. 4.5b-c. This may be due to larger lead resistance due to bad contacts, which is difficult to measure with these integrated samples, but improved contact methods in the following chapters mitigated this problem. The MR curve had a broader peak for the case where the field was applied parallel to the wires because the demagnetization fields due to the shape anisotropy of the Co layers inhibited switching until higher applied fields.

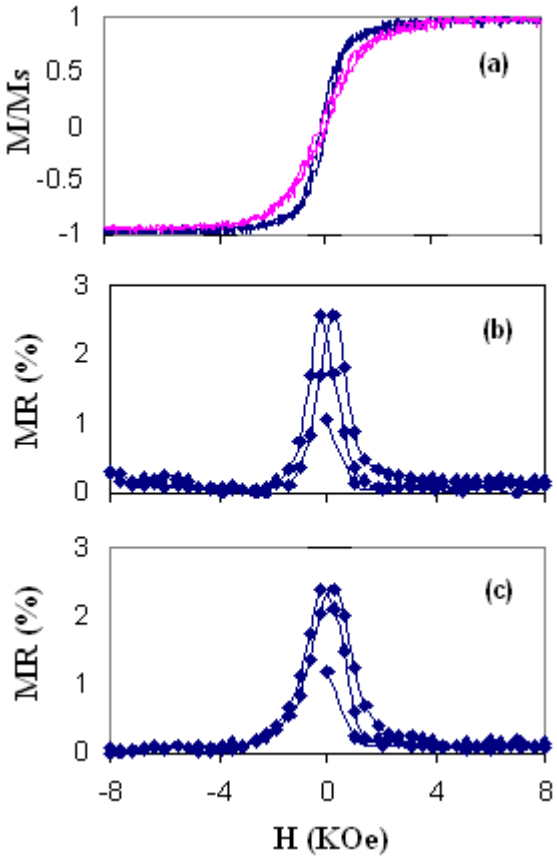

Fig. 4.5. MH loops of Co(7.5nm)/Cu(5nm) multilayered (50 bi-layers) nanowires with the field perpendicular (blue) and parallel (pink) to the wires (a), and magnetoresistance when the field is perpendicular (b) and parallel (c) to the wires.*

4.4. CONCLUSIONS

Anodic aluminum oxide (AAO) was fabricated as free standing membranes and as successfully integrated templates on Si with pore sizes that were varied between 10-1500 nm by adjusting the anodization parameters. Into these templates, Co/Cu nanowires were successfully fabricated by DC electrodeposition with an easy axis perpendicular to the

wires length. These mutlilayers showed a current-perpendicular-to-plane giant magnetoresistance (CPP-GMR) as well as spin transfer torque (STT) switching. Co/Cu multilayers grown on Si had a GMR ratio of 2-3% which is lower than that of the same multilayers grown in free standing templates. This might be due to the lead resistance in this integrated structure which was improved in the study below. With diameters in the 10-150 nm range and integration with Si, these nanostructures have great potential for future nanosensors, MRAM and microwave oscillator arrays.

Chapter 5

Low-Resistivity 10nm Diameter Magnetic Sensors

5.1. INTRODUCTION

As device dimensions are reduced [76,77] below the scale of electron mean free paths (λ_e), electrical resistivities at the nanoscale have increasing scientific interest and technological importance. This is especially true for magnetic read sensors with dimensions less than 40nm ($\sim\lambda_{metals}$). Models of resistivity often predict difficulty for device designers planning to use 10-40nm dimensions due to potential surface and grain boundary scattering.[78-81] Experimental measurements of electron transport in metallic nanostructures have also been extensive, but challenging, due to contact design, corroded surfaces, grain boundary resistances, and scattering losses, especially for nanowires with exposed edges.[82-86] For copper alone, reported resistivities have varied by several orders of magnitude depending on fabrication and measurement techniques.[86-89] Here, resistivities of 10nm-diameter metallic wires were measured in densely-packed, vertical

arrays inside anodic alumina templates using an atomic force microscope (AFM) tip as a top contact. These arrays are excellent candidates for devices such as array read sensors [17,90], highly-dense magnetic random-access memory [17], and self-assembled electronics.[91] Therefore, the results reported here not only promise to improve near-term read sensors, but also to point the way to low resistance interconnects which will quench growing concerns that the 'size-effect' is threatening to halt progress along the International Technology Roadmap for Semiconductors (ITRS).[92]

Other high-density arrays have been proposed for hard drive media where increasing recording density requirements [93,94] have motivated the fabrication of magnetic nanoscale assemblies with long range order using advanced nanotechnologies, including self-assembly, [95-105] e-beam lithography,[106-107] and block copolymers.[108-114] In fact, guided self-assembly is considered to be the leading candidate for bit patterned magnetic recording. The new technologies expected to be introduced at 1-1.5 TBit/inch^2, such as Heat Assisted Magnetic Recording (HAMR) and Bit Patterned Magnetic Recording (BPMR), will have reduced media Bit Aspect Ratios (BAR) with track pitches of about 30 nm, suggesting a need for < 20 nm diameter read sensors.[115,116] In all cases, the critical dimensions will be reduced quickly as recording densities increase. Consequently, there is an immediate need for suitably scaled read sensors. Similar to the semiconducting nanowires that are revolutionizing nanoelectronics,[117-121] the 10nm diameter magnetic metal nanowires introduced here offer a potential path for sustaining the rapid evolution of magnetic recording.

Current read sensors primarily use tunneling magnetoresistive (TMR) sensors,

which are composed of an oxide layer (such as MgO) sandwiched between two ferromagnetic metal layers. These heads are excellent for today's dimensions (bits ~ 15 nm x 75 nm) with magnetoresistances ($MR=\Delta R_{magnet}/R$) of about 70%. However, the demands of device integration prefer resistances (R) below 300Ω, which means that the resistance-area (RA) products must be substantially decreased as the element areas decrease with recording density. Today, the minimum RA products of TMR sensors ($\sim 1\Omega.\mu m^2$) are acceptable, but progressively smaller values will be required for future read sensors to have feasible signal-to-noise ratios (SNR). [122] In addition, excess resistance means that TMR resistance-capacitance (RC) time constants will be too large for high-speed performance at small element sizes. Finally, large resistances produce Johnson noise and heat which is difficult to dissipate. This has led researchers to examine all-metal "current perpendicular to the plane giant magnetoresistive" (CPP GMR) structures, [8-10,123-126] which are calculated to have high signal to noise ratios [124] at the recording densities of the nano-enabled media (1-10 Tb/in^2) mentioned above.

Experimentally, however, vacuum-deposited CPP GMR structures have low magnetoresistances as volume/sidewall ratios decrease because device etching destroys the interfaces between the ferromagnet/nonmagnet/ferromagnet layers at the sidewalls. Pioneering attempts to increase the magnetoresistance of CPP GMR structures have included the use of nano-oxide layers (NOL) and Heusler-alloy magnetic soft layers.[8, 123] In NOL devices, co-deposition of Al or Si within the device layers is followed by a controlled oxidation to produce insulating Al-O or Si-O boundaries between the magnetic grains.[7,8] Large variations in grain morphology typically lead to unpredictable device

performance even at large sensor dimensions. In Heusler-alloy devices, thick seed layers are required.[9,10] In all of these cases, vacuum-deposited thin films were patterned into either ellipsoidal or cylindrical pillars, the smallest of which were 30nm-diameter cylinders. Also, in all cases, the magneotresistance decreased with diameter until it is negligible below 30nm.

Here, nanoporous aluminum oxide templates with 7 to 20nm diameter pores were made using electrochemical anodization of Al. CPP GMR structures were then designed and electrochemically deposited into these pore arrays. Magnetotransport measurements found that these structures met or surpassed what has been demonstrated in read structures using conventional vacuum deposition and lithography. These parameter improvements are significant because our structures are up to 10x smaller in area compared to current state-of-the-art laboratory read sensors that have 30nm diameters ($707nm^2$).[124] These results hold technological as well as scientific importance because electrochemical techniques are already used in construction of magnetic recording heads, including shields and write heads. Also, the deposition described here can be used to grow read sensors into not only aluminum oxide pores, but into any insulating nanohole, including those in e-beam resists and/or block copolymers. The thick permalloy films that are needed for magnetic shielding of read sensors can be used as growth electrodes because there is no need to have a seed layer with these Co/Cu layers, Figure 5.1. Therefore, facile integration of these sensors with commercial fabrication processes is possible.

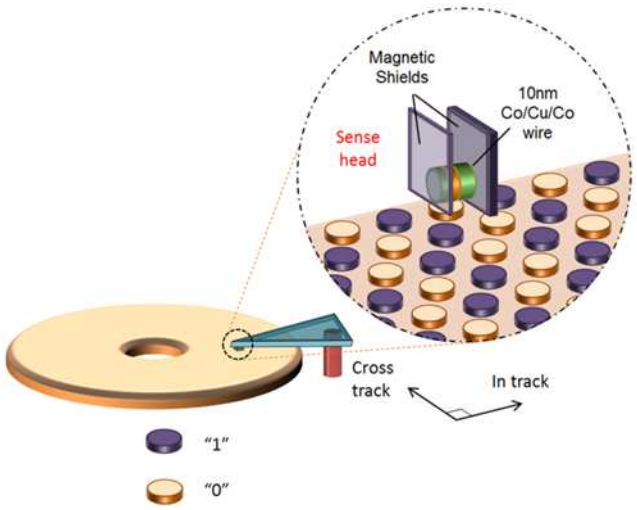

Fig. 5.1. 3D schematic of a 10-nm diameter read sensor. This 10nm-diameter trilayered Co/Cu/Co nanowire, sandwiched by two permalloy shields, is shown reading a bit patterned medium.**

5.2. EXPERIMENTAL

Nanopores were made by anodizing both Al foils and Al films on Si. First, high purity alumina foils (> 99.99%) were degreased in acetone for 10 minutes at room temperature and rinsed subsequently in methanol, isopropyl alcohol (IPA), and finally with deionized (DI) water. After drying in nitrogen, the native oxide layer was removed using a 1 M NaOH solution for 3 minutes. A DI water rinse and N_2 drying were followed by electrochemical polishing to remove surface defects of the Al foil. The electrochemical polishing solution was a 1:5 mixture of perchloric acid ($HClO_4$) and ethanol, and a constant potential of 18 V at 6^{o}C was applied. After this, the foils were anodized in sulfuric acid at various voltages, temperatures and acid concentrations to

explore the minimization of pore size. The resulting nanoporous oxide was etched using a mixture of 1.8 wt% Chromic acid (Cr_2O_3) and 6 wt% Phosphoric acid (H_3PO_4) at 60^oC for 20 minutes. The remaining Al foil was then anodized again under identical conditions for 3 hours to produce uniform nanopores inside a new oxide layer that was 17µm thick. For templates on Si, Ti (200nm)/Cu (200nm) electrodes were first evaporated onto Si, followed by evaporation of a 1 µm thick Al film which was then anodized similarly to the foils above but with different times to produce 190nm thick AAO. This Si-integrated AAO was used for all of the read sensor studies.

Next, a single electrolytic bath was used to electroplate trilayered [Co(15nm)/Cu(5nm)/Co(10nm)] structures with copper leads inside the AAO nanopores. The bath composition was 155 g/l $CoSO_4$, 1.13g/l $CuSO_4 \cdot 7H_2O$ and 50 g/l H_3BO_3 to maintain the pH at 3.7. Co and Cu layers were deposited using -1.00V and -0.52V, respectively, versus a Ag/AgCl reference electrode. The structures of the nanopores and nanowires were characterized by scanning electron microscopy (SEM JEOL6700). More information on the crystalline structure and magnetic properties of electrodeposited Co is given in ref [25].

Single wire resistances were measured using a conductive AFM tip and a fixed current of 100uA while measuring the voltage across the wires. The bottom contact was the conductive film (Ti/Cu) onto which the nanowires were electroplated. Spin torque switching was measured by sweeping the current from +100mA to -100mA and back while the voltage was recorded using a Keithley 2400 sourcemeter. A magnetic field was applied in-plane (perpendicular to the wires) by an electromagnet. Magnetoresistance was

measured using a 2.5mA current and sweeping the applied magnetic field.

5.3. RESULTS AND DISCUSSION

5.3.1. TEMPLATES

First, a process for making reproducible, very small nanoholes was developed using two-step anodization of aluminum foils and also films on metal-electrode coated Si.[25] Although anodizing voltage has been the primary parameter used to reduce pore diameters from 250 to 25nm with a well-known linear dependence [27], here we show that at lower anodization voltages, the nanopore diameter can be independent of voltage, Figure 5.2. Therefore, to achieve smaller diameters, other parameters such as electrolyte dilution and temperature were explored. We found that pore sizes decreased by 0.3nm/^{o}C, but only down to 1^{o}C (~10nm), below which the solution started to freeze. Electrolyte dilution was then optimized to get diameters smaller than 10nm, but careful monitoring of the thermal conditions was important. For repeatability, the 10nm samples in this study were grown under very similar thermal conditions to minimize variability between samples. Figure 5.2 shows scanning electron micrographs and histograms of nanopores made at different anodization voltages and electrolyte concentrations.

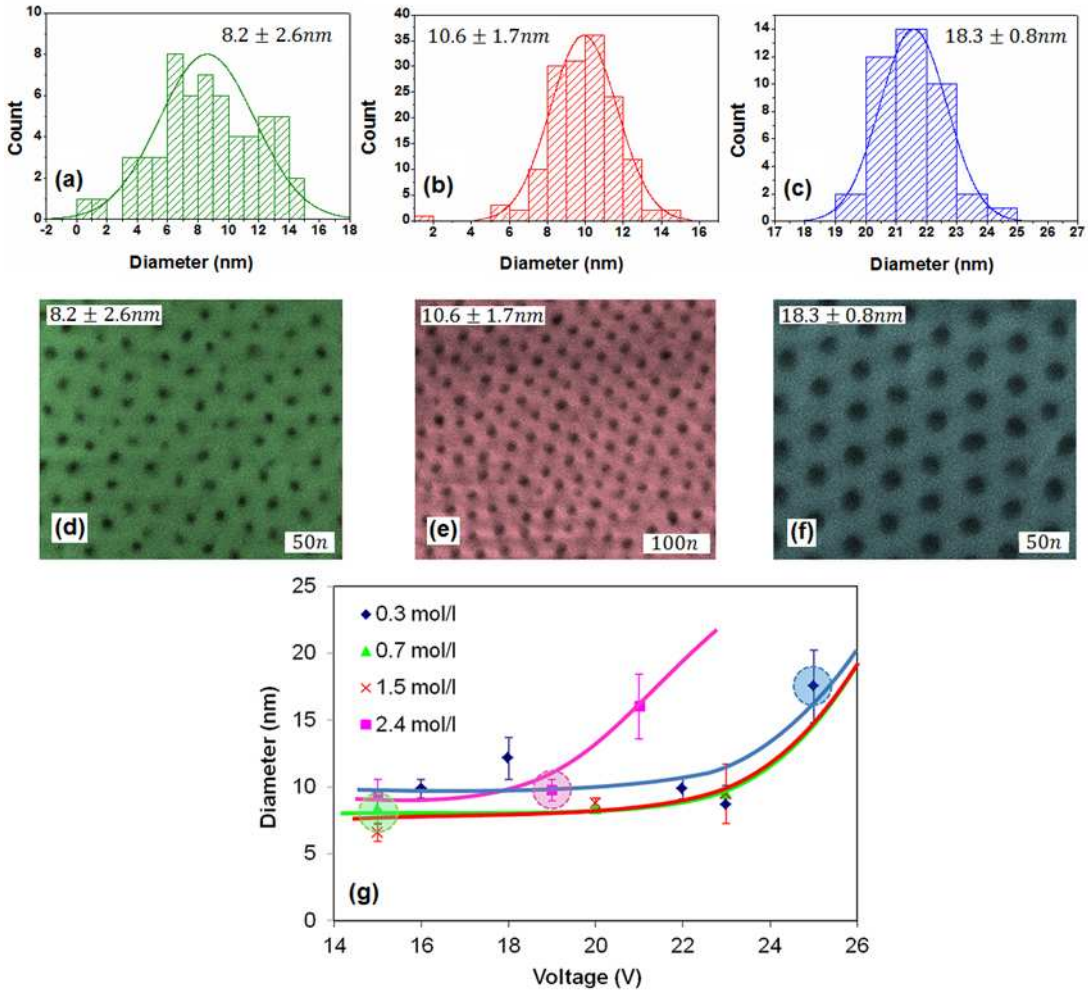

Fig. 5.2. (a-c) Diameter histograms of nanopores formed by anodization at various voltages and concentrations of H2SO4 at 1 oC, as shown in the micrographs in (d-f) and summarized in (g). A temperature study revealed an increase in diameter by 0.3nm/oC so local heating must be carefully controlled. Circled data points in (g) correspond to nanopores that were imaged using SEM as shown in the colored images. The pore size and distribution shown here are analyzed over large areas using ImageJ.**

Although these nanopores are excellent templates, the read sensors discussed below, or any CPP GMR structure, can be electroplated into a variety nanoporous

templates, including those being developed for bit patterned media (BPM). This is important for mass production of read sensors, RAM or 3D nanoelectronics, where long range order will be necessary. Long range order in alumina templates can be achieved by anodizing nanoimprinted Al,[26] Figure 5.3, demonstrated here with 74nm diameter pores. Although very expensive, imprint stamps with 5 to 20nm features have been made industrially via large scale lithography.[127] It is important to note that the expensive master stamps can be used to produce hundreds of wafers with 105-106 electrochemically-grown magnetic devices on each wafer. In addition, daughter stamps from the e-beam masters can be produced in order to again multiply the number of sensors from each master by several orders of magnitude. [127] Therefore, the cost per device will not be a barrier to implementation for industry, especially as e-beam lithography costs continue to decrease due to faster resists and writing software.

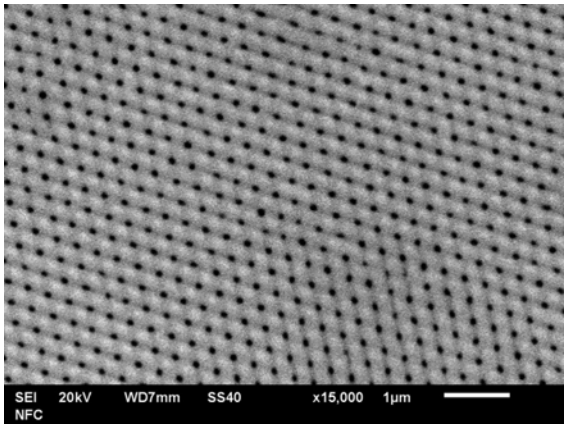

Fig. 5.3. Nanoimprinted aluminum anodized using 160V in 1% phosphoric acid at 0oC. Pores in the resulting oxide self-assembled to align with imprints (74+/-10nm diameters).**

5.3.2. LOW RESISTIVITY NANOWIRES

Next, electrochemical deposition was used to fill the alumina templates, and the resistivities of resulting 10nm-diameter, 190nm-long wires were measured using Au-coated AFM tips and 100μA. The GMR structure discussed below was 30nm long, so the Cu leads were 160nm long in this feasibility study. The top Cu was grown out of the pores, and then it was polished back so that the tops of the wires were level with the surface. Varying pressures were applied to the AFM tip as it was lowered onto the surface in order to make contact with 1-3 wires. A histogram was then constructed using 40 resistance measurements, Figure 5.4. In the first ten measurements, a cluster of 8 resistance readings occurred in the range of 100-129Ω with two single points at 155Ω and 160Ω. All possible combinations of pairs of these 10 single nanowire measurements were calculated and compared to the next cluster of readings that occurred at 50-68Ω with an average and standard deviation of 57Ω and 5.5Ω, respectively. The average and standard deviation of the 45 calculated combinations yielded 59Ω and 6.3Ω, respectively. A similar comparison for all 120 combinations of three single wires (39.2 ± 3.1Ω) was compared to the next grouping of measured resistance values (40.5 ± 3.3Ω). These simulated combinations are plotted next to the measured data to match the spread in the values in Figure 5.4. These results indicate that the first 10 measurements were those of single wires with resistances of 119.8 ± 21.6Ω. This average and distribution corresponds to 3.2 times the resistivity of bulk copper (ρ_o), or 5.4 μΩcm for the average diameter (10.6 ± 1.7nm) determined from micrographs such as Figure 2b using ImageJ. [128] The high resistance "tail" of the data shown in Figure 5.4 is expected for an inverse Gaussian

distribution that arises from resistances of nanowires with Gaussian distributions in diameters and therefore in areas (Figure 5.2b). This occurs due to the inverse relationship between resistance and area, $R = \rho\, l\, /A$ where l was 190nm for all of the wires.

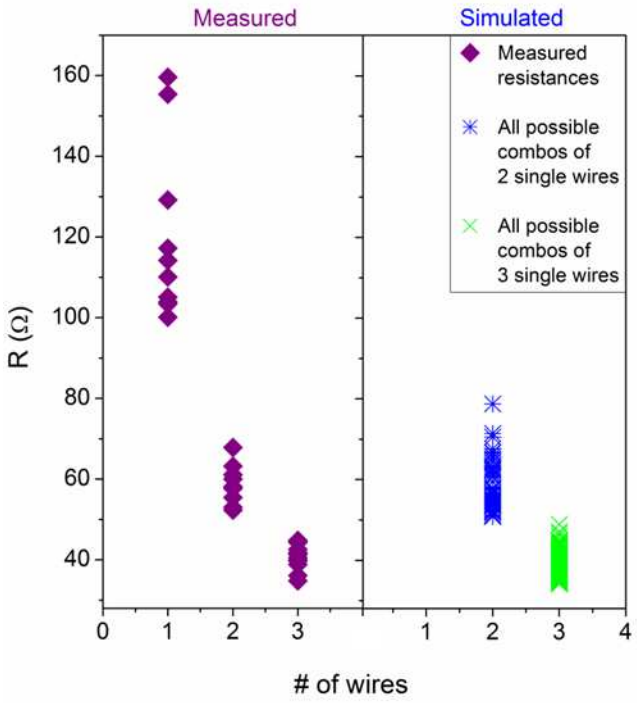

Fig. 5.4. Resistance histogram of 10nm nanowires measured (purple) while inside the AAO matrix. The measured groupings were separated by resistance gaps as 1, 2, or 3 wires were contacted. Blue points correspond to the 45 combinations (combos) of any two measurements of the individual nanowires. Green points correspond to all 120 possible combinations of any three individual nanowires.**

The ITRS "size effect" of increased resistivity (ρ) in nanowires compared to bulk (ρ_o) is usually attributed to electron scattering from surfaces. A popular approximation using the Fuchs-Sondheimer (FS) theory [129,130] for cylindrical wires is

$$\rho = \rho_o*[1 + ¾ (1-p)\kappa] \qquad (5.1)$$

where $\kappa = D/ \lambda_e$, D is the wire diameter, λ_e is the mean free path of the electrons (39nm for bulk Cu), and p is a constant (0-1) that depends on the type of electron reflection off the sample surfaces (from diffuse to specular). Using this approximation, diffuse scattering at the sidewalls of 10nm-diameter nanowires predicts resistivities of 6.4μΩcm-19% higher than our measured resistivities. In reality, most lithographically-patterned nanowires from electroplated Cu films are even more resistive than this approximation predicts: resistivities comparable to that of our nanowires are only obtained with an order of magnitude larger cross sectional area.[131] In fact, the approximation in (5.1) was shown to under-estimate the size effect compared to exact solutions of the FS theory.[132] This result has also been confirmed analytically and numerically using an atomistic tight-binding approach where the resistance (R) was calculated as a function of wire length to determine λ_e using

$$R = h/2e^2 (1/M + 1/\lambda_e M) = h/2e^2 (1/MT_{ave}) \qquad (5.2)$$

where h and e are Planck's constant and electron charge, M is the number of conducting channels whose subbands cross the Fermi level and T_{ave} is the average transmission probability (details in [80]). In this case, one atomic monolayer roughness was predicted to cause an order of magnitude higher resistivities for 10nm diameter nanowires inside alumina compared to bulk. Therefore, the present measurements indicate that the sidewalls of our nanowires must be very smooth, and the nanowires have great promise for device applications, such as the magnetic sensors discussed next.

5.3.3. NANOWIRE READ SENSORS

Co(15nm)/Cu(5nm)/Co(10nm) trilayers were grown inside Si-integrated nanoporous templates to make 10nm diameter GMR sensors, similar to the head shown in Figure 5.1. Previously, the focus of multilayers of Co/Cu with large Co thicknesses grown in free-standing AAO templates was magnetic random access memory (MRAM) which demands low switching current densities; that is the currents that were required to produce aligned or anti-aligned Co magnetizations.[14] However, hard drive read sensors require the opposite: high switching current densities to avoid destabilizing the head. Here, only one sandwich structure with thin Co layers was grown per nanowire in order to obtain higher switching current densities and thus to reduce read sensor noise while maintaining a reasonable GMR ratio.[133]

Magnetoresistance and current stability were measured via spin transfer torque (STT) curves [75], Figure 5.5. Here, the two Co layers in each wire were first set parallel by a 130 Oe magnetic field (used in read heads to overcome the dipole field from the fixed layer), and then a current through the wire was swept from +100mA to -100mA. A positive current is one for which electrons pass from the fixed layer to the free layer. As the absolute value of the current increased, the resistance showed the well-known parabolic Joule heating until a critical current was reached when the free Co layer was switched by the spin torque of the current such that it became anti-aligned to the fixed Co layer. At this point, the resistance exhibited a steep increase due to scattering of electrons from the anti-aligned magnetic layers. On sweeping back to positive currents, the Co layers switched back to be aligned parallel to each other again. From the areas (Figure

5.2b) and resistances (Figure 5.4), the switching current densities were determined to be ($J_{P\text{-}AP}$ = -6.73x10^9 A/cm^2 and $J_{AP\text{-}P}$= +5.66x10^9 A/cm^2). The switching current densities were higher and less symmetric, as expected, when a bias of 250 Oe was used ($J_{P\text{-}AP}$ = -6.53x10^9 A/cm^2 and $J_{AP\text{-}P}$ = +7.32x10^9 A/cm^2), Figure 5.5b. These results indicated that spin torque noise in these read sensors will be minimal because operating read sensor current densities are substantially below these values.[133]

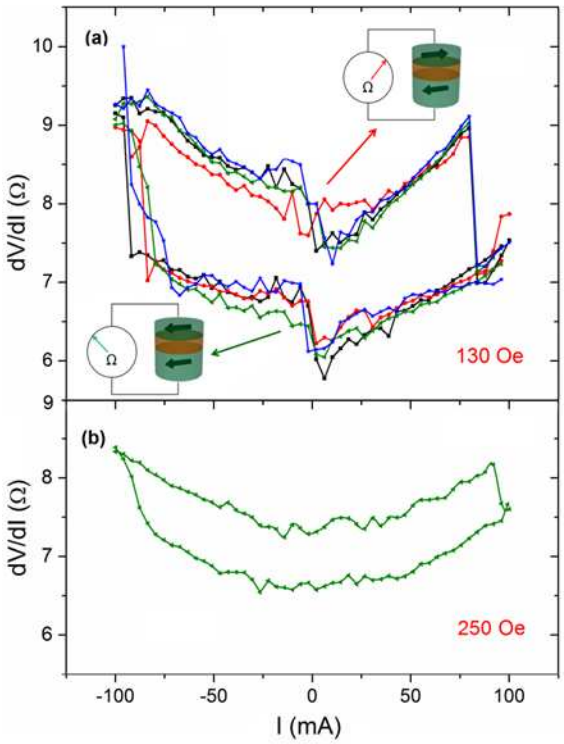

Fig. 5.5. Resistance of trilayered Co(15 nm)/Cu(5 nm)/Co(10 nm) nanowires as a function of current as the current through was swept from positive to negative (lower curves) and negative to positive (upper curves) in an applied field of (a) 130Oe and (b) 250Oe. . Note that code similar to [139] calculated demag and dipole fields in the range of 100-200 Oe acting on the free layer.**

The window between the aligned and anti-aligned states exhibited a magnetoresistance of 19%, a value that was comparable to those obtained in our typical magnetoresistance measurements, Figure 5.6. Here, the magnetizations of a sensor is aligned using a 6kOe field, then the resistance is measured as the field is swept to -6kOe and back. At -500Oe, the switching of the soft Co layer increases the resistance due to the GMR effect, and then at -2.5kOe, the switching of the hard Co layer decreases the resistance back to the aligned value. Returning to +6kOe, the resistance jumps are observed again due to the soft then the hard Co layers switching back. Other groups have also reported 10-20%MR for electrodeposited multilayered Co/Cu structures although with larger (30-100nm) diameters.[134-136] The total RA product of our samples was 0.04 $\Omega.\mu m^2$ with $\Delta RA = 0.008\Omega.\mu m^2$ including the area of the oxide matrix and the copper leads. The resistance and RA product of a single trilayer (without the nanowire leads [137] or matrix) can then be calculated as 20-30Ω and $0.002\Omega.\mu m^2$, respectively, with ΔR= 4-5Ω which are nearly ideal values.

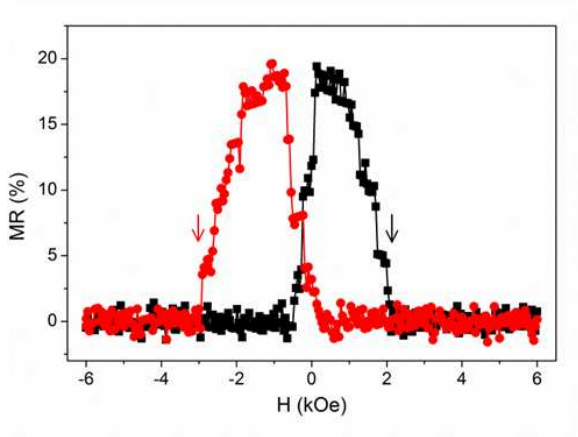

Fig. 3. Magnetoresistance of 10nm-diameter Co(15nm)/Cu(5nm)/Co(10nm) trilayered nanowires.**

Currently, commercial read sensors are individually patterned from their thin film precursors by ion milling, and then they are insulated with an aluminum oxide coating that has to be chemomechanically planarized. Therefore, unlike MRAM applications, the need to contact a single nanowire within an array is not required in read heads. Rather, it is a great advantage for these electrodeposited structures that they are inside a suitable insulator as-grown. Therefore, using commercial fabrication techniques, a 30nm diameter etch will produce a 10nm diameter device that is already surrounded by 10 nm of aluminum oxide on all sides.

Even though these elements are 10x smaller in area, the properties shown above are comparable to state of the art CPP GMR structures grown by vacuum deposition and lithographic methods [123] where 30nm diameter structures have been fabricated with RA products of $0.043\Omega.\mu m^2$ and 5.5% MR. Recall that smaller diameter structures have proven exceedingly difficult via lithography. The attractive results presented here are a result of the layers being grown in-situ: thus, the sidewalls never experience damaging etching conditions. Experimentally, studies have shown that sidewall rms roughness, due to plasma etching for instance, can be as large as 4nm. [138] As mentioned above, theory shows that roughnesses with standard deviations of even 1 atomic monolayer strongly affect electron scattering, and therefore resistance and magnetoresistance. [80]

For proper bit differentiation, the magnetic soft layer should be biased perpendicular to the fixed layer in the actual device. This can be achieved by the same methods currently used in read sensors, that is by use of either permanent magnets, where

materials such as permalloy are deposited beside the sensor.[133] Thus, the fabrication processes described here could substitute directly into the head fabrication process with simple template-growth/electrochemistry steps replacing thin-film growth/lithography/oxide/planarization steps that are used currently after the first shield is electroplated.

5.4. CONCLUSIONS

We have measured low resistivities (5.4 μΩcm) in 10nm-diameter electroplated nanowires and have used these nanowires to demonstrate initial feasibility of a new class of read sensor for ultra-high density recording. The read sensors were sandwiches of Co/Cu/Co that were 10 times smaller in area than the next smallest reported read head. Resistance-area (RA) products of 2 $m\Omega\mu m^2$ offer a highly desirable 20-30 Ω resistance even for 10nm diameter rods. We have also demonstrated 19% magnetoresistance (MR) and high spin torque stability (low current-induced noise) with switching current densities higher than 10^9 A/cm^2. We attribute much of our advantages at these very small dimensions to in situ growth with no need for sidewall etching. Overall, the low-resistivity nanowires presented here provide an unusual opportunity to enable continued high density growth for many nanosystems, including recording, RAM and 3D nanoelectronics.

Chapter 6

Effect of the Interlayer Spacer Thickness on the Spin Transfer Torque Effects in Magnetic Multilayered Nanowires

6.1. INTRODUCTION

Current induced magnetization reversal in magnetic multilayers has been widely investigated and proven both theoretically and experimentally [49-52,139-146]. These structures, in the most popular scenario, are composed of two ferromagnetic layers sandwiching a nonmagnetic layer, which can be an insulator as in the case of magnetic tunnel junctions (MTJ) [140-142], or a metallic nonmagnetic layer as in the case of giant magnetoresistive (GMR) devices [14,143-144]. In either of these architectures, the switching from antiparallel magnetizations (high resistance state) to parallel magnetizations (low resistance state) and back again has been well understood and mathematically formulated. Albert et al. [144] showed that the switching current densities of all metallic Co/Cu/Co trilayered structures vary linearly with the free layer thickness

and exponentially with the nonmagnetic layer thickness while having no dependence on the fixed layer thickness. In another study [145], the effect of the applied magnetic field on similar structures was studied. It was shown that the switching current densities for magnetic layers having in plane or perpendicular to the plane anisotropies vary linearly with the applied magnetic field, with lower switching current densities in the perpendicular case owing to the collinear demagnetizing and anisotropy fields. These observations, along with the mathematical formulae available for those devices [168,170], allow for the design and optimization of the behavior of these structures. Multilayered structures, on the other hand, have had very limited exploration. Although theoretical predictions [139] and experimental measurements [14] exist for these types of structures, understanding of the switching behavior and control over the current densities have yet to be fully realized.

GMR multilayered structures have been intensively studied over the past decades. This is mainly due to their high MR ratios which come from the direct correlation between MR and the number of the layers as suggested by the interface spin-dependent scattering model [146]. Although higher MR ratios can be seen in magnetic tunnel junctions, these structures have very large total resistances that can potentially lead to slow device speed performance due to their high resistance-capacitance (RC) time constants. These junctions are good for current hard disk drive read sensor applications where small stack thicknesses are desired for high density recording but however, MRAM applications may favor the all metallic GMR multilayered structures because of their low resistances and the potentially achievable high MR ratios.

In this work, spin transfer torque switching was observed in multilayered Co/Cu nanowires under zero external magnetic fields. Similar to Ref. 169, we found that the switching current densities increase with the Cu interlayer thickness due to spin relaxation while still being in the 10^6-10^7 A/cm^2 range. More interestingly however, we found that the majority of the observed increase is coming from the effective demagnetizing field (H_{eff}) effect. In studying the effect of this field on the switching current densities, we observed that unlike conventional spin valve structures, multilayered structures can be engineered to have very small H_{eff} and thus small switching current densities, all in the absence of external fields. This simplifies device complexity when structures like these are implemented in MRAM applications, for instance. We also observed that the magnetization easy axis of these multilayers changes from perpendicular to the plane to in the plane of the Co layers as the interlayer Cu thickness is changed, resulting in different spin transfer effects. Interestingly however, the high resistance state (HRS) was shown to revert always to an in-plane AP configuration irrespective of the direction of the magnetic anisotropy. Finally, we tried to relate the experimental observations to simple energy and dipole field calculations, and we found agreeing results.

6.2. EXPERIMENTAL

Arrays of Co/Cu multilayered nanowires were electrodeposited into anodic aluminum oxide templates that contained columnar nanopores with diameters of 100nm

and porosity of 22% from a mixture solution that contained 155g/L $CoSO_4.7H_2O$ and 1.13g/L $CuSO_4$. The number of Co/Cu bilayers was fixed at 200, and the thickness of the individual Co layers was fixed at 10nm. The c-axis of the Co layers was made perpendicular to the plane of the layers by adjusting the pH of the solution to 5.8 using diluted NaOH. The thickness of the Cu spacer layers is the only variable in this study and was varied from 3nm to 20nm. A long Cu lead was deposited prior to and after the deposition of the multilayers and polishing was performed after nanowire outgrowth was observed. The samples were then transferred to the vibrating sample magnetometer (VSM) to measure their static magnetic properties. Room temperature magnetotransport measurements in the absence of external magnetic fields were then performed, Figure 6.1. Here, a 10μm diameter contact was applied to the tips of the wires and the current was swept from -10mA to 10mA and back while the voltage across the wires was recorded. The resistance *dV/dI* was then calculated.

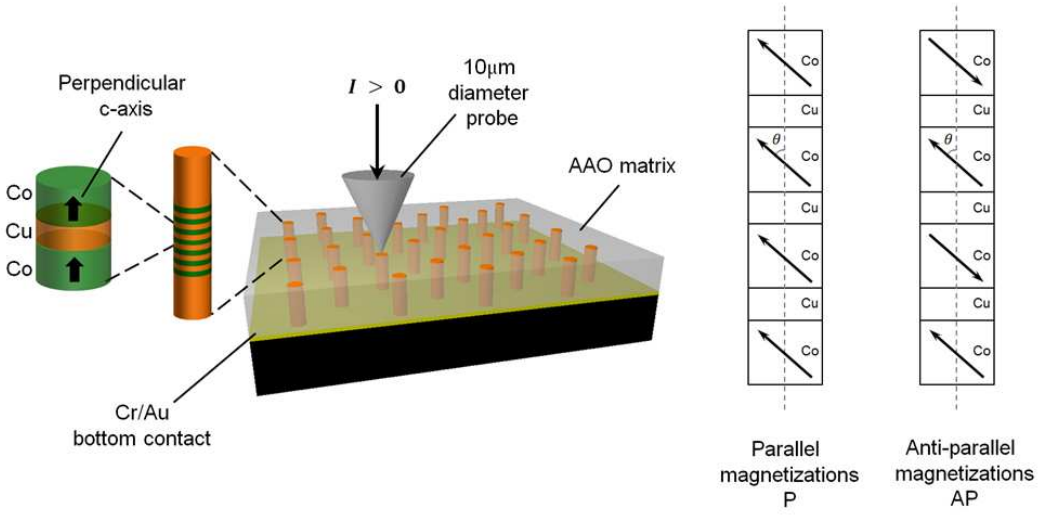

Fig. 6.1. Schematics of the spin torque switching measurements and schematics of titled magnetization configuration.

6.3. RESULTS AND DISCUSSION

6.3.1. MAGNETIZATION HYSTERESIS LOOPS

Figure 6.2 shows x-ray diffraction pattern for Co wires made using the above mixture at pH=5.8. As seen here, the Co layers have a main (002) peak indicating a perpendicular c-axis. Our Co/Cu multilayered wires studies here were grown from the same electrolyte and thus their Co layers have perpendicular c-axis too.

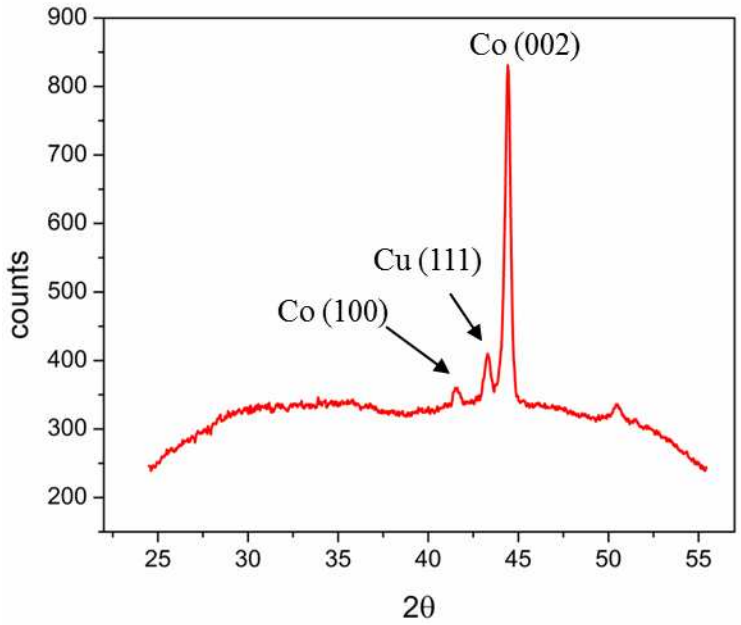

Fig. 6.2. X-ray diffraction pattern for Co wires deposited at pH=5.8.

Figure 6.3 shows magnetization hysteresis (MH) loops of 100nm diameter $[Co(10n)/Cu(t_{Cu})]_{200}$ multilayered nanowire samples for different values of t_{Cu}. Here, similar to our previous study [147], we show that the multilayered structure changes its

magnetization easy axis from perpendicular-to-plane to in-plane of the Co layers as d is increased even though the c-axis is perpendicular to the plane. At small t_{Cu} (Fig. 6.3a), the high magnetostatic interactions between the Co layers and the orientation of the c-axis both favor a magnetization easy axis along the NW axis (perpendicular to the plane of the Co layers) even though the shape anisotropy of the thin Co layers favors an in-plane magnetization. Figure 6.3b (intermediate t_{Cu}) shows an intermediate sample where the magnetostatic interactions and the crystallographic anisotropy balance the shape anisotropy of the layers, resulting in a nearly isotropic behavior. Finally, when t_{Cu} is large (Fig. 6.3c), the magnetostatic interactions become very weak and the high shape anisotropy dominates the crystalline anisotropy, resulting in a magnetization easy axis perpendicular to the NW axis (in plane of the Co layers). To save space, we show MH loops for only three thicknesses here but the overall behavior of all the samples can be seen in Fig. 6.3d. In Fig. 6.3d, magnetic susceptibility calculated from *dM/dH* near the origin is plotted vs t_{Cu} when the field is applied perpendicular and parallel to the NW axis. This clearly shows the transition from perpendicular-to-the-plane anisotropy to in-plane anisotropy with an isotropic point at the intersection of the two curves seen at t_{Cu}=10nm.

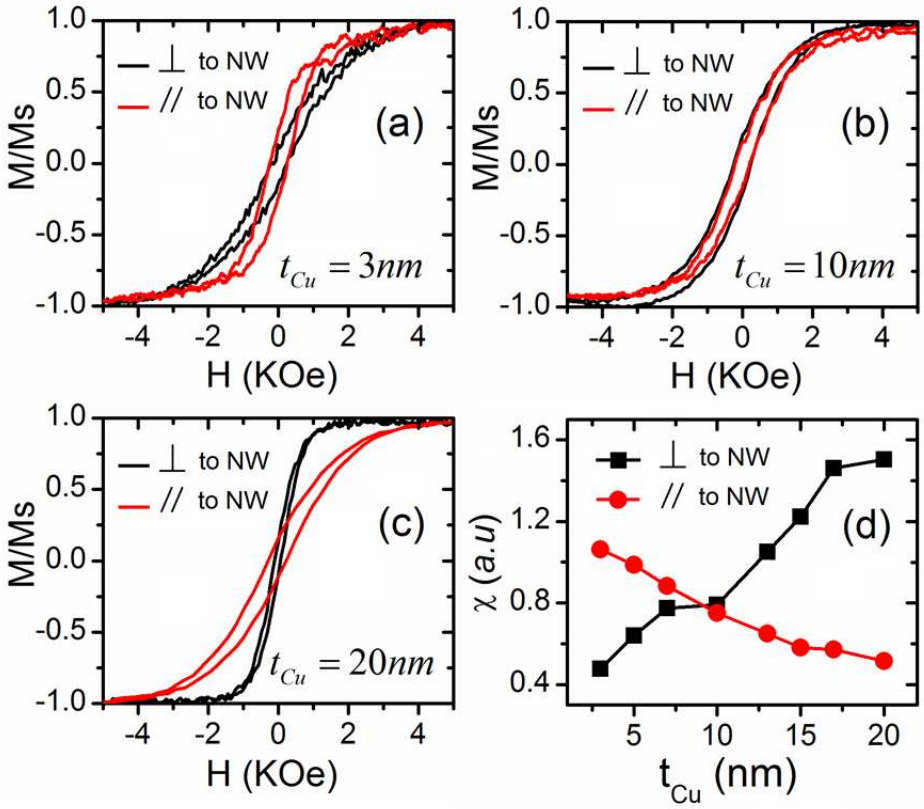

Fig. 6.3. Magnetization hysteresis loops of 100nm diameter [Co(10nm)/Cu(tCu)]200 wires with in-plane (perpendicular to wire) c-axis when is (a) 3nm, (b) 10nm, and (c) 20nm. (d) Magnetic susceptibility, calculated from dM/dH near the origin of the MH loops, is plotted vs t_{Cu}.

6.3.2. SPIN TRANSFER TORQUE SWITCHING

Figure 6.4 shows zero field STT switching loops of our multilayers for each value of t_{Cu}. The difference in resistance between the samples is due to contacting different number of wires in parallel for each measurement. This resulted in different values of the current needed to switch the layers from parallel P magnetizations (low resistance state:

LRS) to antiparallel AP magnetizations (high resistance state: HRS) and back. The number of contacted wires was determined using the area of the probe and previous single wire resistance measurements [18]. The samples were measured multiple times for repeatability but only one loop per sample is shown here. The as measured magnetoresistance (MR) ratio extracted from these figures is 1.52±0.80% which can be as high as 19.14±14.62% after subtracting lead resistances. The number of layers that switch also varies with layer thickness, so the total MR value varies accordingly. The number of layers per domain is currently under study via neutron scattering, but the trend in the switching current densities will be explained in this work.

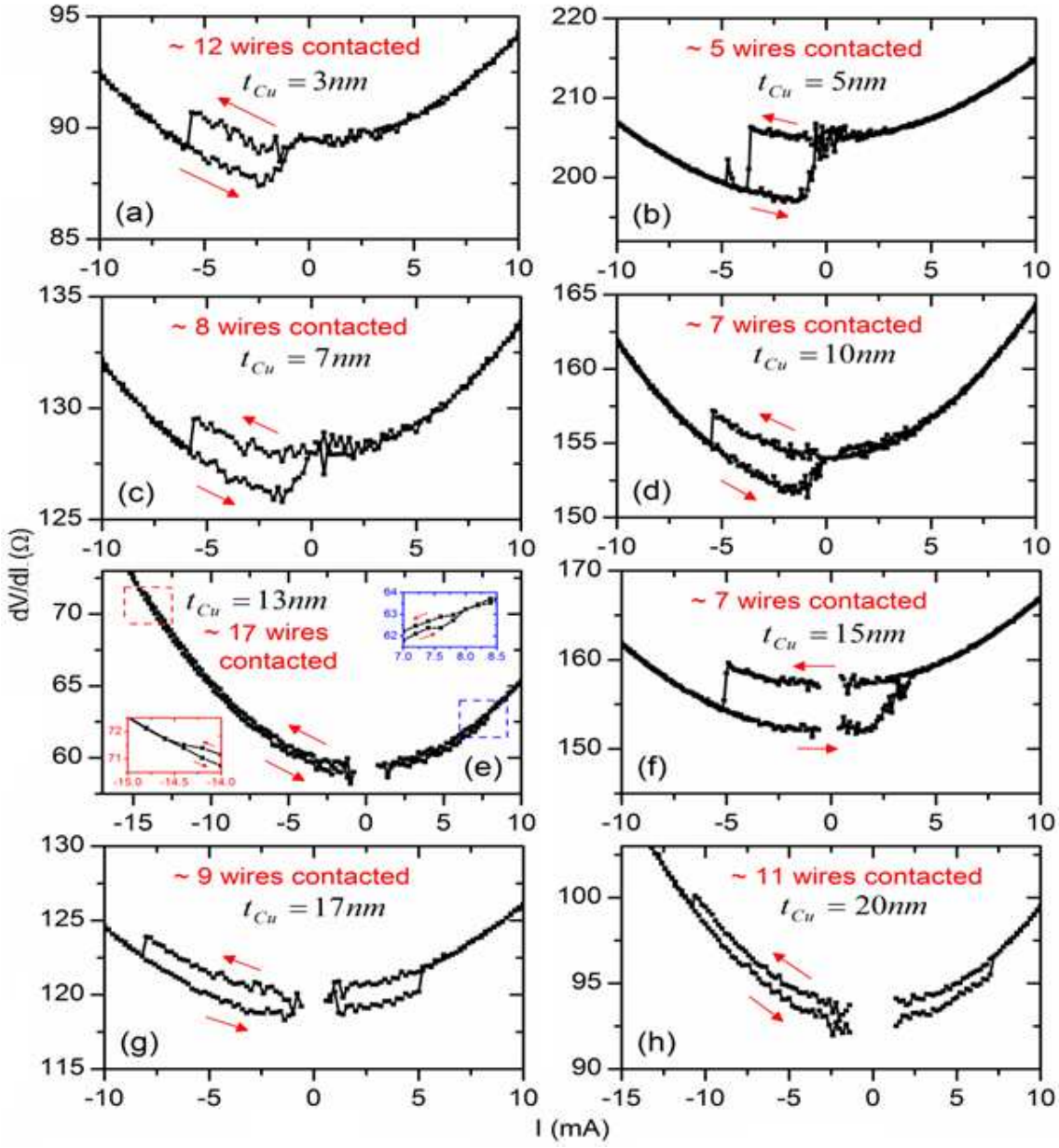

Fig. 6.4. STT switching in 200 bilayers of Co(10 nm)/Cu(tCu) where tCu is (a) 5 nm (b) 10 nm (c) 15 nm. The nanowire diameter is 100 nm. In all these cases, Cu leads were deposited to fill out the pores. The difference in resistance between samples is because our microprobe contacts different number of wires each time the measurement is made. It is important to distinguish here between the unipolar and bipolar switching as the spacer thickness is changed.

As clearly seen in Fig. 6.4(a-d), the LRS for wires having $t_{Cu} \leq 10$nm is not stable at zero current meaning that the Co magnetizations prefer a remanant AP state at these thicknesses. Given the fact that perpendicular anisotropy is observed for these thicknesses, one might expect a perpendicular AP state at remanance for these thicknesses. However, an in-plane AP state could also be possible given the expectedly high dipole fields at small interlayer thicknesses. Next, we will look at the dipole field effect and see how that may alter the conclusions taken from Fig. 6.3.

6.3.2.1. Dipole Field Considerations

In this section, we will estimate the dipole fields between the Co layers and between the neighboring wires, and we will determine which of these alters the switching process to make one particular magnetization configuration more favorable than another.

6.3.2.1.1. Intra-wire Dipole Fields

In this section we will estimate the dipole fields coming from the individual Co layers. To simplify the problem, we will calculate the field at the center Co layer of the multilayered nanowires. We will also assume uniform in-plane magnetizations, Fig. 6.5.

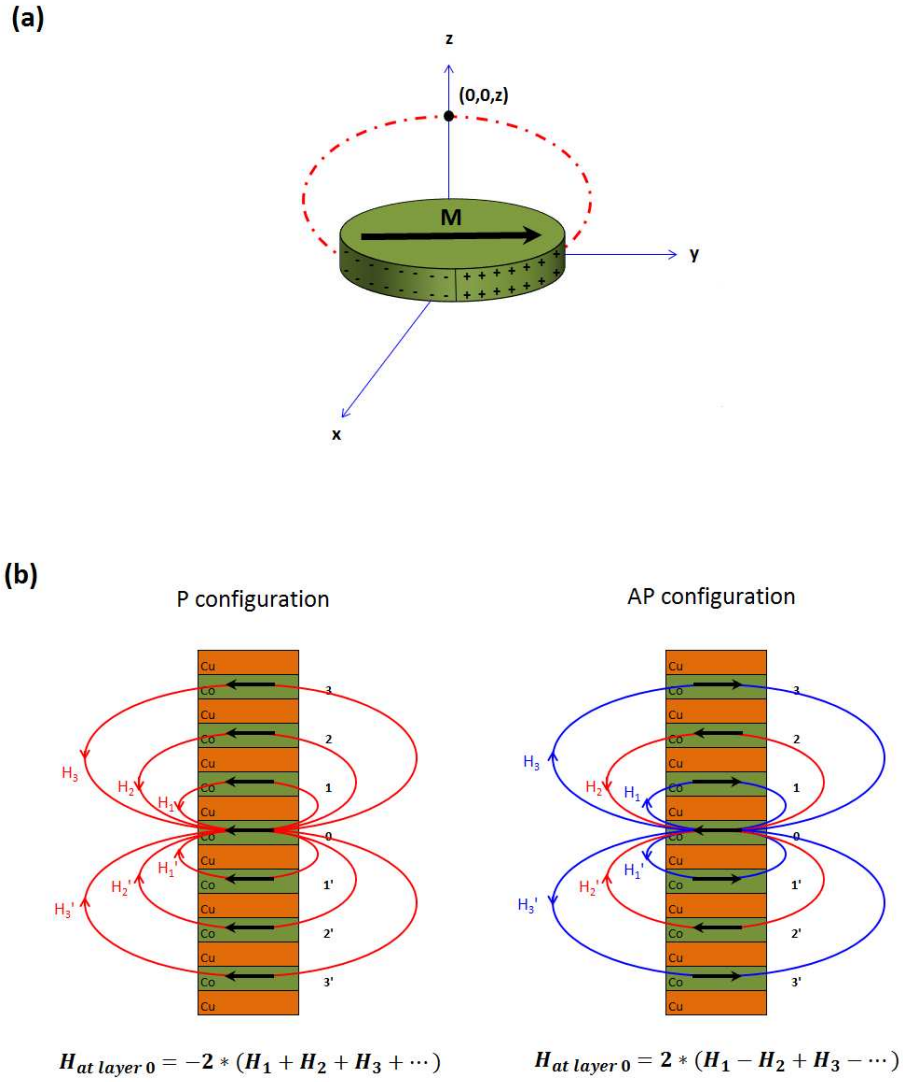

Fig. 6.5. (a) Dipole fields generated by a single Co layer with in-plane magnetization. (b) Schematics of in-plane P and AP magnetization configuration. Here, the dipole fields from all the layers are summed at the center Co layer.

As shown in Fig. 6.5, the field coming from each layer will be calculated at point (0,0,z) where z is the center-to-center spacing between that layer and the center Co layer.

Then all contributions are summed to give the total dipole field at the center layer. This will be done for both in-plane P and in-plane AP configurations.

The dipole field of Fig. 6.5a assuming uniform magnetization can then be evaluated from:

$$\vec{H}_{dip} = \frac{1}{4\pi}\int \frac{d^2 r' \vec{M}.\hat{n}'(\vec{r}-\vec{r}')}{\left|\vec{r}-\vec{r}'\right|^3} \qquad (6.1)$$

where M is the magnetization, *r* is the observation point, and *r'* is the source coordinates.

Figure 6.6 shows calculated dipole fields from equation (6.1) at the center Co layer as shown in the schematics of Fig. 6.5b. Here, all the dipole fields from all the layers are summed at the center layer. The diameter of the wires is 100nm and Ms=750emu/cm^3 (measured by VSM for electroplated Co film with known volume). The thickness of the Co layers is 10nm and the thickness of the spacer layer is varied from 1nm to 300nm.

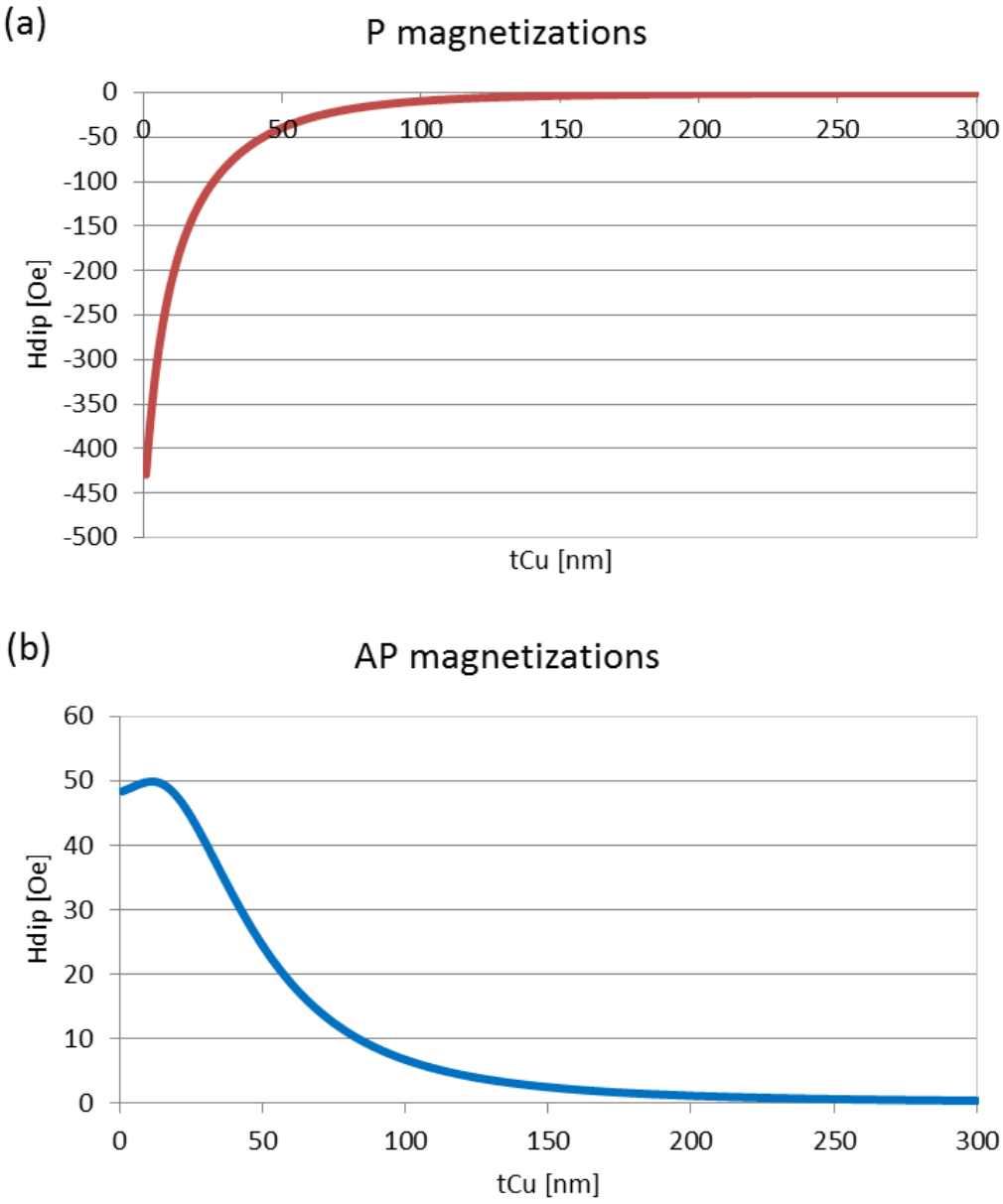

Fig. 6.6. Dipole field calculated from eq. (6.1) at the center Co layer as shown in schematics of Fig. 6.4 for both P and AP magnetizations.

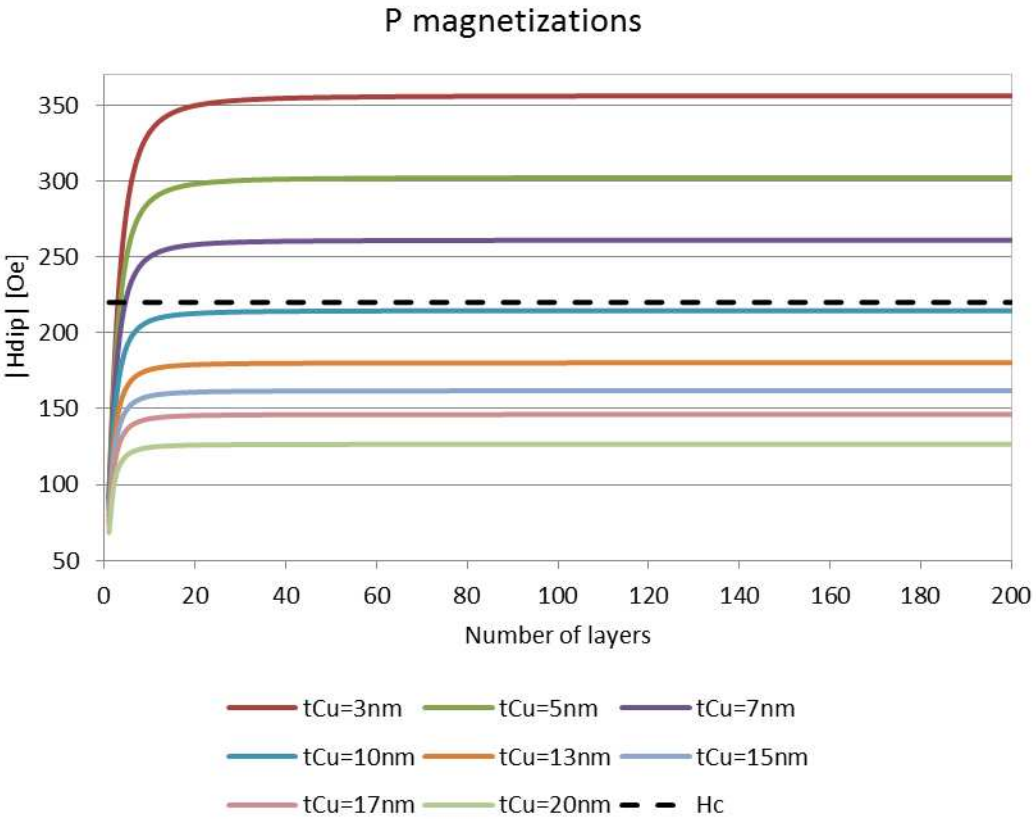

Fig. 6.7. Intra-wire dipole field vs number of Co/Cu layers.

Figure 6.7 shows the dipole field as a function of the number of layers for in-plane parallel magnetizations. As seen here, only the first few layers contribute to the total field seen at the center layer. Also, it can be seen that the dipole field for t_{Cu}<10nm is comparable to the coercivity of our nanowires (black dashed line) and thus can potentially switch the layers from one magnetization direction to the other. This can be related to what we experimentally observe in the STT switching loops for samples having t_{Cu} < 10nm shown in Fig. 6.4. However, the switching there is assumed to occur between perpendicular P state to an AP state with an unknown direction (inplane or perpendicular

to the plane). The question that arises is how can we use the dipole field effect calculated for in-plane P magnetizations if the initial state of Fig. 6.4 is perpendicular P magnetizations? The question is answered by looking at the coercivity vs angle curve shown in Fig. 6.8.

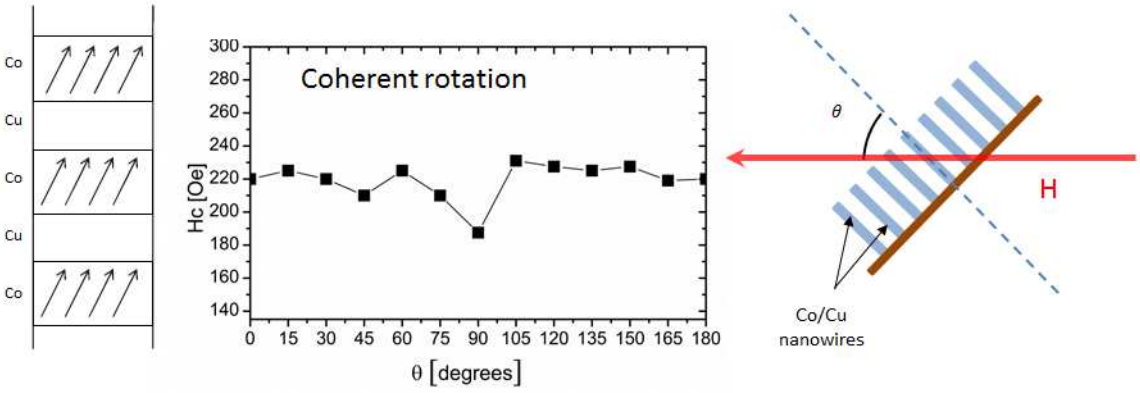

Fig. 6.8. Coercivity as a function of the applied field angle.

Figure 6.8 shows H_c vs angle for 100nm diameter Co[10nm]/Cu[5nm] multilayered nanowires. The fact that H_c reaches a minimum at 90^o somewhat indicates that magnetization reversal is done through coherent rotation of the moments of all the Co layers [147]. However, for coherent rotation H_c should reach zero at 90^o. The difference may be attributed to the fact that all nanowires are measured together and in electrodeposited nanowires, interfaces might be tilted between different nanwires which adds some averaging to the experiment [42]. Therefore, due to Fig. 6.8 showing a sign of coherent rotation, this assumption will be used for the rest of the text. This means when the moments coherently reverse, there will be a point where they lie in-plane of the Co

layers where dipole field is maximum and can force the layers to go from that state to an inplane AP state. However, for moments to start the coherent reversal process there should be an external force (field) that initiates the process. Next, we will look at such force which we'll call the interwire dipolar field, a field that comes from adjacent wires in a perpendicular direction or along the NW axis.

6.3.2.1.2. Inter-wire Dipole Fields

As discussed in chapter 2, the inter-wire dipole field for multilayered nanowires is given by:

$$H_{inter} = 6\pi M_s P * F \qquad (6.2)$$

where $6\pi M_s P$ is the inter-wire dipolar field for continuous magnetic wires and F is a factor representing the effect of layering (i.e., adding nonmagnetic spacers between the magnetic layers). This factor was previously derived for multilayered nanowires in a study that determined the effect on the demagnetizing field of the wires, [45] and is given by:

$$F = 1 - 3\sum_{i=0}^{N}(-1)^i N_i \qquad (6.3)$$

where N is the number of layers and N_i is the *i*th demagnetizing tensor that depends on the aspect ratios of the magnetic and nonmagnetic layers. Expressions for N_i and more details are found in [45]. Therefore, the inter-wire dipolar field of multilayered nanowire arrays is:

$$H_{inter} = 6\pi M_s P(1 - 3\sum_{i=0}^{N}(-1)^i N_i) \qquad (6.4)$$

Figure 6.9 shows the inter-wire dipole field for our 100nm diameter $[Co(10n)/Cu(t_{Cu})]_{200}$ multilayered nanowires as a function of t_{Cu} using Ms=750 emu/cm^3 and P=0.2. As shown, the field at t_{Cu}=0 is $6\pi M_s P$ and goes nearly to zero at very high t_{Cu}. This field is much higher than H_c for $t_{Cu} \leq$ 10nm and serves as the driving force to initiate magnetization coherent reversal from the initial perpendicular P of Fig. 6.4 (a-d).

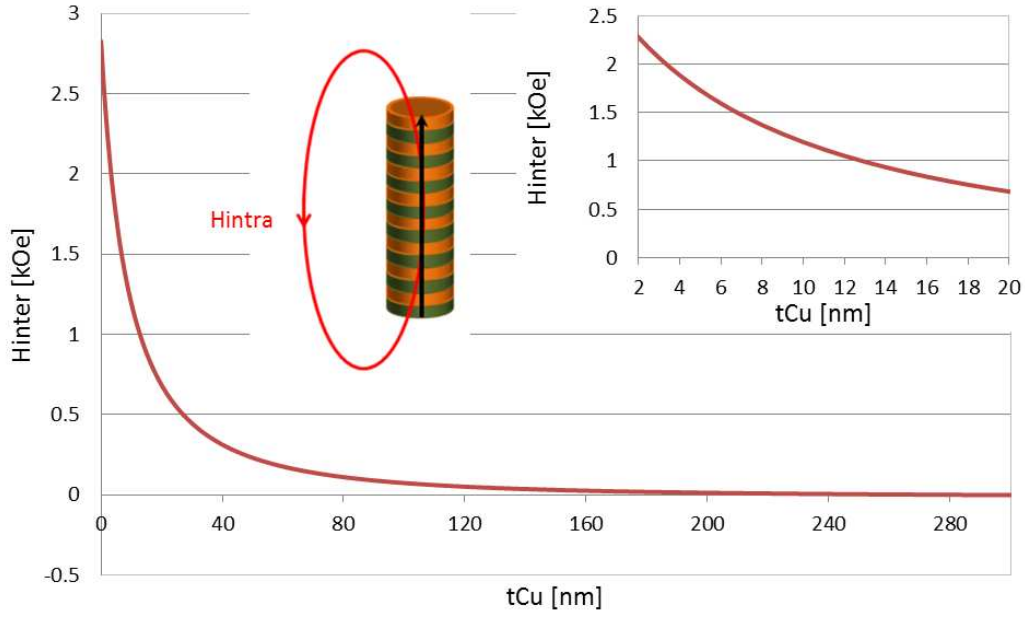

Fig. 6.9. Inter-wire dipole field of Co/Cu multilayered nanowire arrays as a function of tCu. Inset shows the region of tCu of the experimentally prepared samples.

The above finding of intra-wire and inter-wire dipole fields can be used now to explain the STT switching behavior (Fig. 6.4) of samples having $t_{Cu} \leq$ 10nm as follows. When the layers have perpendicular P magnetizations, the inter-wire dipole field is higher than H_c and will initiate coherent magnetization switching in the Co layers soon as the spin torque is reduced (i.e., when the current is swept back from -10mA towards zero). At

some point during this coherent switching, the moments will reach a parallel in-plane magnetization state where dipole fields come into play ($H_{dip} > H_c$) and will flip the magnetization of the layers to an in-plane AP state where layers have alternating AP magnetizations. The ΔR associated with this process eliminates the possibility of going from wires with perpendicular up magnetizations to wires with alternating up-down magnetizations. The inter-wire dipole field is thus the main reason why thin t_{Cu} samples have unstable perpendicular P state at zero currents. Also, as seen in Fig. 6.4 the thinner t_{Cu}, the earlier the P-AP switch and this is attributed to the fact that both intrawire and interwire dipole fields increase with thinner t_{Cu}, making the P configuration less stable at zero current. Next, we will look at the total energy of the system and we will determine whether our assumption of going from perpendicular P state to in-plane AP state, based on dipole field arguments, is feasible.

6.3.2.2. Total Energy Arguments

Investigating interwire and intrawire dipolar fields and looking at the magnetization reversal mechanism for thin Cu spacer samples suggested that the layers switch from perpendicular P state to in-plane AP state during the STT switching measurement at these thicknesses. This happens despite the observation of perpendicular anisotropy for these thicknesses.

To remove the ambiguity on which AP state exists at zero current (perpendicular AP or in-plane AP), we will look at the total energy content of these samples and determine which state is favorable and which is not. Also, we will look at the energy

content for all four magnetization configurations (perpendicular P/AP and inplane P/AP) to investigate the switching process from an energy perspective for the entire range of Cu thicknesses.

For Co/Cu multilayers with in-plane P or perpendicular P configurations, consider the tilted P magnetization configuration shown in the schematics of Fig. 6.1. Here, the total anisotropy energy at the center Co layer can be written as:

$$E_{TOT}^{P} = Ksin^2\theta + (1/2){M_s}^2(N_{eff}^{||P}sin^2\theta + N_{eff}^{\perp P}cos^2\theta) \qquad (6.5)$$

where $Ksin^2\theta$ is the uniaxial anisotropy energy, M_s is the saturation magnetization, θ is the angle between the magnetization and the NW axis. $N_{eff}^{||P}$ and $N_{eff}^{\perp P}$ are the effective demagnetization tensors at the center Co layer when the layers have in-plane or perpendicular to the plane P states, respectively. Note that substituting $\theta = 90°$ and $\theta = 0°$ in equation (6.5) gives the in-plane P or perpendicular to the plane P configuration. From ref. 45, the effective demagnetizing tensor for perpendicular P configuration is given by:

$$N_{eff}^{\perp P} = 2\pi\left[3\left|\sum_{i=0}^{(n-1)/2}(-1)^i N_i\right| - 1\right] \qquad (6.6)$$

The in-plane demagnetizing tensor $N_{eff}^{||P}$ can then be calculated from $N_{eff}^{||P} = (4\pi - N_{eff}^{\perp P})/2$.

For AP magnetizations, consider the tilted AP configuration of Fig. 6.1. Here, following the same strategy presented in [45], one can derive $N_{eff}^{||AP}$ and $N_{eff}^{\perp AP}$ for perpendicular AP magnetizations, in CGS units, as:

$$N_{eff}^{\perp AP} = 4\pi - 2N_{eff}^{||AP} = 2\pi\left[3\left|\sum_{i=0}^{(n-1)/2}(-1)^i(N_{2i}+N_{2i+1})\right|-1\right] \qquad (6.7)$$

And the total anisotropy energy for this tilted AP configuration will then be written as:

$$E_{TOT}^{AP} = Ksin^2\theta + (1/2){M_s}^2(N_{eff}^{||AP}sin^2\theta + N_{eff}^{\perp AP}cos^2\theta) \qquad (6.8)$$

Substituting $\theta = 90°$ and $\theta = 0°$ in equations (6.5) and (6.8) and including interwire and intrawire dipole fields for the in-plane P and perpendicular P magnetization configurations, respectively, yields:

$$E_{inplane}^{P} = K + (1/2)N_{eff}^{||P}{M_s}^2 + H_{intra}M_s \qquad (6.9)$$

$$E_{perp}^{P} = (1/2)N_{eff}^{\perp P}{M_s}^2 + H_{inter}M_s \qquad (6.10)$$

$$E_{inplane}^{AP} = K + (1/2)N_{eff}^{||AP}{M_s}^2 \qquad (6.11)$$

$$E_{perp}^{AP} = (1/2)N_{eff}^{\perp P}{M_s}^2 \qquad (6.12)$$

where H_{intra} and H_{inter} are the intra-wire and inter-wire dipole fields defined in equations (6.1) and (6.4), respectively. Note that the weak intra-wire dipole field for the inplane AP case (Fig. 6.6b) is not included in (6.11). The above energies are plotted for our 100nm diameter $[Co(10nm)/Cu(t_{Cu})]_{200}$ nanowires in Fig. 6.10. Here, tabulated values of K and M_s ($K=4.5\times10^6$ erg/cm^3, $M_s=1400$ emu/cm^3) were used here for simplicity.

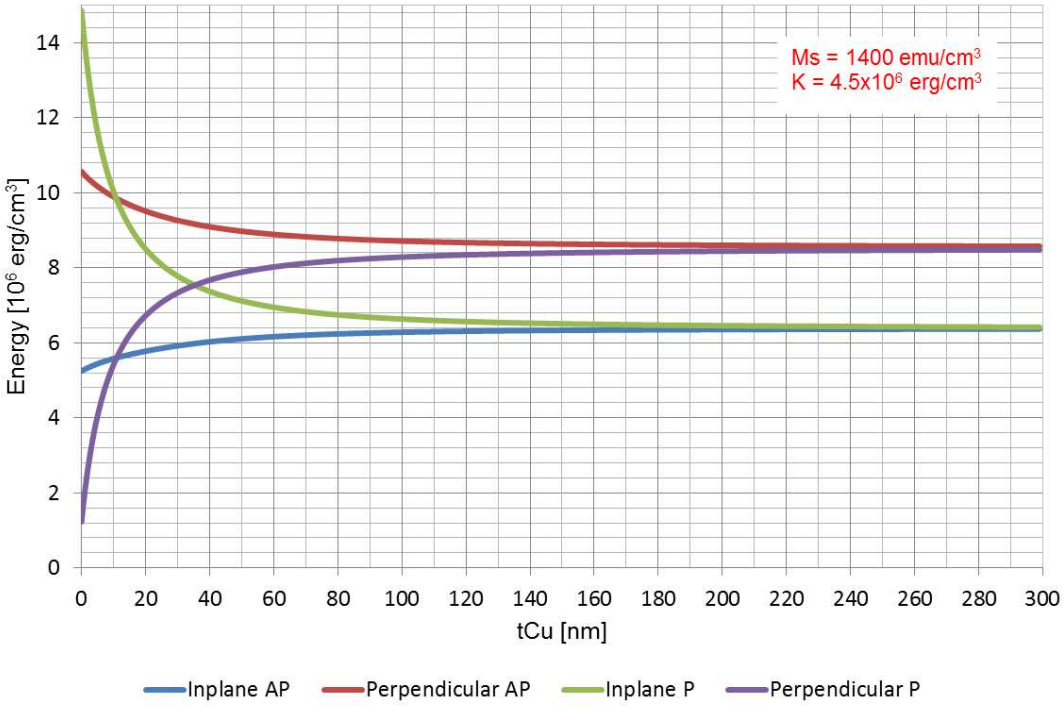

Fig. 6.10. Calculated energy for all possible magnetization configurations in our Co/Cu multilayered nanowires.

As seen in Fig. 6.10, the perpendicular P state is the most stable state at very thin t_{Cu} and then switches places with the inplane AP state at t_{Cu}~10nm where the latter becomes the most stable for the rest of the plot. The perpendicular P state continues to be the 2nd most stable state until t_{Cu}~35nm where the in-plane P state then takes over. Note that at very large t_{Cu} the effect of magnetization alignment on energy content vanishes where both P and AP start to have similar energies.

In our switching results of Fig. 6.4, the in-plane AP state is observed to be more stable than the perpendicular P state at thin Cu thicknesses. Also, the perpendicular P state switches to in-plane P due to change in anisotropy at t_{Cu}>10nm. Figure 6.10 does

not reflect our observed behavior. One reason is because it uses Ms=1400 emu/cm^3 which is about twice the measured Ms for our nanowires (750emu/cm^3). The other reason is possibly because our nanowires have much lower K than bulk. Figure 6.11 shows calculated energies using Ms=750emu/cm^3 and K=5x10^5 erg/cm^3. Here, the value of K was adjusted such that the energy curves match our STT switching observations. Note that recent micromagnetic simulations also used a much reduced K to reproduce experimental STT switching results of 60nm diameter Co/Cu multilayered nanowires [139].

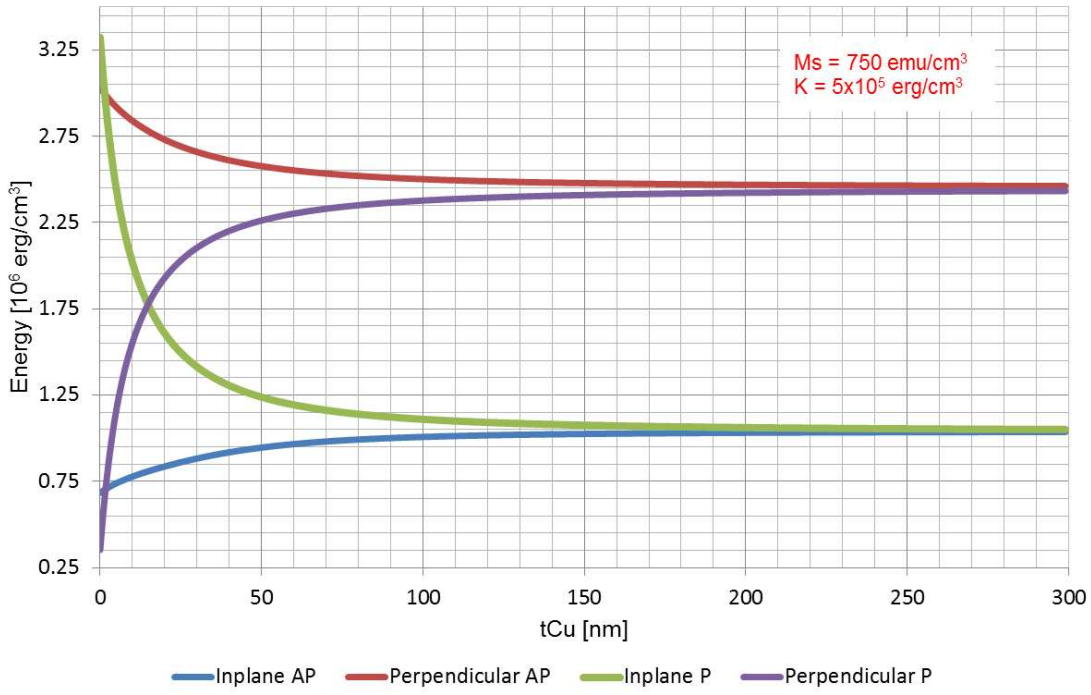

Fig. 6.11. Calculated energy for all possible magnetization configurations in our Co/Cu multilayered nanowires using reduced Ms and K.

It can be clearly seen in Fig. 6.11 that the in-plane AP state is the most stable state for all Cu thicknesses above 2nm. The next most stable state is perpendicular P from t_{Cu}=2nm to t_{Cu}=14nm but in-plane P is more stable afterwards. Figure 6.12 shows a zoomed in version of Fig. 6.11 with a shaded region showing the energy difference between the different magnetization configurations involved in our STT switching experiment. Here, it is interesting to see how the in-plane P state becomes more stable than perpendicular P at t_{Cu}~14nm, where experimentally that occurs at t_{Cu}=13nm. This is a close agreement between calculation and experiment.

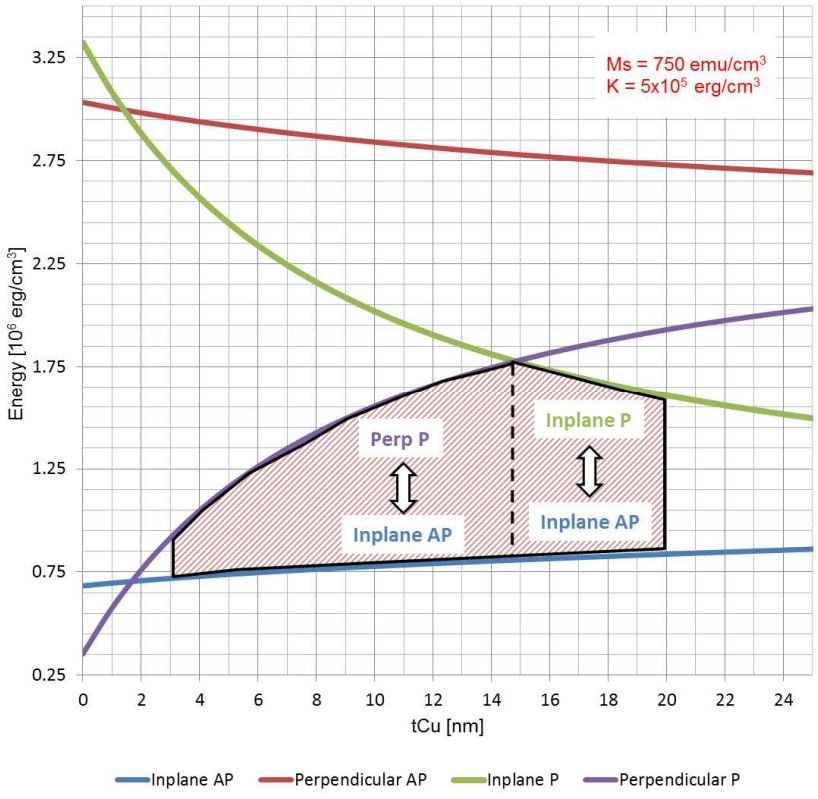

Fig. 6.12. Zoomed in version of Fig. 6.11 showing regions of switching for our implemented samples.

The trend seen in our switching results can now be summarized as follows. For small Cu interlayer thicknesses, the magnetization easy axis is perpendicular to the plane of the Co layers (along NW axis) but STT switching takes place between a perpendicular P state and in-plane AP state rather than switching between both perpendicular P and AP states. This is due to the high interwire and intrawire dipole field interactions at these thicknesses which was also verified using energy calculations. For larger Cu thicknesses, the magnetization easy axis is in the plane of the Co layers and the switching happens between in-plane P and AP states, Figure 6.13. Here, the switching current densities $J_c=I_c/A$ vs copper interlayer thickness t_{Cu}, where A is the total area of the contacted wires, are plotted showing the different regions of magnetic anisotropy. The data points are measured values and the error bars represent repeated measurements on the same sample and on samples having similar structures. The variation has the same origin as that seen for the MR ratio discussed earlier in the text.

Compared to traditional spin valves, it can be seen in Fig. 6.13 that it takes more current to switch from AP to P rather than P to AP (normally smaller because reflected electrons usually cause the P-AP switch). There reason behind this is that in-plane AP state is observed to be very stable and thus it takes more current to overcome the energy barrier to a less stable state even though the torque efficiency is higher. This kind of STT switching was observed before in multilayered Co/Cu nanowires [13,14,148] but never was explained due to the lack of such energy and dipole field calculations.

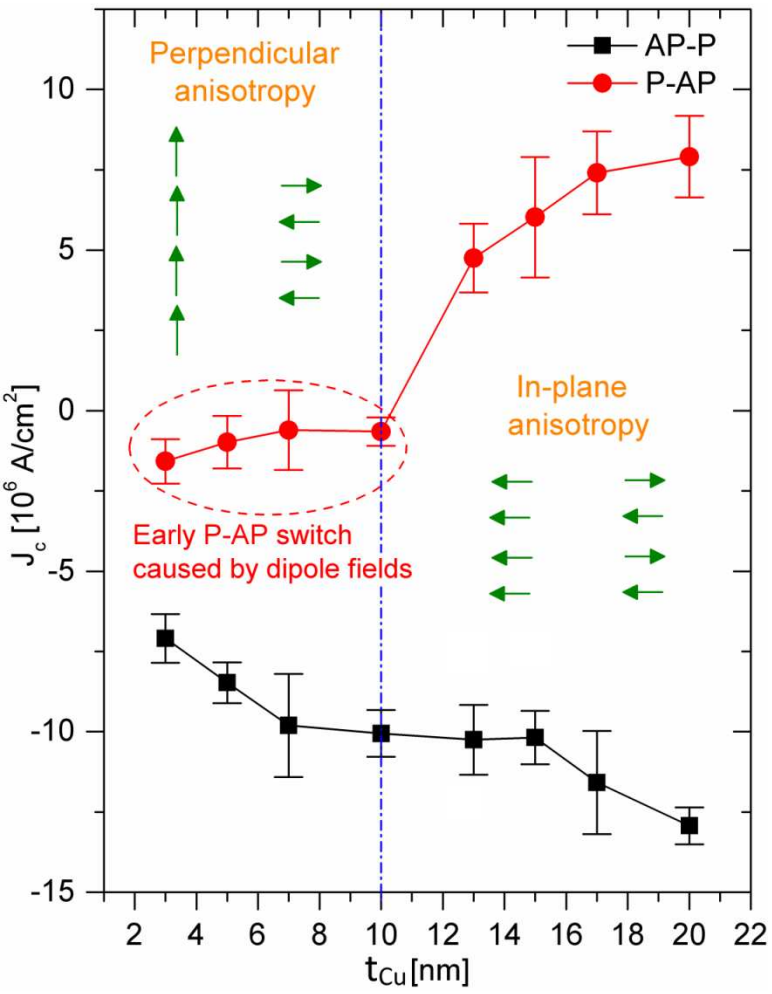

Fig. 6.13. Switching current density as a function of t_{Cu} with defined regions of anisotropy.

In Fig. 6.13, ignoring the region where dipole fields force an early P-AP switch, the magnitudes of both switching current densities J_c^{AP-P} and J_c^{P-AP} increase with the Cu interlayer thicknesses. This can be attributed to three different mechanisms; the spin relaxation effect, the direction of the magnetic anisotropy (perpendicular or in-plane), and the effective demagnetizing field acting on each Co layer. From Ref. 144, the switching

current densities were shown to scale with e^{t_{Cu}/λ_s} where λ_s is the spin relaxation length. For our interlayer thicknesses $3 \leq t_{Cu} \leq 20$ nm and using λ_s=150nm [144], this effect can explain only 12% increase in J_c while the observed increase exceeds 100% in both $J_c^{P\text{-}AP}$ and $J_c^{AP\text{-}P}$. There is also an increase in switching current densities due to the change of anisotropy direction from perpendicular to the plane at small t_{Cu} to in-plane of the Co layers at larger t_{Cu}. As seen in Fig. 6.13, J_c is smaller for the perpendicular anisotropy region owing to the collinear demagnetizing and anisotropy fields. This effect was first demonstrated by Meng et al. [149] and Mangin et al. [145] and has been used for most spintronics applications since. The effective demagnetizing field effect is discussed next.

6.3.3. EFFECTIVE DEMAGNETIZING FIELD

An effective demagnetizing field can be used to explain the large dependence of J_c on t_{Cu}. This effective demagnetizing field, acting on each Co layer, can be calculated by considering all possible magnetization configurations (perpendicular P and AP, in plane P and AP). According to Medina et al. [45], the effective demagnetizing field seen at the center Co layer in a multilayered Co/Cu nanowire within an array of porosity P, assuming parallel alignment of Co magnetizations along the NW axis (perpendicular to the plane), is given by:

$$H_{eff}^{\perp P} = 2\pi M_s(1-3P)\left[1-3\left|\sum_{i=0}^{n}(-1)^i N_i\right|\right] \qquad (6.4)$$

where n and N_i are defined earlier. Similarly, for antiparallel AP magnetizations along the

NW axis, the effective field can be derived as:

(6.5)

The in-plane versions of these equations can be found by solving for and then calculating where then can be calculated. These fields are calculated and plotted in Fig. 6.14.

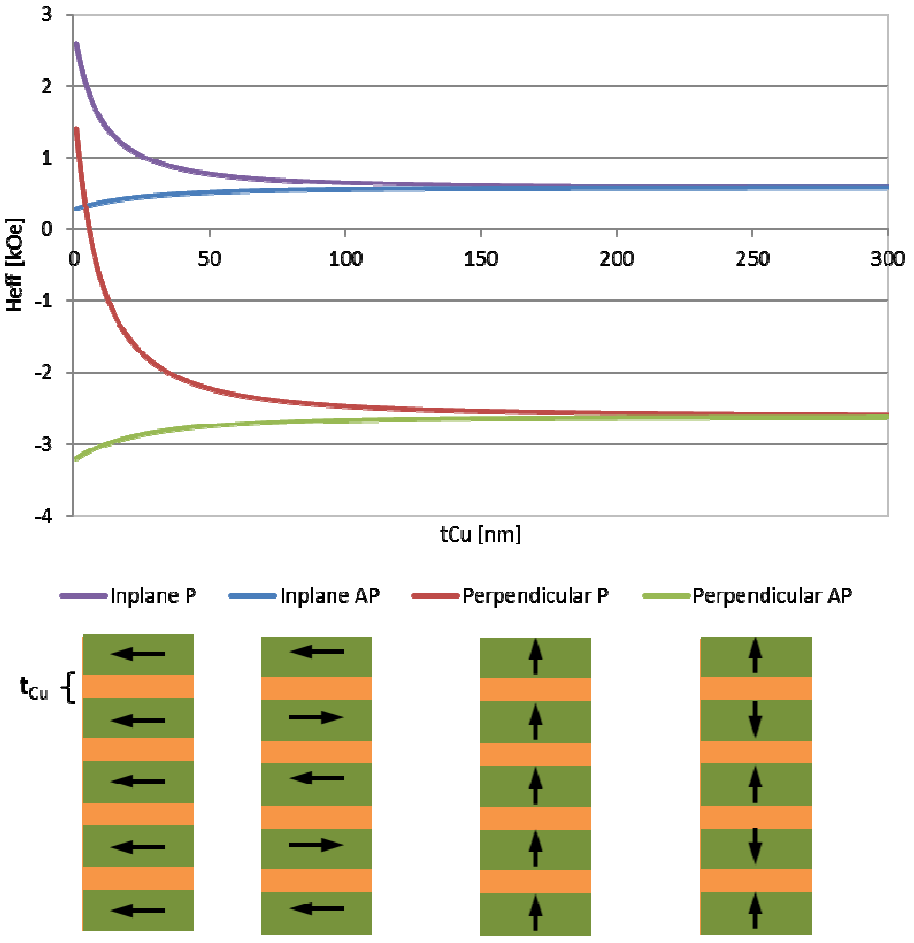

Fig. 6.14. Effective demagnetizing field as a function of the Cu spacer thickness. Negative values indicate fields opposite to the magnetization.

In Figure 6.15, the measured switching current densities $J_c^{AP\text{-}P}$ and $J_c^{P\text{-}AP}$ are plotted versus calculated H_{eff}^{AP} and H_{eff}^{P}, respectively, showing the two regions of anisotropy (|| and ⊥). This is because to switch from *AP* to *P* an effective field of H_{eff}^{AP} must be overcome and similarly a field of H_{eff}^{P} is needed to overcome when switching from P to AP. In Fig. 6.15a, the magnitude of the switching current density increases with the magnitude of the effective field with almost the same slope for in-plane and perpendicular anisotropy. This is because the AP state seen in our structures is always in the plane of the Co layers which results in similar spin torque efficiency (i.e., dJ_c/dH_{eff}) for both regions. The nearly flat behavior around the dashed line indicates that the system locks into the isotropic state for interlayer spacer thicknesses around 10nm resulting in a nearly constant current density for this range of thicknesses. The switching from P to AP is shown in Fig. 6.15b. Here, unlike the AP-P switching, two distinct P configurations were seen (perpendicular P and in-plane P). For both regions, it is seen that as the effective fields gets more negative (opposite to magnetization direction), the magnitude of the switching current density decreases with a clear difference in dJ_c/dH_{eff} for the two regions owing to dissimilar spin torque efficiencies for the two anisotropy directions [145]. It can be clearly seen now that the switching current densities depend greatly on the effective demagnetizing field seen in the array and that adds to the spin relaxation effect in explaining the huge increase in J_c seen in Fig. 6.13.

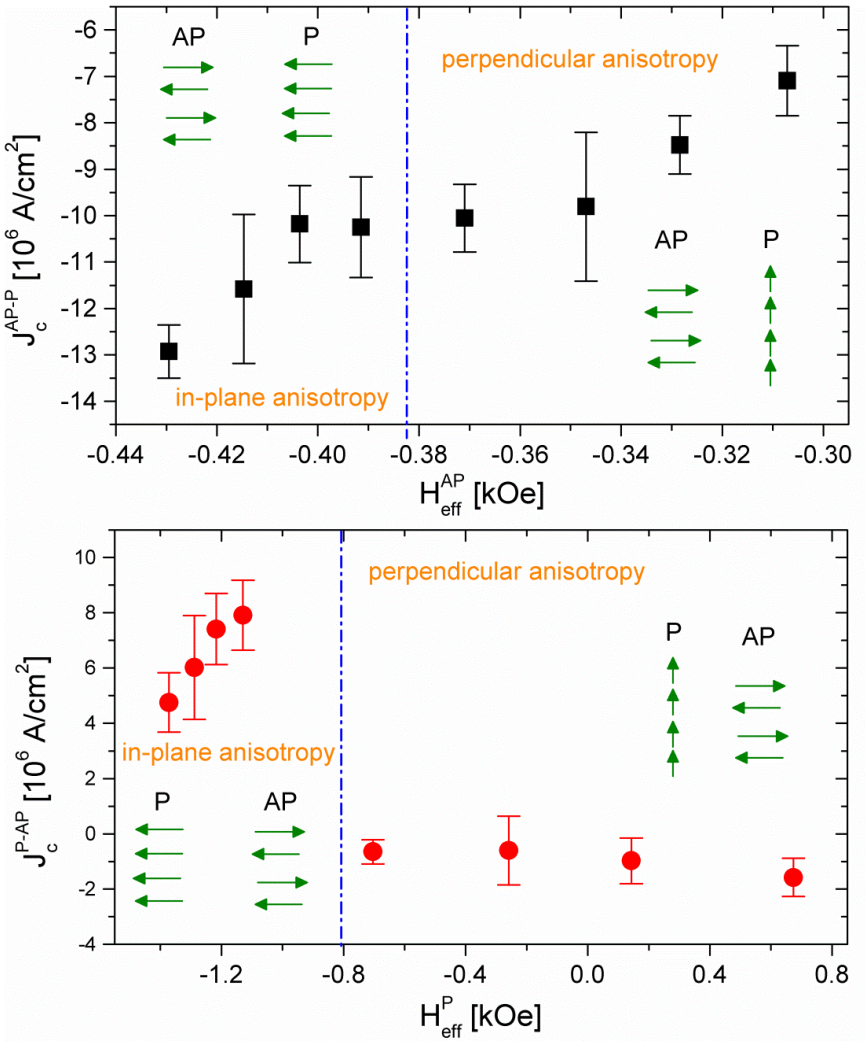

Fig. 6.15. Switching current densities vs Heff when (a) the layers switch from AP to P and (b) when the layers switch back from P to AP.

It is important to note that the effective field given in equations (6.4) and (6.5) is always less than that of a single nanopillar structure. This reduction comes from both the array-like geometry ($P > 0$) and the layering effect ($N_{eff} < N_0$) where N_0 is the demagnetizing tensor for a single Co layer. Therefore, the spin torque switching current

densities of arrays of multilayered structures are always less than those of single nanopillar systems. This opens the way to implementing these structures in devices like spin torque random access memories (ST-RAM) where high density and low switching currents are both favorable. Similar behavior was reported before for nanopillar systems where the demagnetizing field of the free layer was partially cancelled using Co/Ni stacks as the free layer [150]. However, it is important to note here that the MR ratio for the un-stacked system was already small and was further reduced when using Co/Ni stacks for the free layer. Our structures have MR ratios as high as 30% and can be grown into arrays with very low cost and very low resistance area product (2.66 $\Omega\mu m^2$). Although RA product is higher than those observed in GMR trilayered nanowires in the previous chapter [18], they are still low compared to magnetic tunnel junctions.

6.4. CONCLUSIONS

In conclusion, spin torque switching of 100nm diameter Co(10nm)/Cu(d) multilayered nanowires was observed under zero applied magnetic fields. Although these wires have perpendicular to the plane Co c-axis, they were shown to change their effective magnetic anisotropy from perpendicular to the plane of the Co layers to in-plane as the Cu interlayer thickness increased. The high resistance state was shown to always refer to an antiparallel in-plane state irrespective of the anisotropy direction, which was supported by both the dipole field effect and total energy considerations. The spin torque switching current densities of these multilayers were 2-3 orders of magnitude less than

those seen in previous electrodeposited Co/Cu/Co trilayers. This was a result of the significantly smaller demagnetizing field seen in each Co layer. Being able to tune the demagnetizing field in these structures, along with the possibility of cancelling the dipole fields makes these engineered structures very promising candidates for future spin torque random access memories (ST-RAM).

Chapter 7

Conclusions and Future Work

7.1. CONCLUSIONS

In this work, we were able to fabricate anodic aluminum oxide templates by two-step anodization of aluminum with pore diameters of 10-500nm. These templates were fabricated as free standing membranes and as integrated films on Si substrates. The barrier layer for templates made on Si was cleverly removed by running the second anodization step longer than required to allow for the anodization solution to break the barrier in attempts to reach the bottom electrode.

Next, electrodeposition of Co and Cu nanowires in these membranes was precisely controlled such that thickness as small as 3nm were possible. The crystalline anisotropy was tuned by adjusting either the deposition voltage or the pH of the electrolyte containing the metallic cations (Cu^{+2} and Co^{+2}). Resistance versus field and magnetization hysteresis loops for Co/Cu multilayered nanowires were measured to determine the coercivity and the variation in easy axes of the Co layers.

The feasibility of a new class of read sensors for ultra-high density recording using integrated 10nm-diameter nanowires was demonstrated. The resistivity of these

10nm wires was measured to be 5.4 μΩcm, a three times lower than the bulk value for Cu. This resulted in a resistance-area product of 2 mΩμm^2 and 20-30Ω per sensor. We attribute much of our advantages at these very small dimensions to the *in situ* growth with no need for sidewall etching. Overall, the all-metallic giant magnetoresistive sensors presented here provide an unusual opportunity to incorporate the techniques of modern nanotechnology to enable the future high density growth of this economically important technology.

Spin torque switching of multilayered Co/Cu nanowires in anodic aluminum oxide (AAO) templates was controlled such that the parallel-antiparallel critical current density ($J_c^{P\text{-}AP}$) varied from negative to positive values by proper design of the layer thicknesses. Close-packed GMR arrays such as these have recently drawn significant attention because of their potential use in applications like magnetic and spin transfer torque random access memory (MRAM and STT-RAM). In this study, Co(10nm)/Cu(t_{Cu}) multilayered nanowires with 100nm diameters were electrodeposited. Spin transfer torque (STT) switching of these multilayered nanowires was observed under zero external fields with switching current densities below 10^7 A/cm^2 with MR ratios of 30%. Traditionally, applying an external magnetic field can cause the switching curve to shift left or right depending on the direction of applied field. Here, shifting of the loop was successfully achieved by varying the nonmagnetic layer thicknesses (t_{Cu}) with a slight change in the critical currents. It was found that increasing the Cu thickness from 2nm to 20nm changed the critical $J_c^{P\text{-}AP}$ switching current density from being negative to positive. In the latter structures, at zero current both P and AP states (1 or 0) were stable,

all without the need for external fields. This is extremely important because for real devices (especially STT-RAM), external magnetic fields add undesirable complexity to the system. The unipolar switching behavior at thin Cu thicknesses (both current densities are negative) was attributed to the high interwire and intrawire dipolar fields, which was also confirmed by simple energy calculations. Although increasing the Cu thickness resulted in ideal switching curves, the critical current densities increased slightly. However, these current densities are significantly smaller than those for trilayered structures with similar dimensions. The reduction in current density is attributed to the reduced demagnetizing field for the Co/Cu multilayered nanowire. This demagnetizing field was successfully calculated and proven to be smaller than that of trilayered structures. The ability to tune the demagnetizing field and to fully understand the dipole fields and energies, even though these were calculated using simple and ideal environments, will attract more interest in the future and such structures will be perfect candidates for future STT-RAMs.

7.2. FUTURE WORK

Co/Cu multilayered nanowires were successfully shown to have good magnetic and structural properties for applications like magnetic read sensors and spin transfer torque RAM. However, there is more to be done to more optimize these structures for these applications.

For fabrication point of view, structural and imaging practices like XRD, TEM, and SEM should be made more routine to enhance the quality of the samples and to reduce the time spent on testing afterwards.

For read sensor applications, more work is needed to prove the feasibility of our design as a potential read head. This means biasing the free layer, adding magnetic shields, and introducing more pinning to the fixed layer. Also, after these are integrated into more complete head designs, performance measurements like SNR and BER should be made before the design is finalized.

For STT-RAM, the spin torque switching experiment should be done under the influence of perpendicular and in-plane fields to confirm our conclusions of the interwire and intrawire dipole field effects. Then, our simple dipole field and energy arguments should be replaced with more realistic calculations based on micromagnetic simulations. More can be done in tuning the demagnetizing field of the array. Based on equations (6.4) and (6.5), the thicknesses can be designed to make H_{eff} close to zero, which we think will reduce the switching current densities even further. Finally, given the very high aspect ratios that are possible for electrodeposited nanowires, it is possible to incorporate several multilayered bits into each wire to enable multi-state areal bits for extremely high density RAM. If all of these suggestions are made, then our Co/Cu multilayered nanowires will be excellent candidates for future spin torque random access memories.

REFERENCES

1. Moore, G. E., *Electronics* **1965**, 38, 114.

2. Parkin, S.S.P.; Fontana, R.E.; Marley, A.C., *J. Appl. Phys.* **1997**, 81, 8, 5521.

3. Fert et al., *Phys. Rev. Lett.* **1988**, 61, 21, 2472.

4. Wang, D.; Nordman, C.; Daughton, J. M.; Qian, Z.; Fink, J., *IEEE Trans. Magn.* **2004**, 40, 4, 2269.

5. Berkowitz, A. E.; Mitchell, J. R.; Carey, M. J.; Young, A. P.; Zhang, S.; Spada, F. E.; Parker, F. T.; Hutten, A.; Thomas, G., *Phys. Rev. Lett.* **1992**, 68, 25, 3745.

6. www.everspin.com

7. Fukuzawa, H.; Yuasa, H.; Hashimoto, S.; Koi, K.; Iwasaki, H.; Takagishi, M.; Tanaka, Y.; Sahashi, M., *IEEE Trans. Magn*. **2004**, 40, 4, 2236.

8. Peng, X.; Kolbo, P.; Nikolaev, K.; Chen, S.; Wang, Z.; Boonstra, T.; Anderson, P.; Kalderon, S.; Czoschke, P.; Morrone, A.; Dimitrov, D.; Xue, S.; Chen, Y., *J. Magn. Magn. Mater.* **2009**, 321, 1889.

9. Furubayashi, T.; Kodama, K.; Sukegawa, H.; Takahashi, Y. K.; Inomata, K.; Hono, K., *Appl. Phys. Lett.* **2008**, 93, 122507.

10. Nakatani, T.M.; Furubayashi, T.; Kasai, S.; Sukegawa, H.; Takahashi, Y.K.; Mitani, S.; Hono, K., *Appl. Phys. Lett.* **2010**, 96, 212501.

11. Taylor, R. C.; Tsuei, C. C., *Solid State Communications* **1982**, 41, 503.

12. Galanakis, I.; Ozdogan, K.; Sasioglu, E., *J. Appl. Phys.* **2008**, 104, 83916.

13. Tan, L., ProQuest Dissertations And Theses; Thesis (Ph.D.)--University of Minnesota **2009**, Publication number: AAI3344228, Dissertation Abstracts International, Volume: 70-01, B, 0431.

14. Huang, X.; Tan, L.; Cho, H.; Stadler, B. J. H., *J. Appl. Phys.* **2009**, 105, 07D128.

15. Reddy, S. M.; Park, J. J.; Na, S.-M.; Maqableh, M. M.; Flatau, A. B.; Stadler, B. J. H., *Adv. Funct. Mater.* **2011**, 21, 24, 4677.

16. Piraux, L.; Dubois, S.; Duvail, J. L.; Ounadjela, K.; Fert, A., *J. Magn. Magn. Mater.* **1997**, 175, 127.

17. Maqableh., M. M.; Tan, L.; Huang, X.; Cobian, R.; Norby, G.; Victora, R. H.; Stadler, B. J. H., *IEEE Trans. Magn.* **2012**, 48, 1-7.

18. Maqableh, M. M.; Huang, X.; Sung, S.-Y.; Reddy, K. S. M.; Norby, G.; Victora, R. H.; Stadler, B. J. H., *Nano Lett.* **2012**, 12, 4102−4109.

19. Maekawa, S.; Shinjo, T., Spin Dependent Transport in Magnetic Nanostructures (book), *CRC Press LLC* **2002**, pg 81.

20. Piraux, L.; Dubois, S.; Demoustier-Champagne, S., *Nuclear Instruments & Methods in Physics Research* **1997**, Section B, v 131, n 1-4, p 357-63.

21. Rani, V.S.; Yoon, S.S.; Rao, B.P.; CheolGi Kim, *Materials Chemistry and Physics* **2008**, 112, 3, 1133-6.

22. Routkevitch, D.; Bigioni, T.; Moskovits, M.; Xu, J. M., *J. Phys. Chem.*, **1996**, 100, 33,14037–14047.

23. Apel, P., *Radiation Measurements* **2001**, 34, 559.

24. Park, S.; Lee, D. H.; Xu, J.; Kim, B.; Hong, S. W; Jeong, U.; Xu, T.; Russell, T. P., S*cience* **2009**, 323, p 1030.

25. Masuda, H.; Fukuda, K., *Science* **1995**, 268, 1466.

26. Zou, J.; Qi, X.; Tan, L; Stadler, B. J. H., *Appl. Phys. Lett* **2006**., 89, 9, pp 93106.

27. Lee, W.; Ji, R.; Gösele, U.; Nielsch, K., *Nat. Mater.* **2006**, 5, 741-747.

28. Sulkaa, G. D.; Stepniowski, W. J., *Electrochimica Acta* **2009**, 54, 3683–3691.

29. Lim, S.K., Jeong, G.H., Park, I.S., Na, S.M., Suh, S.J., *J. Magn. Magn. Mater.* **2007**, 310, e841-e842.

30. Mazin Maqableh, Xiaobo Huang, and Beth Stadler, *MRS Proceedings* **2009**, Volume 1160.

31. Zheng, M.; Menon, L.; Zeng, H.; Liu, Y.; Bandyopadhyay, S.; Kirby, R. D.; Sellmyer, D. J., *Phys. Rev. B* **2000**, 62, 12282–12286.

32. Yang, S.; Zhu, H.; Yu, D.; Jin, Z.; Tang, S.; Du, Y., *J. Magn. Magn. Mater*. **2000**, 222, 1–2, p97–100.

33. Zeng, H.; Zheng, M.; Skomski, R.; Sellmyer, D. J.; Liu, Y.; Menon, L.; Bandyopadhyay, S., *J. Appl. Phys.* **2000**, 87, 4718.

34. Fashen Li, Tao Wang, Liyuan Ren and Jianrong Sun, *J. Phys.: Condens. Matter* **2004**, 16, 8053–8060.

35. Rabin, O.; Herz, P. R.; Lin, Y.-M.; Akinwande, A. I.; Cronin, S. B.; Dresselhaus, M. S., *Adv. Funct. Mater*. **2003**, 13, 8, p631–638.

36. Rani, V.S.; AnandaKumar, S.; Kim, K. W.; Yoon, S.S.; Jeong, J.-R.; CheolGi Kim, *IEEE Trans. Magn.* **2009**, 45, 6, 2475.

37. Gerein, N. J.; Haber, J. A., *J. Phys. Chem. B* **2005**, 109, 17372-17385.

38. McGary, P. D., ProQuest Dissertations And Theses; Thesis (Ph.D.)--University of Minnesota **2008**, Publication number: AAI3316145, Dissertation Abstracts International.

39. Fert, A.; Piraux, L., *J. Magn. Magn. Mater*. **1999**, 200, issues 1-3, 338-358.

40. García, J.M.; Thiaville, A.; Miltat, J., *J. Magn. Magn.* Mater. **2002**, 249.

41. Darques, M.; Piraux, L.; Encinas, A.; Bayle-Guillemaud, P.; Popa, A.; Ebels, U., *Appl. Phys. Lett.* **2005**, 86, 7, p 72508-1-3.

42. Darques, M.; Bogaert, A.-S.; Elhoussine, F.; Michotte, S.; De La Torre Medina, J.; Encinas, A.; Piraux, L., *J. Phys. D* **2006**, 39, 23, p 5025-32.

43. Routkevitch, D.; Bibioni, T.; Moskovits, M.; Xu, J. M., *J Phys. Chem.* **1996**, 100, 14037–47.

44. Song et *al.*, *Materials Letters* **2011**, 65, 1562–1564.

45. La Torre Medina, J.; Darques, M.; Blon, T.; Piraux, L.; Encinas, A., *Phys. Rev. B* **2008**, 77, 1, 014417-1-9.

46. Tan, L.; McGary, P. D.; Stadler, B. J. H., *J. Appl. Phys.* **2008**, 103, 07B504.

47. Tan, L.; Stadler, B. J. H., *J. Mater. Research* **2006**, 21, 11, p 2870-5.

48. Mott, N. F., *Advances in Physics* **1964**, 325.

49. Slonczewski, J. C, *J. Magn. Magn. Mater.* **1996**, 159, L1-L7.

50. Berger, L., *Phys. Rev. B* **1996**, 54, 13.

51. E. B. Myers, D. C. Ralph, J. A. Katine, R. N. Louie, and R. A. Buhrman, *Science* **1999**, 285, 867–870.

52. Bussmann, K.; Prinz, G. A.; Cheng, S.-F.; Wang, D., *Appl. Phys. Lett.* **1999**, 75, 2476.

53. Schrag et *al.*, *Appl. Phys. Lett.* **2000**, 77, 15.

54. M.A. Ruderman and C. Kittel, *Phys. Rev.* **1954**, 96, 99.

55. T. Kasuya, *Prog. Theor. Phys.* **1956**, 16, 45.

56. S. S. Parkin, N. More, and K. P. Roche, *Phys. Rev. Lett.* **1990**, 64, 2304.

57. Krimpalis, S.; Chiriac, H., *IEEE Trans. Magn.* **2012**, 48, 9, 2455-2460.

58. J. Park, M. Reddy, B.J. Stadler, and A.B. Flatau, Hysteresis measurement of individual multilayered Fe-Ga/Cu nanowires using magnetic force microscopy, 12th joint MMM-intermag conference, Chicago, IL, Jan 2013.

59. A. Encinas, M. Demand, and L. Piraux, *Phys. Rev. B.* **2001**, 63, 104415,.

60. Carl Wagner, Calculation of the current distribution at electrodes involving slots, *Plating* **1961**.

61. M. E. Orazem and J. Newman, *J. Electrochem. Soc.* **1984**, 131, 2857.

62. A. C. West and J. Newman, *J. Electrochem. Soc.* **1991**, 138, 6.

63. Comsol Multiphysics, “Electrochemical Copper Deposition”, Solved with Comsol Mutliphysics 3.5a.

64. www.synkera.com.

65. A. Belwalkar, E. Grasing, W. Van Geertruyden, Z. Huang, W.Z. Misiolek, *J. Membr. Sci.* **2008**, 319, 192–198.

66. Bo Yan, Hoa T. M. Pham, Yue Ma, Yan Zhuang, Pasqualina M. Sarro, *Appl. Phys. Lett.* **2007**, 91, 053117.

67. Cai-Ling Xu, Hua Li, Guang-Yu Zhao, Hu-Lin Li, *Appl. Surf. Sci.* **2006**, 253, 1399-1403.

68. Filimon Zacharatos, Violetta Gianneta, and Androula G. Nassiopoulou, *Nanotechnology* **2008**, 19, 495306.

69. M. Tian, S. Xu, J. Wang, N. Kumar, E.Wertz, Q. Li, P.M. Campbell, M. Chan, and T.E. Mallouk, *Nano Lett.* **2005**, 5, 697-703.

70. C. L. Xu, H. Li, G. Y. Zhao, and H. L. Li, *Mater. Lett.* **2006**, 60, 2335-2338.

71. K. Liu, K. Nagodawithana, , P.C Searson, C.L Chien, *Phys. Rev. B* **1995**,51, 11, 7381-4.

72. M. Kashi, A. Ramazani and A. Khayyatian, *J. Phys. D: Appl. Phys.* 2006, 39, 4130–4135.

73. Jinxia Xu, Yi Xu, *Mater. Lett.* **2006**, 60, 2069–2072.

74. T. Blon, M. Matefi-Tempfli, S. Matefi-Tempfli, L. Piraux, S. Fusil, R. Guillemet, K. Bouzehouane, C. Deranlot, and V. Cros, *J. Appl. Phys.* ,102, 103906.

75. Piraux, L; Renard, K.; Guillemet, R.; Mátéfi-Tempfli, S.; Mátéfi-Tempfli, M.; Andrei Antohe, V.; Fusil, S.; Bouzehouane, K.; Cros, V, *Nano Lett.* **2007**, 7, 2563-2567.

76. Yan, H.; Choe, H. S.; Nam, S.; Hu, Y.; Das, S.; Klemic, J. F.; Ellenbogen, J. C.; Lieber, C. M., *Nature* **2011**, 470, p 240-244.

77. Wu, Y.; Xiang, J.; Yang, C.; Lu, W.; Lieber, C. M., *Nature* **2004**, 430, p 61-65.

78. Zhang, W.; Brongersma; S.H.; Li, Z.; Li, D.; Richard, O.; Maex, K., *J. Appl. Phys.* **2007**, 101, 06370.

79. Durkan, C.; Welland, M. E., *Phys. Rev. B* **2000**, 61, 14215–14218.

80. Chen, X.; Victora, R. H., *Appl. Phys. Lett.* **2008**, 93, 16, p162105.

81. Chawla, J. S.; Gstrein , F., O'Brien, K. P.; Clarke, J. S., and D. Gall, *Phys. Rev. B* **2011**, 84, 235423.

82. Karim, S.; Ensinger, W.; Cornelius, T. W.; Neumann, R., *Physica E: Low-dimensional Systems and Nanostructures* **2008**, 40, 10, 3173–3178.

83. Xiang, C.; Gu□ell, A. G.; Brown, M. A.; Kim, J. Y.; Hemminger, J. C.; Penner, R. M., *Nano Lett.* **2008**, 8, 9, 3017–3022.

84. Xiang, C.; Kung, S.-C.; Taggart, D. K.; Yang, F.; Thompson, M. A.; Gu□ell, A. G.; Yang, Y.; Penner, R. M., *ACS Nano* **2008**, 2, 9, 1939–1949.

85. Li, X.; Wei, Y; Lu, L.; Lu, K., Gao, H., *Nature* **2010**, 464, 7290, 877–880.

86. Lu, L.; Shen, Y.; Chen, X.; Qian, L.; Lu, K., *Science* **2004**, vol. 304, no. 5669, pp. 422 –426.

87. Graham, R. L.; Alers, G. B.; Mountsier, T.; Shamma, N.; Dhuey, S.; Cabrini, S.; Geiss, R. H.; Read, D. T.; Peddeti, S.; *Appl. Phys. Lett.* **2010**, 96, 4, 042116.

88. Kim, T.-H.; Zhang, X.-G.; Nicholson, D. M.; Evans, B. M.; Kulkarni, N. S.; Radhakrishnan, B.; Kenik, E. A.; Li, A.-P. ; *Nano Lett.* **2010**, 10, 8, 3096–3100.

89. Kitaoka, Y.; Tono, T.; Yoshimoto, S.; Hirahara, T.; Hasegawa, S.; Ohba, T., *Appl. Phys. Lett.* **2009**, 95, 5, 052110.

90. Wood, R.; Williams, M.; Kavcic, A.; Miles, J., *IEEE Trans. Magn.* **2009**, vol. 45, p. 917.

91. Fan, D. L.; Cammarata, R. C.; Chien, C. L., *Appl. Phys. Lett.* **2008**, 92, 9, 093115.

92. *The International Technology Roadmap for Semiconductors* **2011**, pages 23, 41.

93. Service, R. F., *Science* **2006**, 314, 1868-1870.

94. Terris, B., *J. Magn. Magn. Mater.* **2009**, 321, 512-517

95. Peng, J., *Langmuir* **2006**, 22, 3955-3958.

96. Wang, J. P., *Proc. IEEE* **2008**, 96, 1847-1863.

97. Chantrell, R.W.; Verdes, C.; Satoh, A.; Harrell, J.W.; Nikles, D., *J. Magn. Magn. Mater*. **2006**, 304, 27-31.

98. Naito, K., *Chaos* **2005**, 15, 47507-1-7.

99. Weiss, N.; Cren, T.; Epple, M.; Rusponi, S.; Baudot, G.; Rohart, S.; Tejeda, A.; Repain, V.; Rousset, S.; Ohresser, P.; Scheurer, F.; Bencok, P.; Brune, H., *Phys. Rev. Lett.* **2005**, 95, 157204-1-4.

100. Jones, B. A.; O'Grady, K., *J. Appl. Phys.* **2005**, 97, 10J312.

101. Puntes, Victor F.; Gorostiza, Pau; Aruguete, Deborah M.; Bastus, Neus G.; Alivisatos, A. Paul., *Nat. Mater.* **2004**, 3, 263-268.

102. Sun, S.; Murray, C.B.; Weller, D.; Folks, L.; Moser, A., *Science* **2000**, 287, 1989-1991.

103. Naito, K.; Hieda, H.; Sakurai, M.; Kamata, Y.; Asakawa, K., *IEEE Trans. Magn.* **2002**, 38, 1949-1951.

104. Kamata, Y.; Kikitsu, A.; Kihara, N.; Marita, S.; Kimura, K.; Isumi, H., *IEEE Trans. Magn.* **2011**, 47, 51-54.

105. Kappenberger, P, Luo, F.; Heyderman, L. J.; Solak, H. H.; Padeste, C.; Brombacher, C.; Makarov, D.; Ashworth, T. V.; Philippe, L.; Hug, H. J.; Albrecht, M., *Appl. Phys. Lett.* **2009**, 95, 023116.

106. Yang, X.; Xu, Y.; Lee, K.; Xiao, S; Kuo, D.; Weller, D., *IEEE Trans. Magn.* **2009**, 45, 833-838.

107. Yang, X.; Wan, L.; Xiao, S.; Xu, Y.; Weller, *ACS Nano* **2009**, 7, 1844-1858.

108. Li, M.; Ober, C. K., *Mater. Today* **2006**, 9, 30-39.

109. Kitano, H.; Akasaka, S.; Inoue, T.; Chen, F.; Takenaka, M.; Hasegawa, H.; Yoshida, H.; Nagano, H., *Langmuir* **2007**, 23, 6404-6410.

110. Stoykovich, M. P.; Nealey, P. F., *Mater. Today* **2006**, 9, 20.

111. Cheng, J. Y.; Mayes, A. M.; Ross, C., *Nat. Mater.* **2004**, 3, 823-828.

112. Kim, S.O.; Solak, H.H.; Stoykovich, M.P.; Ferrier, N.J.; de Pablo, J.J.; Nealey, P.F., *Nature* **2003**, 424, 411-414.

113. Choi, Chulmin; Hong, Daehoon; Oh, Young; Noh, Kunbae; Kim, Jin Yeol; Chen, Leon; Liou, Sy-Hwang; Jin, Sungho., *Mater. Lett.* **2010**, 6, 113-116.

114. Ross, C. A.; Cheng, J. Y., *MRS Bull.* **2008**, 33, 838.

115. Kryder, M.H.; Gage, E.C.; McDaniel, T.W.; Challener, W.A.; Rottmayer, R.E.; Ganping Ju; Yiao-Tee Hsia; Erden, M.F., *Proc. IEEE* **2008**, 961810–1835.

116. Zhu, J.-G; Zhu, X.; Tang, Y., *IEEE Trans. Magn.* **2008**, 44, 125–131.

117. Friedman, R. S.; McAlpine, M. C.; Ricketts, D. S.; Donhee Ham; Lieber, C. M., *Nature* **2005**, 434, 1085-1085.

118. Frank, S.; Poncharal, P.; Wang, Z. L.; de Heer, W. A., *Science* **1998**, 280, 1744-1746.

119. Yang, P; Yan, R.; Fardy, M., *Nano Lett.* **2010**, 10, 1529–1536.

120. Briseno, A. L.; Mannsfeld, S. C. B.; Lu, X.; Xiong, Y.; Jenekhe, S. A.; Bao, Z.; Xia, Y., *Nano Lett.* **2007**, 7, 668–675.

121. Hu, Y.; Xiang, J.; Liang, G.; Yan, H.; Lieber, C. M., *Nano Lett.* **2008**, 8, 925–930.

122. Choi, Y.-S.; Tsunematsu, H.; Yamagata, S.; Okuyama, H.; Nagamine, Y.; Tsunekawa, K., *Jap. J. Appl. Phys.* **2009**, 48, 120214.

123. Childress, J. R.; Carey, M. J.; Maat, S.; Smith, N.; Fontana, R. E.; Druist, D.; Carey, K.; Katine, J. A.; Robertson, N.; Boone, T. D.; Alex, M.; Moore, J.; Tsang, C. H., *IEEE Trans. Magn.* **2008**, 44, 90-94.

124. Nakamoto, K.; Hoshiya, H.; Katada, H.; Hoshino, K.; Yoshida, N.; Shiimoto, M.; Takei, H.; Sato, Y.; Hatatani, M.; Watanabe, K.; Carey, M.; Maat, S.; Childress, J., *IEEE Trans. Magn.* **2008**, 44, 95-99.

125. Wang, L.; Qiu, J. J.; McMahon, W. J.; Li, K. B.; Wu, Y. H., *Phys. Rev. B* **2004**, 69, 214402.

126. Yuasa, H.; Hara, M.; Fukuzawa, H., *Appl. Phys. Lett.* **2008**, 92, 262509.

127. Yang, X.; Xiao, S.; Wu, W.; Xu, Y.; Mountfield, K.; Rottmayer, R.; Lee, K.; Kuo, D., Weller, D., *J. Vac. Sci. Tech. B* **2007**, 25, 2202-2209.

128. Image J is a public domain image processing tool created at the National Institute of Health.

129. Fuchs, K., *Mathematical Proceedings of the Cambridge Philosophical Society* **1938**, 34, 100-108.

130. Sondheimer, E.H., *Advances In Physics (Quarterly Supplement of Philosophical Magazine)* **1952**, 11-42.

131. Mayadas A.F.; Shatzkes M; Janak J.F., *Appl. Phys. Lett.* **1969**, 14, p345-347.

132. Steinhogl, W.; Schindler G.; Steinlesberger, G.; Engelhardt M., *Phys. Rev. B* **2002**, 66, 075414.

133. Smith, N.; Katine, J.A.; Childress, J.R.; Carey, M.J., *IEEE Trans. Magn.* **2006**, 42, 114-119.

134. Piraux, L; George, J. M.; Despres, J. F.; Leroy, C.; Ferain, E; Legras, R.; Ounadjela, K.; Fert, A., *Appl. Phys. Lett.* **1994**, 65, 2484-2486.

135. Blondel, A.; Meier, J. P.; Doudin, B.; Ansermet, J.-Ph., *Appl. Phys. Lett.* **1994**, 65, 3019-3021.

136. Liu, K.; Nagodawithana, K.; Searson, P. C.; Chien, C. L., *Phys. Rev. B* **1995**, 51, 7381-7384.

137. Ohgai, T.; Hoffer, X.; Gravier, L.; Wegrowe, J-E.; Ansermet, J-Ph., *Nanotech.* **2003**, 14, 978.

138. Ramana, B.; Moitreyee, M.; Wu, S; Ananth, N., *Jpn. J. Appl. Phys.* **2004**, 43, 7381-7385.

139. Hernández, S; Tan, L.; Stadler, B.J.H.; Victora, R. H., *J. Appl. Phys.* **2011**, 109, 07C916.

140. Y. Liu, Z. Zhang, P. P. Freitas, and J. L. Martins, *Appl. Phys. Lett.* **2003**, 82, 2871.

141. Yiming Huai, Frank Albert, Paul Nguyen, Mahendra Pakala, and Thierry Valet, *Appl. Phys. Lett.* **2004**, 84, 3118.

142. G. D. Fuchs, N. C. Emley, I. N. Krivorotov, P. M. Braganca, E. M. Ryan, S. I. Kiselev, J. C. Sankey, D. C. Ralph, R. A. Buhrman, and J. A. Katine, *Appl. Phys. Lett.* **2004**, 85, 1205.

143. J. A. Katine, F. J. Albert, R. A. Buhrman, E. B. Myers, and D. C. Ralph, *Phys. Rev. Lett.* **2000**, 84, 3149.

144. F. J. Albert, N. C. Emley, E. B. Myers, D. C. Ralph, and R. A. Buhrman, *Phys. Rev. Lett.* **2002**, 89, 226802.

145. Mangin et *al.*, *Nature Mat.* **2006** 5, 210.

146. Valet, T; Fert, A., *Phys. Rev. B* **1993**, 48, 10.

147. K. S. M. Reddy, J. J. Park, M. M. Maqableh, A. Flatau, and B. J. H. Stadler, *J. Appl. Phys*. **2012**, 111, 07A920.

148. Krimpalis et *al.*, *Journal of Advanced Research in Physics* **2010**, 1(2), 021005.

149. Hao Meng and Jian-Ping Wang, *Appl. Phys. Lett.* **2006**, 88, 172506.

150. Luqiao Liu, Takahiro Moriyama, D. C. Ralph, and R. A. Buhrman, *Appl. Phys. Lett.* **2009**, 94, 122508.